



CZECH TECHNICAL UNIVERSITY IN PRAGUE

**Faculty of Civil Engineering
Department of Mechanics**

Constitutive Model of Timber

Master Thesis

Study Programme: Civil Engineering
Branch of study: Building Structures

Thesis advisor: prof.Ing. Petr Kabele, Ph.D.

Eliška Bartůňková

Prague 2012/2013



ČESKÉ VYSOKÉ UČENÍ TECHNICKÉ V PRAZE

**Fakulta stavební
Katedra mechaniky**

Konstitutivní model dřeva

Constitutive Model of Timber

Diplomová práce

Studijní program: Stavení inženýrství (SI)
Studijní obor: Konstrukce pozemních staveb (C)

Vedoucí práce: prof. Ing. Petr Kabele, Ph.D.

Eliška Bartůňková

Praha 2012/2013



ZADÁNÍ DIPLOMOVÉ PRÁCE

studijní program: STAVEBNÍ INŽENÝRSTVÍ (SI)
studijní obor: KONSTRUKCE POZEMNÍCH STAVEB (C)
akademický rok: 2012/2013

Jméno a příjmení diplomanta: Eliška Bartůňková
Zadávací katedra: K132 Katedra mechaniky
Vedoucí diplomové práce: prof. Ing. Petr Kabele, Ph.D.
Název diplomové práce: Konstitutivní modelování dřeva
Název diplomové práce v anglickém jazyce: Constitutive modelling of timber


Rámcový obsah diplomové práce: Vymezení problematiky dřeva. Přehled typů modelu dřeva.
Tvorba konstitutivního modelu dřeva: teorie, aplikace v programu MATLAB. Porovnání výsledků výpočtu s experimentálními daty.

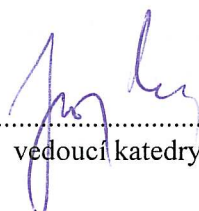
Datum zadání diplomové práce: 13.9.2012 Termín odevzdání: 21.12.2012
(vyplňte poslední den výuky přísl. semestru)

Diplomovou práci lze zapsat, kromě oboru A, v letním i zimním semestru.


Pokud student neodevzdal diplomovou práci v určeném termínu, tuto skutečnost předem písemně zdůvodnil a omluva byla děkanem uznána, stanoví děkan studentovi náhradní termín odevzdání diplomové práce. Pokud se však student řádně neomluvil nebo omluva nebyla děkanem uznána, může si student zapsat diplomovou práci podruhé. Studentovi, který při opakovaném zápisu diplomovou práci neodevzdal v určeném termínu a tuto skutečnost řádně neomluvil nebo omluva nebyla děkanem uznána, se ukončuje studium podle § 56 zákona o VŠ č. 111/1998 (SZŘ ČVUT čl 21, odst. 4).

Diplomant bere na vědomí, že je povinen vypracovat diplomovou práci samostatně, bez cizí pomoci, s výjimkou poskytnutých konzultací. Seznam použité literatury, jiných pramenů a jmen konzultantů je třeba uvést v diplomové práci.


vedoucí diplomové práce


vedoucí katedry

Zadání diplomové práce převzal dne: 20.9.2012


diplomant

Formulář nutno vyhotovit ve 3 výtiscích – 1x katedra, 1x diplomant, 1x studijní odd. (zašle katedra)

Nejpozději do konce 2. týdne výuky v semestru odešle katedra 1 kopii zadání DP na studijní oddělení a provede zápis údajů týkajících se DP do databáze KOS.

DP zadává katedra nejpozději 1. týden semestru, v němž má student DP zapsanou.
(Směrnice děkana pro realizaci stud. programů a SZZ na FSv ČVUT čl. 5, odst. 7)

SPECIFIKACE ZADÁNÍ

Jméno diplomanta: Eliška Bartůňková

Název diplomové práce: Konstitutivní modelování dřeva

Základní část: Konstitutivní modelování dřeva podíl: 100 %

Formulace úkolů: Vymezení problematiky dřeva.

Přehled typů modelu dřeva.

Tvorba konstitutivního modelu dřeva: teorie, aplikace v programu MATLAB.

Porovnání výsledků výpočtu s experimentálními daty.

Podpis vedoucího DP: 

Datum: 20.9.2012

Případné další části diplomové práce (části a jejich podíl určí vedoucí DP):

2. Část: _____ podíl: _____ %

Konzultant (jméno, katedra): _____

Formulace úkolů: _____

Podpis konzultanta: _____ Datum: _____

3. Část: _____ podíl: _____ %

Konzultant (jméno, katedra): _____

Formulace úkolů: _____

Podpis konzultanta: _____ Datum: _____

4. Část: _____ podíl: _____ %

Konzultant (jméno, katedra): _____

Formulace úkolů: _____

Podpis konzultanta: _____ Datum: _____

Poznámka: Zadání včetně vyplněných specifikací je nedílnou součástí diplomové práce a musí být přiloženo k odevzdané práci (vyplněné specifikace není nutné odevzdat na studijní oddělení spolu s 1.stranou zadání již ve 2.týdnu semestru)

DECLARATION

Name: Eliška Bartůňková
Email: bartunkova.eliska@gmail.com

Title of the dissertation: Constitutive Model of Timber
Supervisor: prof. Ing. Petr Kabele, Ph.D.
Year: 2012/2013

I hereby declare that all information in this document has been obtained and presented in accordance with academic rules and ethical conduct. I also declare that, as required by these rules and conduct, I have fully cited and referenced all material and results that are not original to this work.

University: Czech Technical University in Prague
Date: 21.12.2012
Signature: _____

ACKNOWLEDGEMENTS

I would like to thank my supervisor prof.Ing. Petr Kabele, Ph.D. for proposing the topic of this thesis, for ideas he came up with and for his willingness to help with any problem that arose. Also, I would like to thank Ing. Hana Hasníková for her useful help and sharing her experience regarding the availability of experimental data of timber.

Last but not least, I would like to thank my family and friends for their devoted social and financial support.

ABSTRACT

Timber is one of the most frequently used building materials both in ancient and modern engineering constructions. Recently, the use of timber structures has increased in the construction industry due to the advantages of environmentally friendly nature of timber and low handling costs. Nevertheless, the complexity of timber structure causes difficulties in adequate description of timber behaviour by means of mathematical models.

This thesis provides a summary of typical wood behavior and wood characteristics and an overview of current timber models together with a brief discussion on their applicability to a model developed in this work. The core of the thesis is a two-dimensional homogeneous constitutive model of timber fracturing under tensile and shear loads that was implemented in a MATLAB[®] computer code and verified. The model performance was demonstrated for various load cases with isotropic and orthotropic material properties and also for an unloading/reloading cycle.

In the proposed constitutive model, we idealize timber as a quasi-brittle material. Thus, we consider the material as a continuum with discontinuities (cracks). The continuous part is characterized by elastic orthotropic stress-strain law while traction-separation law describes the behavior of the discontinuities (cracks). Fixed smeared crack model is used to represent the fracture. Prior to cracking, wood obeys the rules of orthotropic elasticity. The proposed model considers only one initiated crack in material at the same time and small deformations (lower than 0.05ε).

A crack is initiated if failure criterion is fulfilled. Whether a crack forms across (crack type 1) or along the grain (crack type CT2) is decided based on threshold angle between the grain direction and the principal stress direction. This angle is considered as a material parameter. Crack across the grain is perpendicular to the principal stress direction while the crack along the grain keeps parallel to the fibers irrespective of the principal stress direction. Consequently, at the crack initiation state, the crack type CT1 is exposed only to normal traction while the crack type CT2 can be exposed both to normal and tangential traction. After crack initiation, as the fixed crack model is used, the direction of the crack (CT1 or CT2) is freezed and since the principal stress axes can rotate, both normal and shear tractions may subsequently arise on the crack.

Traction-separation law defining the behavior of the initiated crack is softening in normal direction to the crack ($t_n(\varepsilon_{nn}^c)$). In tangential direction, traction-separation law $t_m(\varepsilon_{nm}^c, \gamma_{nm}^c)$ is proposed using an arctangential function that fulfills the following assumptions: (i) the maximal value of shear traction t_m never exceeds shear strength f_s ($t_m < f_s$), (ii) the function of $t_m(\varepsilon_{nm}^c, \gamma_{nm}^c)$ can take the value of $t_m \in [0, f_s)$ at the crack initiation state. Thus, traction separation law in both local directions (n, m) ensures a smooth transition from the stress state on the failure surface to the proposed cracking cohesive relationship. Traction-separation law is limited in both local directions by critical crack opening (δ_{crit}).

On account of the developed model performance demonstrated for various load cases, the model is consistent with expected timber behavior.

Keywords: timber, 2D constitutive model, orthotropic elasticity, orthotropic fracture criterion, fixed smeared crack model, traction-separation law, shear retention function, unloading/reloading

ABSTRAKT

Dřevo je jeden z nejpoužívanějších konstrukčních materiálů historických i moderních budov. V posledních letech je dřevo více a více používáno ve stavebnictví díky jeho výhodným vlastnostem, které nezatěžují životní prostředí, a nízkým nákladům. Nicméně složitá struktura dřeva komplikuje popis jeho chování pomocí matematických modelů.

Tato diplomová práce shrnuje typické chování dřeva a jeho charakteristiky. Dále poskytuje přehled současných modelů dřeva spolu s krátkým zhodnocením jejich použitelnosti pro model vyvinutý v této práci. Jádrem diplomové práce představuje dvourozměrný homogenní konstitutivní model porušení dřeva trhlinami pro zatížení tahem a smykem, který byl implementován v počítačovém kódu MATLAB[®] a verifikován. Chování modelu bylo demonstrováno na několika zatěžovacích stavech za použití izotropních a ortotropních materiálových vlastností, a také na odtěžovacím cyklu.

V navrženém konstitutivním modelu dřevo idealizujeme jako kvazi křehký materiál, který považujeme za kontinuum obsahující diskontinuity (trhliny). Spojitá část materiálu (kontinuum) je charakterizována elastickým ortotropním vztahem mezi napětím a deformací, zatímco zákon koheze popisuje chování diskontinuit (trhlin). Model fixované rozetřené trhliny je použit pro popis trhliny. Předpokládáme, že před vznikem trhliny se dřevo chová ortotropně elasticky. Navržený model uvažuje existenci maximálně jedné trhliny a malé deformace (menší než 0.05ε).

Trhlina se vytvoří, pokud je splněna podmínka porušení. Zda se vytvoří trhlina přes vlákna (typ trhliny CT1) či podél vláken (typ trhliny CT2) závisí na mezním úhlu mezi podélnou orientací vláken a směrem hlavního napětí. Tento úhel má roli materiálového parametru. Trhlina přes vlákna (CT1) je vždy kolmá na směr hlavního napětí, zatímco v případě trhliny podél vláken (CT2) je její směr vždy s vlákny bez ohledu na směr hlavního napětí. Z toho plyne, že při vzniku trhliny je trhlina CT1 zatížena pouze normálovou složkou vektoru napětí, zatímco trhlina CT2 může být namáhána jak normálovou tak tečnou složkou vektoru napětí. Po vytvoření trhliny je směr trhliny (CT1 nebo CT2) zafixován, což je hlavní předpoklad použitého modelu fixované trhliny, a jelikož osy hlavního napětí mohou rotovat, trhlina může být vystavena normálové i tangenciální složce vektoru napětí.

Zákon koheze definující chování vzniklé trhliny je změkčujícího charakteru pro normálový směr vzhledem k trhlině ($t_n(\varepsilon_{nn}^c)$). Pro tečný směr je trakční separační zákon $t_m(\varepsilon_{nn}^c, \gamma_{nm}^c)$ nově navržen pomocí arcustangenciální funkce, která splňuje následující předpoklady: (i) maximální hodnota t_m nikdy nepřesáhne smykovou pevnost f_s ($t_m < f_s$), (ii) funkce $t_m(\varepsilon_{nn}^c, \gamma_{nm}^c)$ může nabývat hodnot $t_m \in [0, f_s)$ v okamžiku vzniku trhliny. Tímto zákonem koheze zajišťuje hladký přechod v obou lokálních směrech mezi stavem napětí na ploše porušení a navrženým kohezním vztahem pro trhlinu. Zákon koheze je omezen hodnotou kritického otevření trhliny (δ_{crit}) v obou lokálních směrech.

Vzhledem k chování modelu, které bylo demonstrováno na několika zatěžovacích případech, je navržený model konzistentní s očekávaným chováním dřeva.

Klíčová slova: dřevo, 2D konstitutivní model, ortotropní elasticita, ortotropní kritérium porušení, model fiktivní rozetřené trhliny, zákon koheze, funkce retence smykové tuhosti, odtěžování/přítěžování

TABLE OF CONTENTS

1.	Introduction	1
1.1	Motivation.....	1
1.2	Objectives	1
1.3	Organization of the thesis	1
2.	Wood properties	2
2.1	Macroscopic description of a tree trunk section	2
2.2	Microscopic structure of wood	3
2.2.1	Wood cells	3
2.2.2	Softwood and hardwood	4
2.2.2.1	Softwood	5
2.2.2.2	Hardwood.....	6
2.3	Density and specific gravity	7
2.3.1	Density	7
2.3.2	Density within growth rings	8
2.3.3	Specific gravity.....	8
2.4	Moisture in wood.....	8
2.4.1	Moisture content (MC)	8
2.4.2	Fiber saturation point (MC_{fs}).....	9
2.4.3	Maximum moisture content (MC_{max}).....	9
2.4.4	Equilibrium moisture content (EMC).....	9
2.4.5	Sorption hysteresis	10
2.4.6	Dimensional instability	10
2.5	Mechanical properties of wood	12
2.5.1	Elastic orthotropic properties	12
2.5.2	Non-elastic properties	13
2.5.2.1	Failure types	13
2.5.2.2	Stress-strain curves	15
2.5.2.3	Fracture.....	16
2.5.3	Fracture toughness and fracture energy	18
2.5.3.1	Critical strain energy release rate G_c (energy-balance approach).....	19
2.5.3.2	Critical stress intensity factor (SIF) K_c (stress intensity approach).....	19
2.5.3.3	Fracture energy G_f	20
2.5.3.4	Test methods for fracture toughness and fracture energy determination.....	21
2.5.4	Strength properties	21
2.6	Natural defects affecting mechanical properties of wood	22
2.6.1	Reaction wood	22
2.6.2	Cross grain.....	23
2.6.3	Knots	23
2.6.4	Pitch Pockets	24
2.6.5	Cracks.....	24
3.	Overview of current models of timber	25
3.1	Micro-macro modeling of wood properties	25
3.1.1	Micro-mechanical approach.....	26
3.1.2	Continuum modeling approach.....	28
3.2	Moisture induced eigen-stresses	29
3.2.1	Parameter influence on moisture induced eigen-stresses.....	30
3.2.2	Moisture-induced stresses under different climates	31
3.2.3	A 3D moisture-stress FEM analysis.....	31
3.2.4	2D orthotropic model of wood-drying.....	32
3.3	FEM at large deformations and brittle failure prediction	32
3.4	Fracture in spruce: damage and linear mechanics.....	33
3.5	Summary.....	34
4.	Constitutive model for timber under tension and shear.....	36
4.1	Assumptions	37
4.2	Elastic orthotropic 2D model.....	37

4.3	Failure criterion	37
4.4	Crack types	39
4.5	Smearred crack model (SCM)	42
4.5.1	One-dimensional smearred crack model	42
4.5.2	Two-dimensional fixed smearred crack model	43
4.5.3	Application of two-dimensional fixed smearred crack model	44
4.6	Cohesive law in n direction	45
4.7	Cohesive law in m direction	47
4.7.1	Linear-based function t_m	47
4.7.2	Arctangential function of t_m	48
4.8	Critical crack opening δ_{crit}	50
4.9	Crack unloading/reloading cycle	50
4.10	Characteristic length l_{ch}	51
4.11	Transformation between coordinate systems	52
4.12	Computational Newton-Raphson method	53
4.13	Code scheme	55
4.14	Input data	56
5.	Results	57
5.1	Model performance with isotropic material properties	57
5.1.1	LC V1: $\Delta\varepsilon_x$ and then $\Delta\gamma_{xy}$, CT1, $\theta = 0^\circ$	57
5.1.2	LC V2: $\Delta\varepsilon_y$ and then $\Delta\gamma_{xy}$, CT2, $\theta = 90^\circ$	59
5.1.3	LC V3: $\Delta\varepsilon_x$ and then $\Delta\gamma_{xy}$, CT1, $\theta = 20^\circ$	62
5.1.4	LC V4: $\Delta\varepsilon_x$ and then $\Delta\gamma_{xy}$, CT1, $\theta = 20^\circ$, minor orthotropy	63
5.2	Model performance with orthotropic material properties	64
5.2.1	LC CT1-1: $\Delta\varepsilon_x$, $\theta = 0^\circ$ (pure tension parallel to grain)	64
5.2.2	LC CT1-2: $\Delta\varepsilon_x$ and then $\Delta\gamma_{xy}$, $\theta = 0^\circ$	67
5.2.3	LC CT1-3: $\Delta\varepsilon_x \wedge \Delta\gamma_{xy}$, $\theta = 4.5^\circ$	70
5.2.4	LC CT1-4: $\Delta\varepsilon_x$ or $\pm\Delta\gamma_{xy}$, $\theta = 0^\circ$	72
5.2.5	LC CT2-1: $\Delta\varepsilon_y$, $\theta = 90^\circ$ (pure tension perpendicular to the grain)	75
5.2.6	LC CT2-2: $\Delta\varepsilon_y \wedge \Delta\gamma_{xy}$, $\theta = 90^\circ$	77
5.2.7	LC CT2-3: $\Delta\varepsilon_y$ or $\pm\Delta\gamma_{xy}$, $\theta = 90^\circ$	79
5.2.8	LC CT2-4: $\Delta\gamma_{xy}$, $\theta = 90^\circ$ (pure shear)	82
5.3	Model performance during unloading/reloading cycle	84
6.	Conclusion	87
	REFERENCES	89
	APPENDIX 1: Tension test parallel to grain of chestnut timber	92
	APPENDIX 2: Code of constitutive model developed in MATLAB[®] software	97

1. Introduction

1.1 Motivation

Timber is one of the most frequently used building materials in both ancient and modern engineering constructions. Recently, the use of timber structures has increased in the construction industry due to the advantages such as environmentally friendly nature of timber and low handling costs.

Nevertheless, there is still a gap between understanding of timber behavior from micro to macro level and adequate timber models. Timber behavior at micro level ought to be integrated with the knowledge of its behavior on different scales, especially those that have a dominant effect on its structural performance.

1.2 Objectives

This thesis has the following objectives:

- to summarize typical wood behavior and characteristics describing it,
- to make an overview of current models of timber,
- to develop a general constitutive model of timber fracturing under tensile and shear loads and implement it in MATLAB[®] software, to verify the model and to demonstrate and discuss the performance of the model by analyzing the response of spruce under complex loading paths.

1.3 Organization of the thesis

The thesis is organized in 6 chapters as follows:

- Chapter 1: Introduction,
- Chapter 2: Wood properties,
- Chapter 3: Overview of current models of timber,
- Chapter 4: Constitutive model for timber under tension and shear,
- Chapter 5: Verification and results,
- Chapter 6: Conclusion.

In chapter 1, the main challenges regarding the modeling of timber are briefly described. Then, the objectives and organization of the thesis are outlined. Chapter 2 gives an overview of the typical structural, physical, and mechanical wood properties. Chapter 3 provides an overview of up to date models of timber. Chapter 4 represents the core of the thesis. It describes the theory behind the proposed constitutive model of timber, its application and input data. Chapter 5 concerns verification of the constitutive model developed in MATLAB[®] software and discussion of obtained results for different load cases. Chapter 6 summarizes the important ideas and results of this thesis together with suggestions for future work.

2. Wood properties

Wood is a complex biological structure composed of many chemistries and cell types that all together ensure conduction of water from the roots to leaves, mechanical support of the plant body and storage of biochemicals. Wood properties can be of physical, mechanical, chemical, biological or technological essence. This chapter describes basic principles of timber behavior. The following subchapters discuss macroscopic and microscopic structure of wood, density and specific gravity, influence of moisture, mechanical properties and natural defects affecting mechanical properties of wood.

2.1 Macroscopic description of a tree trunk section

Main features of timber (milled from a tree trunk) can be observed in **Figure 1**. Main parts of a trunk from the outside of the tree to the inside are outer bark, inner bark, vascular cambium, sapwood, heartwood, juvenile wood and the pith. These parts are briefly described in the following paragraphs:

- The outer layer of a trunk is a bark, which protects the tree from fire, injury or temperature. The inner layers of the bark transport nutrients from leaves to growth parts. (Kuklík, 2008)
- Wood cells grow in a cambium. New wood cells grow towards the interior and new bark cells grow towards the exterior of the cambium. (Kuklík, 2008)
- New cells of upward flow of sap (water and nutrients) from the roots to the crown are known as sapwood. (Kuklík, 2008)
- Heartwood cells in the inner part of the stem do not grow anymore and have the role of receptacles of waste products (extractives). Heartwood is darker in color than sapwood due to the incrustation with organic extractives. Thank to these chemicals, heartwood is more resistant to decay and wood boring insects. Heartwood formation results in reduction in moisture content. (Kuklík, 2008)
- Juvenile wood is the wood of the first 5 – 20 growth rings and thus it is a very early wood. It has different physical and anatomical properties than that of mature wood. The differences consist in fibril angle, cell length, specific gravity, percentage of latewood, cell wall thickness and lumen diameter. It tends to be inferior in density and cell structure and exhibits much greater longitudinal shrinkage than mature wood. (Kuklík, 2008)
- Finally, the very center of the trunk is a pith. This part is typically of a dark color and represents the original twig of a young tree. (Kuklík, 2008)

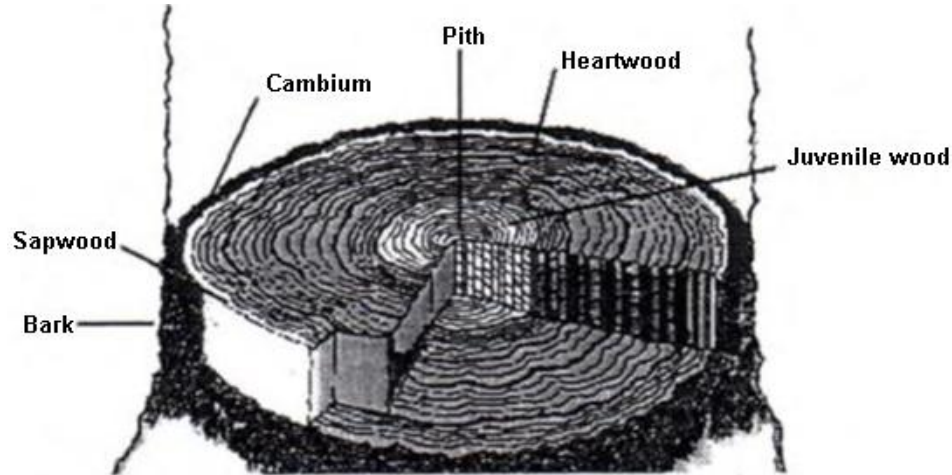


Figure 1 - Cross section of a tree trunk (Kuklík, 2008)

Collections of timber cells produced together over a discrete time interval are known as growth increments (growth rings). Cells formed at the beginning of the growth increment are called earlywood cells. Cells formed in the latter portion of the growth increment are called latewood cells. (Wiedenhoef, 2010)

2.2 Microscopic structure of wood

The fundamental differences between woods are founded on the types, sizes, proportions, pits, and arrangements of different wood cells. These fine structural details can affect the use of a wood. This subchapter describes wood cells structure and function with regard to its differences between hardwood and softwood.

2.2.1 Wood cells

Wood is composed of discrete cells connected and interconnected in an intricate and predictable fashion to form an integrated continuous system from root to twig. The cells of wood are usually many times longer than wide and are oriented in two separate systems: the axial system (long axes running up and down the trunk) and the radial system (elongated perpendicularly to the long axis of the organ and are oriented from the pith to the bark). The axial system provides the long-distance water movement and the bulk of the mechanical strength of the tree. The radial system provides lateral transport for biochemicals and an important fraction of the storage function. (Wiedenhoef, 2010)

In most cells in wood there are two domains; the cell wall and the lumen. The lumen is a critical component of many cells in the context of the amount of space available for water conduction or in the context of a ratio between the width of the lumen and the thickness of the cell wall. The lumen has no structure as it is the void space in the interior of the cell. (Wiedenhoef, 2010)

Cell walls in wood give wood the majority of its properties. The cell wall itself is a highly regular structure. The cell wall consists of three main regions: the middle lamella, the primary wall, and the secondary wall (**Figure 2**). In each region, the cell wall has three major components: cellulose microfibrils, hemicelluloses, and a matrix or encrusting material. Generally, cellulose is a long string-like molecule with high tensile strength, microfibrils are collections of cellulose molecules into even longer, stronger thread-like macromolecules. Lignin is a brittle matrix material. The hemicelluloses help link the lignin and cellulose into a unified whole in each layer of the cell wall. (Wiedenhoef, 2010)

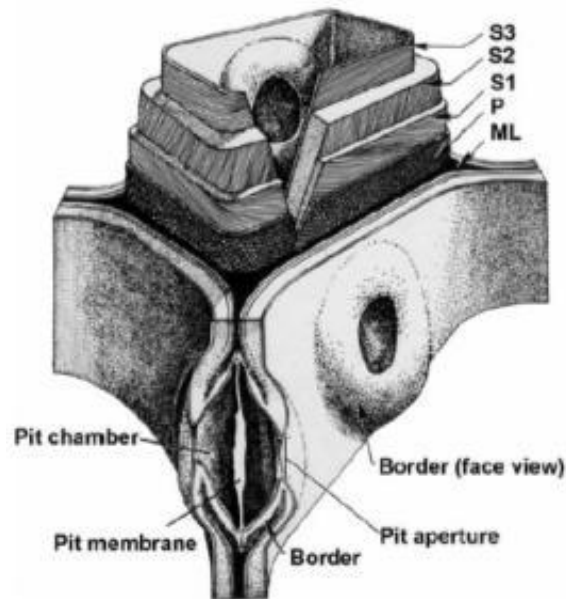


Figure 2 - Cut-away drawing of the cell wall: middle lamella (ML), primary wall with random orientation of the cellulose microfibrils (P), the secondary wall composed of its three layers with illustration of their relative thickness and the microfibril angle: (S1), (S2), and (S3); The lower portion of the illustration shows bordered pits in both sectional and face view (Wiedenhoeft, 2010)

The primary wall (**Figure 2**) is characterized by a largely random orientation of cellulose microfibrils where the microfibril angle ranges from 0° to 90° relative to the long axis of the cell. The secondary cell wall is composed of three layers. The secondary cell wall layer S1 is a thin layer and is characterized by a large microfibril angle. The angle between the mean microfibril direction and the long axis of the cell is large (50° to 70°). The next wall layer S2 the most important cell wall layer in determining the wood properties at a macroscopic level. This is the thickest secondary cell wall layer characterized by a lower lignin percentage and a low microfibril angle (5° to 30°). The S3 layer is relatively thin. The microfibril angle of this layer is $>70^\circ$. This layer has the lowest percentage of lignin of any of the secondary wall layers. (Wiedenhoeft, 2010)

Communication and transport between the wood cells is provided by pits. Pits are thin areas in the cell walls (cell wall modification) between two cells having three domains: the pit membrane, the pit aperture and the pit chamber (**Figure 2**). (Wiedenhoeft, 2010)

2.2.2 Softwood and hardwood

Commercial timber is obtained from two categories of plants, hardwoods and softwoods. To define them botanically, softwoods come from gymnosperms (mostly conifers) and hardwoods come from angiosperms (flowering plants). Softwoods are generally needle-leaved evergreen trees such as pine and spruce, whereas hardwoods are typically broadleaf deciduous trees such as maple, birch and oak. (Wiedenhoeft, 2010)

Main distinction between these two groups consists in their component cells (**Figure 3**). Softwoods have a simpler basic structure that comprises only of two cell types with relatively little variation in structure within these cell types. Hardwoods have greater structural complexity consisting in a greater number of basic cell types and a far greater variability within the cell types. Hardwoods have characteristic type of cell called a vessel element (pore) whereas softwoods lack these. (Wiedenhoeft, 2010)

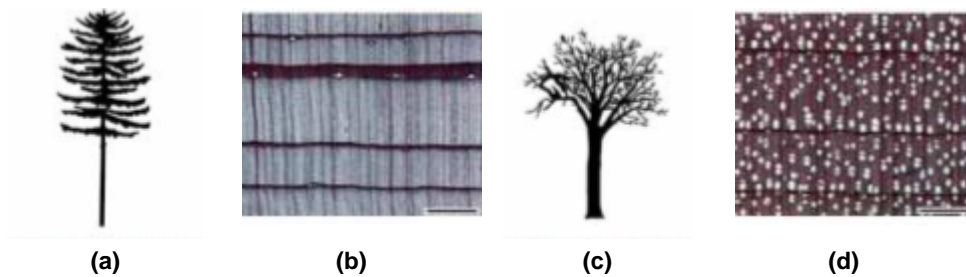


Figure 3 – The general form of a generic softwood tree (a), transverse section of a typical softwood with resin canals as round white spaces (b), the general form of a generic hardwood tree (c), transverse section of a typical hardwood with many vessels and pores as round white structures (d) (Wiedenhoef, 2010)

2.2.2.1 Softwood

Softwood structure is relatively simple (**Figure 4**). The axial (vertical) system is composed mostly of axial tracheids. The radial (horizontal) system is the rays, which are composed mostly of ray parenchyma cells. Another cell types that can be present in softwood are axial parenchyma and resin canal complex. (Wiedenhoef, 2010)

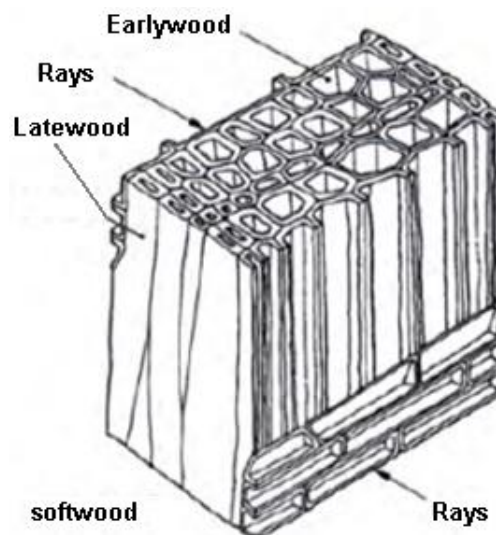


Figure 4 – Structure of softwood, magnified 250 times (Kuklík, 2008)

Tracheids are long cells being the major component of softwoods, making up over 90% of the volume of the wood. They serve both the conductive and mechanical needs. Within a growth ring, they are thin-walled in the earlywood and thicker-walled in the latewood. Water flows between tracheids by passing through circular bordered pits that are concentrated in the ends of the cells. Pit membrane ensures resistance to flow. Tracheids are less efficient conduits compared with the conducting cells of hardwoods due to the resistance of the pit membrane and the narrow diameter of the lumina. (Wiedenhoef, 2010)

In evolving tracheids from earlywood to latewood, the cell wall becomes thicker, while the cell diameter becomes smaller. The difference in growth may result in a ratio latewood density to early wood density of 3:1. (Kuklík, 2008)

Another cell type that is sometimes present in softwoods is axial parenchyma. Axial parenchyma cells are vertically oriented and similar in size and shape to ray parenchyma cells. Resin canal complex is present radially or axially in species of pine, spruce, Douglas-fir, and larch. These structures are voids in the wood. Specialized parenchyma cells producing resin surround resin canals. (Wiedenhoef, 2010)

Rays are formed by ray parenchyma cells (brick-shaped cells). They function primarily in synthesis, storage, and lateral transport of biochemicals and water. (Wiedenhoef, 2010)

The cell arrangement in radial and tangential direction is different. Cells in radial direction are assembled in straight rows while in tangential direction they are disordered (**Figure 5**). This causes that tangential stiffness is lower than the radial one. Also, ray cells aligned in the radial direction reinforce the structure radially and increase the radial stiffness. (Wiedenhoef, 2010)

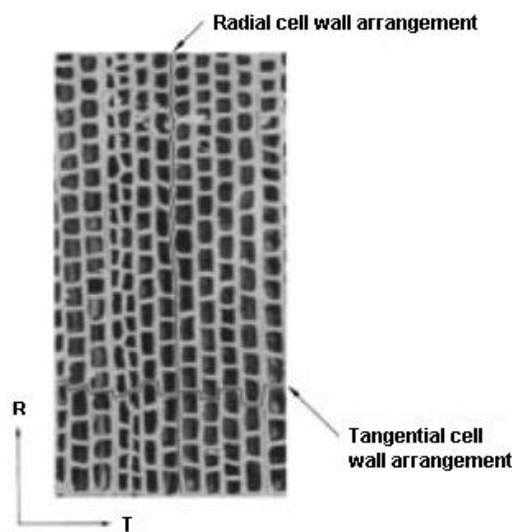


Figure 5 - Cell structure arrangement in the radial and tangential directions (Wiedenhoef, 2010)

2.2.2.2 Hardwood

The structure of a typical hardwood (**Figure 6**) is more complicated than that of softwood. The axial system is composed of various fibrous elements, vessel elements, and axial parenchyma. As in softwoods, rays (composed of ray parenchyma) comprise the radial system, but hardwoods show greater variety in cell sizes and shapes. (Kuklík, 2008)

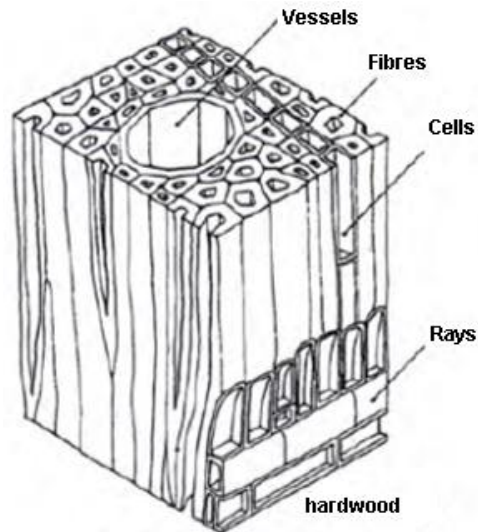


Figure 6 – Structure of hardwood, magnified 250 times (Kuklík, 2008)

Vessel elements (forming vessels) are the specialized water-conducting cells of hardwoods. Vessels are much shorter than tracheids and can be arranged in various patterns. If all the vessels are the same size and more or less scattered throughout the growth ring, the wood is diffuse-porous. If the earlywood vessels are much larger than the latewood vessels, the wood is ring-porous. (Wiedenhoef, 2010)

Hardwoods have perforated tracheary elements (vessels elements) for water conduction, whereas softwoods have imperforate tracheary elements (tracheids). Hardwood fibers have thicker cell walls and smaller lumina than softwood tracheids. Differences in wall thickness and lumen diameters between earlywood and latewood are not as distinct as in softwoods. (Kuklík, 2008)

2.3 Density and specific gravity

This subchapter recalls the definition of density and specific gravity and shows the change in density across a growth ring.

2.3.1 Density

Density is one of the most important physical characteristics of wood. Majority of timber mechanical properties are correlated to it.

Since moisture adds to the mass and causes the volume to swell, density is dependent on moisture. Density ρ_w [kg/m³] is expressed as mass of wood divided by the volume of the specimen at a given moisture content w [%]:

$$\rho_w = \frac{m_w}{V_w} = \frac{m_0(1 + 0.01w)}{V_0(1 + 0.01\beta_V w)} = \rho_0 \frac{1 + 0.01w}{1 + 0.01\beta_V w} \quad [1]$$

where m_0 and V_0 are the mass and volume at zero moisture content (MC). ρ_0 is oven-dry density (at zero MC). β_V is the coefficient of volumetric swelling expressed by units of percentage swelling per percentage increase of MC. In wood science, oven-dry density ρ_0 and density at 12% MC ρ_{12} are most frequently used. (Kuklík, 2008)

In all woods, density is related to wood structure, such as the proportion of the volume of cell wall material to the volume of lumina of those cells, proportion of earlywood and latewood, amount of void space occupied by vessels, etc. (Wiedenhoef, 2010)

2.3.2 Density within growth rings

As each growth ring is composed of three main regions (earlywood, transitionwood and latewood), density changes across it together with its mechanical properties. Density variation for a growth ring of spruce is shown in Figure 7. Function of density variation is linear for earlywood and latewood zone and parabolic for the transitionwood zone. (Persson, 1997)

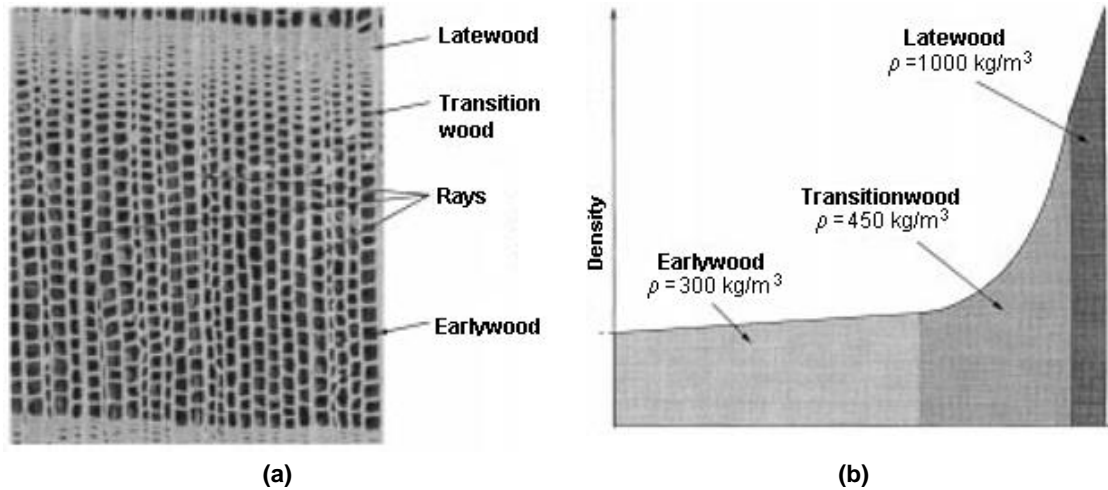


Figure 7 – A growth ring of spruce: cell structure (a), density distribution (b) (Persson, 1997)

2.3.3 Specific gravity

Specific gravity G is defined as the ratio of the density of a substance to the density of water ρ_{water} at a specified reference temperature (typically 4 °C). ρ_{water} is 1 g/cm³ (or 1000 kg/m³). Therefore, a material with a density of 5 g/cm³ has a specific gravity of 5. (Glass and Zelinka, 2010)

2.4 Moisture in wood

Wood is a hygroscopic material, which means that it takes on moisture from the surrounding environment. Moisture exchange between wood and air depends on the relative humidity, temperature of the air and the current amount of water in the wood. This subchapter discusses the macroscopic physical properties of wood related to moisture content (MC) such as fiber saturation point, maximum moisture content, equilibrium moisture content, sorption hysteresis, and dimensional instability.

2.4.1 Moisture content (MC)

Many physical and mechanical properties of wood depend upon the MC of wood. MC is usually expressed as a percentage and can be calculated from

$$MC = \frac{m_{\text{water}}}{m_{\text{wood}}} (100\%) \quad [2]$$

where m_{water} is the mass of water in wood and m_{wood} is the mass of the oven-dry wood. Green wood is usually defined as freshly sawn wood where the cell walls are completely saturated with water and additional water resides in the lumina. The moisture content of green wood can range from about 30% to more than 200%. In green softwoods, the moisture content of sapwood is usually greater than that of heartwood. For example for the black spruce the average MC of sapwood is 113% and the average MC of heartwood is 52%. (Glass and Zelinka, 2010)

2.4.2 Fiber saturation point (MC_{fs})

Moisture can exist in wood as free or bound water. Free water is the form of liquid or vapor in cell lumina and cavities while bound water is held by intermolecular attraction within cell walls. The state when the cell walls are completely saturated (bound water) but no water exists in cell lumina is known as fiber saturation point (MC_{fs}). The fiber saturation point averages about 30% moisture content depending on individual species and individual pieces of wood. (Glass and Zelinka, 2010)

2.4.3 Maximum moisture content (MC_{max})

The maximum moisture content is a state in wood at which both cell lumina and cell walls are completely saturated with water. The major determinant of MC_{max} is basic specific gravity G_b which is based on oven-dry mass and green volume. As G_b increases, the volume of the lumina decreases (together with room available for free water) because the specific gravity of wood cell walls is constant among species. MC_{max} for any basic specific gravity can be estimated according to Glass and Zelinka (2010) from

$$MC_{max} = 100(1.54 - G_b)/1.54G_b \quad [3]$$

where the specific gravity of wood cell walls is taken as 1.54. Maximum possible moisture content ranges from 267% (for $G_b = 0.30$) to 44% (for $G_b = 0.90$) and it is seldom attained in living trees. (Glass and Zelinka, 2010)

2.4.4 Equilibrium moisture content (EMC)

Equilibrium moisture content is MC at which the wood is neither gaining nor losing moisture. EMC depends on both relative humidity and temperature. The relationship among them is shown in **Figure 8**. (Glass and Zelinka, 2010)

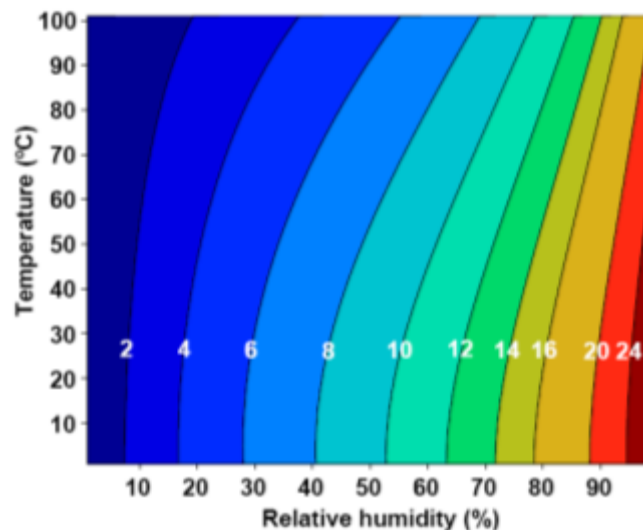


Figure 8 – Equilibrium moisture content of wood (labelled contours) as a function of relative humidity and temperature (Glass and Zelinka, 2010)

For most practical purposes, EMC applicable to wood of any species can be calculated according to Glass and Zelinka (2010) from the following equation:

$$EMC(\%) = \frac{1800}{W} \left[\frac{Kh}{1 - Kh} + \frac{K_1Kh + 2K_1K_2K^2h^2}{1 + K_1Kh + K_1K_2K^2h^2} \right] \quad [4]$$

where h is relative humidity (decimal) and the parameters W , K , K_1 , and K_2 depend on temperature T in °C:

$$W = 349 + 1.29T + 0.0135T_2 \quad [5]$$

$$K = 0.805 + 0.000736T - 0.00000273T_2 \quad [6]$$

$$K_1 = 6.27 - 0.00938T - 0.000303T_2 \quad [7]$$

$$K_2 = 1.91 + 0.0407T - 0.000293T_2 \quad [8]$$

2.4.5 Sorption hysteresis

The relationship between EMC and relative humidity at constant temperature is known as a sorption isotherm. Sorption hysteresis referring to the influence of wood history upon its EMC is shown in **Figure 9** by means of moisture content – relative humidity relationship under adsorption and various desorption conditions. Desorption isotherm is measured on initially wet wood that is brought to equilibrium by decreasing relative humidity (RH). An adsorption (resorption) isotherm is measured from the dry state by increasing RH values. Wood dried from the initial green condition below the fiber saturation point (initial desorption) shows greater EMC than in subsequent desorption isotherms. A midway between adsorption and desorption is represented by oscillating vapour pressure. (Glass and Zelinka, 2010)

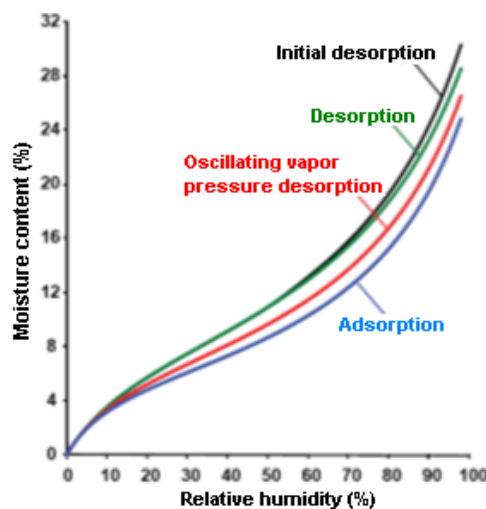


Figure 9 - Moisture content–relative humidity relationship for wood under adsorption and various desorption conditions (Glass and Zelinka, 2010)

2.4.6 Dimensional instability

Wood is dimensionally unstable when moisture content is lower than the fiber saturation point (MC_{fs}). This is because volume of the cell wall depends on the amount of bound water. Below MC_{fs} wood swells as it gains moisture or shrinks as it loses moisture. Shrinking and swelling usually result in warping, checking and splitting of the wood. (Glass and Zelinka, 2010)

Since wood is an anisotropic material, it shrinks and swells most in tangential direction, about half as much in radial direction and only slightly in longitudinal direction. Radial and tangential shrinkage can distort the shape of wood pieces because of the difference in shrinkage and the curvature of annual rings (**Figure 10**). (Glass and Zelinka, 2010)

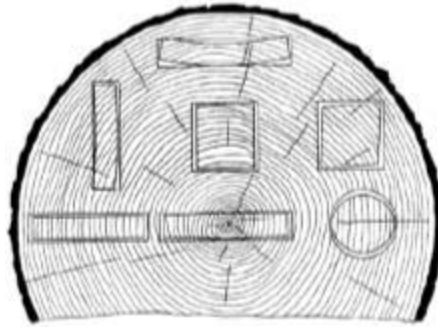


Figure 10 - Shrinkage and distortion of flat, square, and round pieces as affected by direction of growth rings (Glass and Zelinka, 2010)

Shrinkage from green to oven-dry MC (expressed as a percentage of the green dimension) for black spruce is in radial direction 4.1% and in tangential direction 6.8%. Average values for shrinkage are between 0.1% and 0.2% for most species of wood. Reaction wood (compression wood in softwoods or tension wood in hardwoods) and juvenile wood of some species tend to shrink excessively in longitudinal direction. They can shrink 2% from green to oven-dry. (Glass and Zelinka, 2010)

Moisture content-shrinkage relationship can be a linear function for a sufficiently small piece of wood (without moisture gradient) where shrinkage begins at about the fiber saturation point and continues linearly until the wood is dry. However, for a large piece of wood is typical a moisture gradient (the surface of wood dries first) and it begins to shrink when the surface MC drops below the fiber saturation point (in spite of the fact that the interior can still be wet and does not shrink). That is why moisture content - shrinkage relationship is not linear (**Figure 11**). (Glass and Zelinka, 2010)

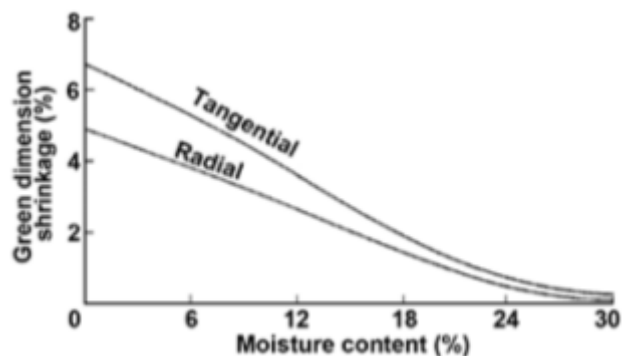


Figure 11 – Typical moisture content – shrinkage curve (Glass and Zelinka, 2010)

Changes in dimensions tend to be linear within the interval (5% – 20%)MC. For this range, change in dimension can be calculated from

$$h_2 = h_1 \left[1 + \frac{\beta}{100} + (w_2 - w_1) \right] \quad [9]$$

where h_1 and h_2 are the dimensions at moisture content w_1 and w_2 respectively. β is the coefficient of swelling (positive value) or shrinkage (negative value). (Glass and Zelinka, 2010)

The coefficient of volumetric movement β_V can be considered equal to the value of density times 10^{-3} (the volume of timber of density equal to 400 kg/m^3 swells 0.4% for each 1% increase in moisture content. As the coefficient of longitudinal movement β_0 is usually negligible, the coefficient

of transverse movement β_{90} is equal to $0.5\beta_V$. For most species, such as spruce, pine, fir, larch, poplar and oak, engineering values of β can be taken as $\beta_0 = 0.01$ and $\beta_{90} = 0.02$ where is considered as percentage movement for 1% change of moisture content. (Kuklík, 2008)

2.5 Mechanical properties of wood

This chapter shortly describes the most important mechanical properties of wood, such as elastic orthotropic properties (modulus of elasticity MoE, Poisson's ratio, shear modulus), non-elastic properties (failure types, stress-strain curves, fracture), fracture toughness and fracture energy, and strength properties.

2.5.1 Elastic orthotropic properties

Wood as an orthotropic material has unique and independent mechanical properties in the directions of three mutually perpendicular axes: longitudinal (L, parallel to fiber), radial (R, normal to the growth rings in radial direction), and tangential (T, perpendicular to grain and tangent to the growth rings), see **Figure 12**. (Kretschmann, 2010)

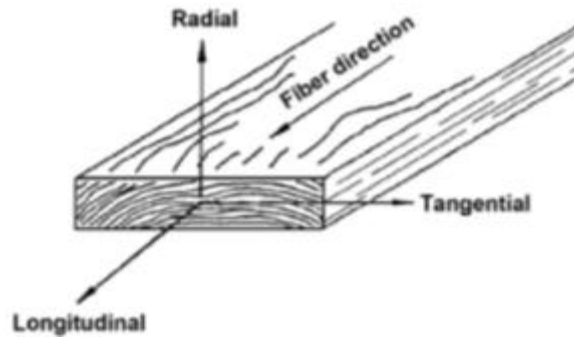


Figure 12 - Three principal axes (L – longitudinal, R – radial, T – tangential) of wood with respect to grain direction and growth rings (Kretschmann, 2010)

Elasticity implies that deformations produced by low stress are completely recoverable after loads are removed and the stress-strain relation is considered to be linear. When loaded to higher stress levels, plastic deformation or failure occurs.

Orthotropic material of wood in elastic region possessing three principal directions (L, R, T) in 3D can be described by Hooke's generalized law as follows:

$$\begin{pmatrix} \varepsilon_{LL} \\ \varepsilon_{RR} \\ \varepsilon_{TT} \\ \gamma_{RT} \\ \gamma_{LT} \\ \gamma_{LR} \end{pmatrix} = \begin{pmatrix} \frac{1}{E_L} & -\nu_{LR} & -\nu_{LT} & & & \\ \frac{E_L}{E_R} & \frac{1}{E_R} & \frac{E_L}{E_T} & & & \\ -\nu_{RL} & \frac{1}{E_R} & -\nu_{RT} & & & \\ \frac{E_L}{E_L} & -\nu_{TL} & \frac{1}{E_T} & & & \\ & & & & & \\ & & & & \frac{1}{G_{RT}} & 0 & 0 \\ & & & & 0 & \frac{1}{G_{LT}} & 0 \\ & & & & 0 & 0 & \frac{1}{G_{LR}} \end{pmatrix} \begin{pmatrix} \sigma_{LL} \\ \sigma_{RR} \\ \sigma_{TT} \\ \tau_{RT} \\ \tau_{LT} \\ \tau_{LR} \end{pmatrix} \quad [10]$$

or shorter as

$$\boldsymbol{\varepsilon} = \mathbf{C}\boldsymbol{\sigma} \quad [11]$$

or as the inverse relationship

$$\boldsymbol{\sigma} = \mathbf{D}\boldsymbol{\varepsilon}, \quad \mathbf{D} = \mathbf{C}^{-1} \quad [12]$$

where $\boldsymbol{\varepsilon}$ is the elastic strain vector, $\boldsymbol{\sigma}$ is the stress vector and \mathbf{D} is the material stiffness matrix, \mathbf{C} is the compliance matrix. E_L , E_R and E_T are the moduli of elasticity in longitudinal, radial and tangential direction, respectively. Parameters G_{RT} , G_{LT} , and G_{LR} are the shear moduli in the respective orthotropic planes. Parameters ν_{LR} , ν_{LT} , ν_{RT} , ν_{RL} , ν_{TL} and ν_{TR} are Poisson's ratios.

Compliance matrix is symmetric and thus

$$\frac{\nu_{RL}}{E_L} = \frac{\nu_{LR}}{E_R}, \quad \frac{\nu_{TL}}{E_L} = \frac{\nu_{LT}}{E_T}, \quad \frac{\nu_{TR}}{E_R} = \frac{\nu_{RT}}{E_T} \quad [13]$$

Finally, there are nine independent constants that are necessary for description of elastic behavior of wood (three moduli of elasticity E , three shear moduli G , and three Poisson's ratios ν).

Elastic moduli values depend on species, growth conditions, moisture content or temperature. Nevertheless, they can be generally related according to the following ratios (Bodig and Jayne, 1982):

$$\begin{aligned} E_L : E_R : E_T &\approx 20 : 1.6 : 1 \\ G_{LR} : G_{LT} : G_{RT} &\approx 10 : 9.4 : 1 \\ E_L : G_{LR} &\approx 14 : 1 \end{aligned} \quad [14]$$

The three moduli of elasticity (E_L , E_R , E_T) are usually obtained from compression tests. However, data for E_R and E_T are not extensive.

Poisson's ratio (ν_{LR} , ν_{LT} , ν_{RT} , ν_{RL} , ν_{TL} , ν_{TR}) represents ratio of the transverse to axial strain with respect to the load direction. The first letter of the subscript refers to direction of applied load and the second letter to direction of lateral deformation.

Two of the Poisson's ratios, ν_{RL} and ν_{TL} , are very small and are less precisely determined compared to other Poisson's ratios. Poisson's ratios vary within and between species and are influenced by moisture content and specific gravity.

The shear modulus (modulus of rigidity) relates the shear stress to engineering shear strain. The three shear moduli (G_{LR} , G_{LT} , G_{RT}) are the elastic constants in the respective planes. For example, G_{LR} is the shear modulus based on shear strain in the LR plane and shear stress in the same plane. The shear moduli vary within and between species and with moisture content and specific gravity. (Kretschmann, 2010)

2.5.2 Non-elastic properties

Wood behaves in a nonlinear way when loaded above the limit of proportionality (elastic region). Also, irreversible changes occur in the material. Similarly to elastic properties, non-elastic properties are influenced by density, moisture content, temperature, and duration of loading.

2.5.2.1 Failure types

Three basic failure patterns can be distinguished for compression perpendicular to grain according to growth rings orientation and direction of load: crushing of earlywood, buckling of growth rings and shear failure (**Figure 13**). (Gibson and Ashby, 1988)

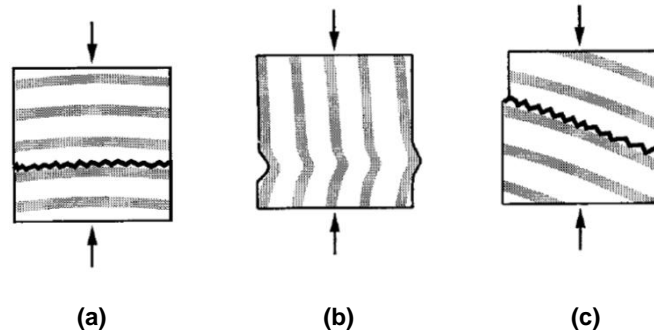


Figure 13 - Failure types in compression perpendicular to the grain: crushing of earlywood under radial loading (a), buckling of growth rings under tangential loading (b), shear failure under loading at an angle to the growth rings (c) (Gibson and Ashby, 1988)

Failure modes that occur during a compression test in longitudinal direction are crushing (the plane of rupture is approximately horizontal), wedge split, shearing (the plane rupture makes an angle of more than 45° with the top of the specimen), splitting (usually occurs in specimens having internal defects prior to test), compression and shearing parallel to grain (usually occurs in cross-grained pieces) and broomig or end-rolling (usually associated to an excessive MC at the ends of the specimen or improper cutting of the specimen), see **Figure 14**. The failure modes of splitting, compression and shearing parallel to grain and broomig or end-rolling are the basis for excluding the specimen from the set of measured results.

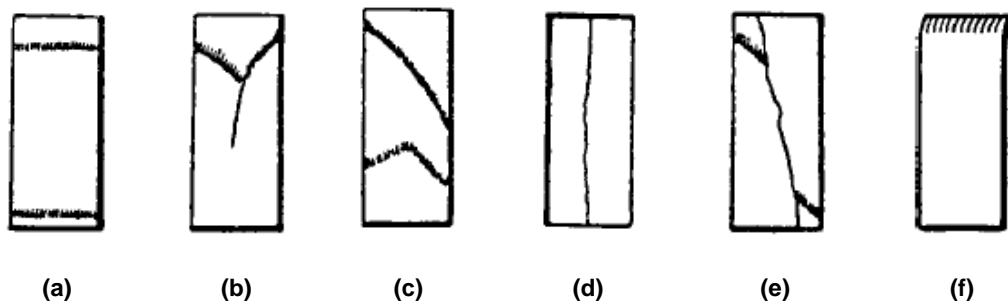


Figure 14 – Failure types in compression parallel to grain: crushing (a), wedge split (b), shearing (c), splitting (d), compression and shearing parallel to grain (e), broomig (end-rolling) (f) (ASTM D143-94)

Tensile loading perpendicular to the grain gives three failure patterns (similarly to compression perpendicular to grain, **Figure 13**):

- tensile fracture in earlywood (radial loading),
- failure in wood rays (tangential loading),
- shear failure along growth ring (loading at an angle to the growth rings).

Crack propagation for opening mode (I) can occur in two ways: cell-wall breaking (crack propagates across the cell wall) and cell-wall peeling (crack propagates between two adjacent cells), see **Figure 15**. (Gibson and Ashby, 1988)

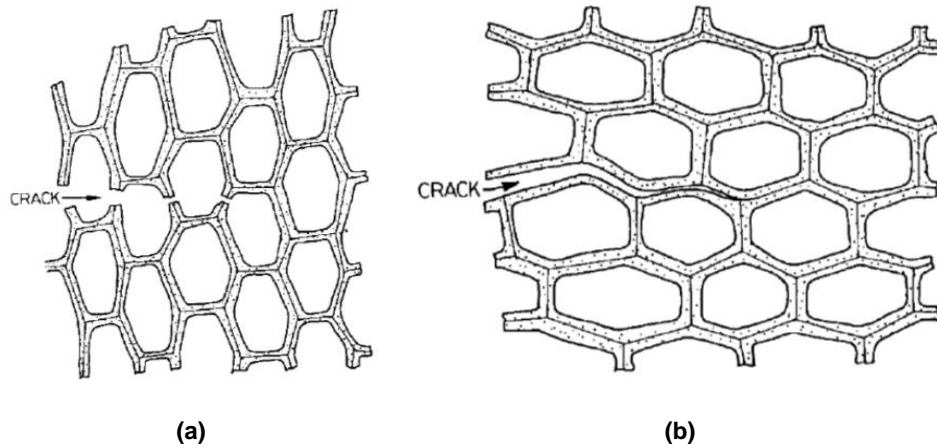


Figure 15 – Crack propagation for opening mode (I) loading: cell-wall breaking (a), cell-wall peeling (b) (Gibson and Ashby, 1988)

For tension parallel to grain, four failure types may occur, namely shear, a combination of shear and tension, pure tension, and splinter mode (Figure 16). (Feio, 2005)

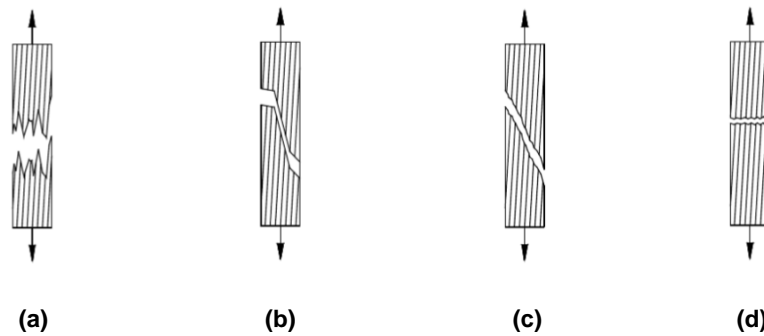


Figure 16 - Failure types in tension parallel to the grain: splinter (a), shear and tension failure (b), shear failure (c) and pure tension failure (d) (Feio, 2005)

2.5.2.2 Stress-strain curves

Typical stress-strain curves for dry wood loaded in longitudinal (L), radial (R) and tangential (T) direction in compression and in tension in L direction are presented in Figure 17. (Holmberg et al.,1998)

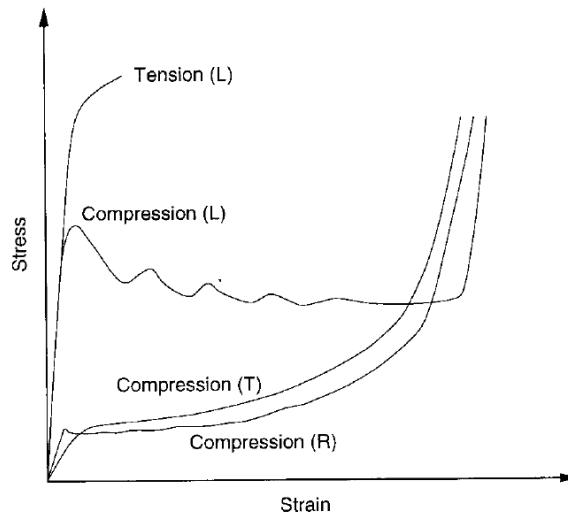


Figure 17 – Typical stress-strain curves for wood loaded in compression in L, R and T direction and for tension in L direction (Holmberg et al.,1998)

Development of the stress-strain curves in L, T and R (longitudinal, transversal and radial) compression show an initial elastic region, followed by a plateau region and a final region of rapidly increasing stress. The yield stresses for T and R compression are about equal and are considerably lower than L compression. R compression is characterized by a small drop in stress after the end of elastic region and it has slightly irregular plateau compared to the smooth plateau of T compression and serrated plateau region of L compression. (Holmberg et al.,1998)

2.5.2.3 Fracture

In fracture mechanics, three general fracture modes are defined: symmetric opening perpendicular to the crack surface (I), forward shear mode (II) and transverse shear mode (III), see **Figure 18**. Modes (II) and (III) involve antisymmetric shear separations. (Kretschmann, 2010)

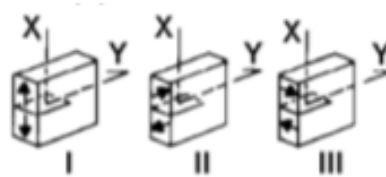


Figure 18 - Failure modes in wood: opening mode (I), forward shear mode (II) and transverse shear mode (III) (Kretschmann, 2010)

In wood, eight crack-propagation systems can be distinguished: RL, TL, LR+, LR-, TR+, TR-, LT, and RT. The first letter of the crack-propagation system denotes perpendicular direction to the crack plane and the second one refers to direction in which the crack propagates. The distinction between + and – direction arises because of the asymmetric structure of the growth rings, see **Figure 19**. For each of eight crack-propagation systems, fracture can occur in three modes and thus cracks in wood can arise in 24 different principal manners. (Kretschmann, 2010)

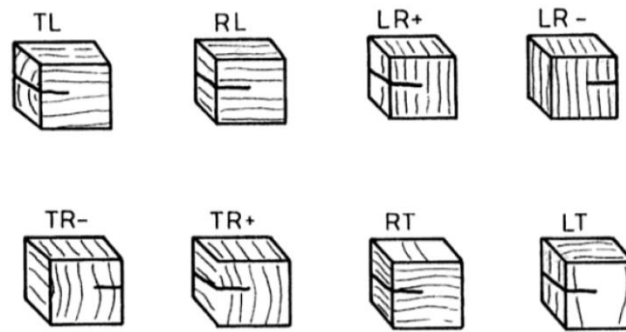


Figure 19 – Eight modes of possible crack propagation in wood (Gibson and Ashby, 1988)

It is suggested that fracture toughness is either insensitive to moisture content or increases as the material dries (until maximum at MC of 6% - 15%). Fracture toughness then decreases with further drying. (Kretschmann, 2010)

Mode I fracture characteristics of one softwood (spruce) and three hardwoods (alder, oak and ash) in the crack propagation systems RL and TL are presented in Reiterer et al. (2002). Wedge splitting test under loading perpendicular to grain was used (Figure 20). Testing arrangement is shown in Figure 21.

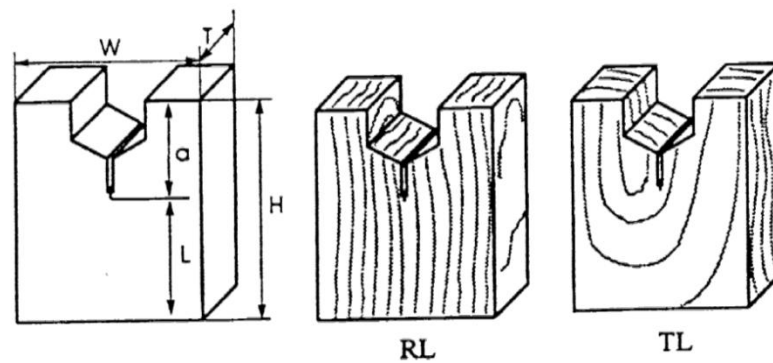


Figure 20 – Wedge splitting test: specimen geometry and grain orientation (RL, TL)

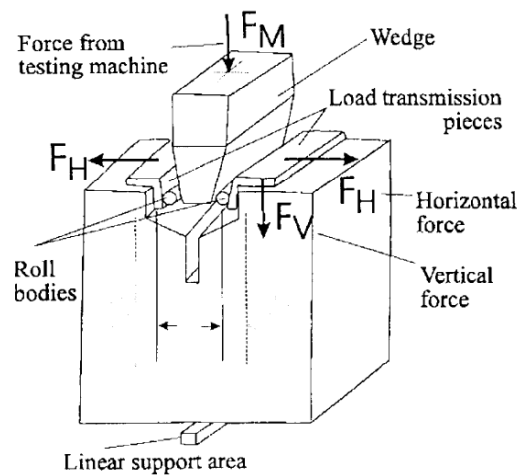


Figure 21 – Wedge splitting test: testing arrangement

The load-displacement curves for different crack propagation systems are presented in **Figure 22**. Spruce shows stable crack propagation until complete separation of the specimens. Hardwoods behave in a different manner: after macro-crack initiation at the maximum horizontal splitting force a sudden drop in the load–displacement curve occurs indicating unstable crack propagation. This drop is followed by crack arresting leading to another maximum. This is explained by the more brittle behavior of the hardwoods, which can be attributed to the fact that hardwood fibers are shorter than spruce fibers and energy dissipating processes (e.g. fiber bridging) are less effective. Also, less micro-cracks is formed during the crack initiation phase for the hardwoods which can be shown by means of acoustic emission measurements.

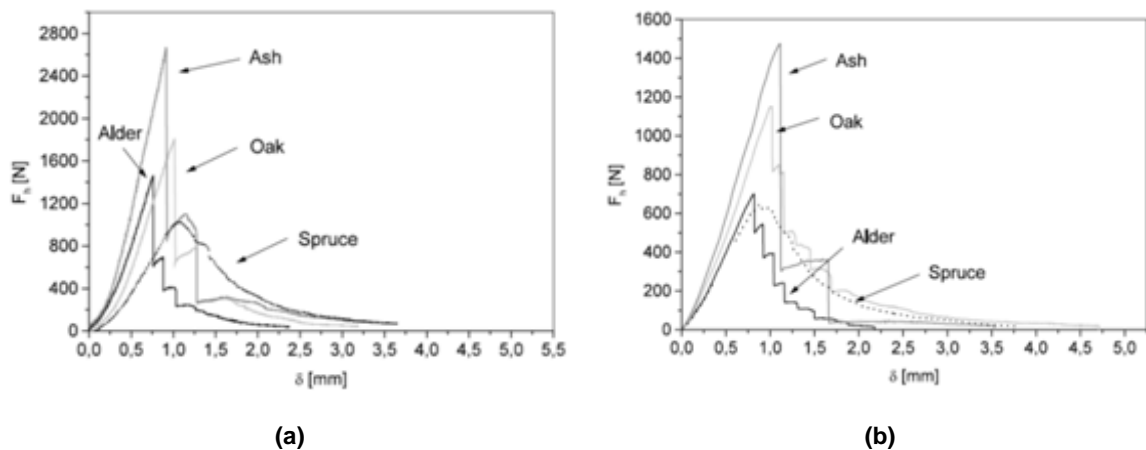


Figure 22 – Typical load-displacement curves obtained by the wedge splitting test in the RL (a) and TL (b) systems (Reiterer et al., 2002)

2.5.3 Fracture toughness and fracture energy

The fracture mechanics approach has three important variables: applied stress, flaw size, and fracture toughness while traditional approach to structural design has two main variables: applied stress and yield or tensile strength. In the latter case, a material is assumed to be adequate if its strength is greater than the expected applied stress. The additional structural variable in fracture mechanics approach is flaw size and fracture toughness. They replace strength as the relevant material property. Fracture mechanics quantifies the critical combinations of the three variables. (Anderson, 2005)

In fracture mechanics, fracture toughness is essentially a measure of the extent of plastic deformation associated with crack extension. Fracture toughness is measured by critical strain energy release rate G_c according to energy-balance approach or by critical stress intensity factor (SIF) K_c according to stress intensity approach. (Dinwoodie, 1981)

In case linear elastic fracture mechanics (LEFM) is involved, critical strain energy release rate G_c is equal to fracture energy G_f ($G_c = G_f$). Both variables are a material property that gives information about when a crack starts propagating. (Bostrom, 1992)

The forthcoming subchapters describe material properties G_c , K_c , G_f and a few examples of current test methods available for their determination.

2.5.3.1 Critical strain energy release rate G_c (energy-balance approach)

The energy approach assumes that crack extension (i.e. fracture) occurs when the energy available for crack growth is sufficient to overcome the resistance of the material. The material resistance may include the surface energy, plastic work, or other types of energy dissipation associated with crack propagation. This approach is based on energy release rate G which is defined as the rate of change in potential energy with the crack area for a linear elastic material. At the moment of fracture, energy release rate is equal to its critical value ($G = G_c$) which is a measure of fracture toughness. (Anderson, 2005)

For a crack of length $2a$ in an infinite plate (where width of the plate is $\gg 2a$) subjected to a remote tensile stress (Figure 23), the energy release rate is expressed by

$$G = \frac{\pi\sigma^2 a}{E} \quad [15]$$

where E is modulus of elasticity, σ is the remotely applied stress, and a is the half-crack length. If fracture occurs ($G = G_c$), the Eq. [15] describes the critical combinations of stress and crack size for failure:

$$G_c = \frac{\pi\sigma_f^2 a_c}{E} \quad [16]$$

The energy release rate G is the driving force for fracture while G_c is the material's resistance to fracture. Fracture toughness G_c is independent of the size and geometry of the cracked body and thus a fracture toughness measurement on a laboratory specimen should be applicable to a structure. These assumptions are valid as long as the material behavior is predominantly linear elastic. (Anderson, 2005)

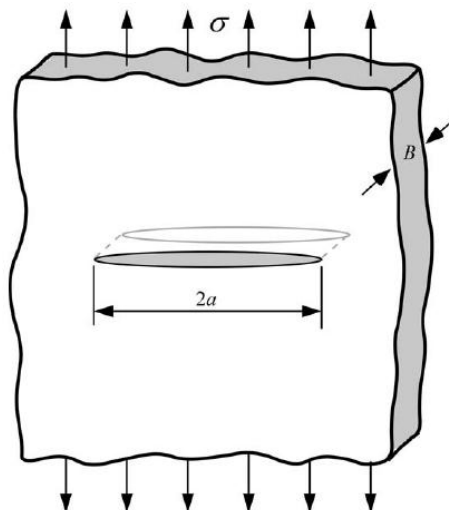


Figure 23 - Through-thickness crack in an infinite plate (plate width is $\gg 2a$) subject to a remote tensile stress (Anderson, 2005)

2.5.3.2 Critical stress intensity factor (SIF) K_c (stress intensity approach)

Stress intensity approach examines the stress state near the tip of a sharp crack and defines critical stress intensity factor K_c that is a fracture toughness measure and it can be used for normal-opening crack modes I and shear sliding modes II and III (K_{Ic} , K_{IIc} , K_{IIIc}). The text of this subchapter describes equations only for opening crack failure mode I. Figure 24 schematically shows an element near the tip of a crack in an elastic material, together with the in-plane stresses

on this element. Each stress component is proportional to stress intensity factor K_I for fracture mode I. If material fails locally at some critical combination of stress and strain, then fracture must occur at a critical stress intensity factor K_{Ic} . (Anderson, 2005)

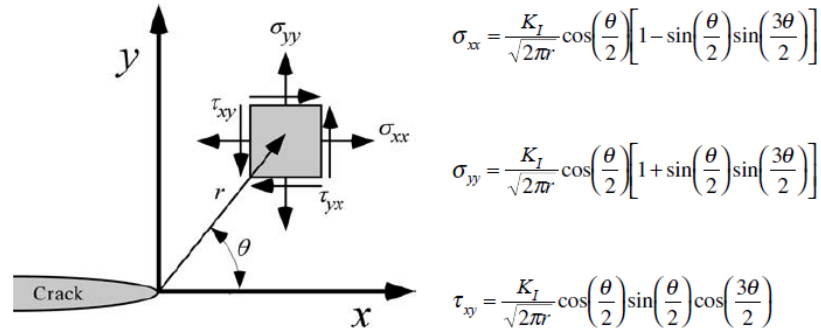


Figure 24 - Stresses near the tip of a crack in an elastic material (Anderson, 2005)

For an infinite plate (Figure 23), the stress intensity factor is given by

$$K_I = \sigma\sqrt{\pi a} \quad [17]$$

Failure occurs when $K_I = K_{Ic}$ (where K_I is the driving force for fracture and K_{Ic} is a measure of material resistance. K_{Ic} is assumed to be a size-independent material property. If we compare Eq. [15] and Eq. [17], we can derive relation between G and K_I

$$G = \frac{K_I^2}{E} \quad [18]$$

This same relationship holds for G_c and K_{Ic} . Thus, the energy and stress-intensity approaches to fracture mechanics are essentially equivalent for linear elastic materials. (Anderson, 2005)

2.5.3.3 Fracture energy G_F

Fracture energy [N/m] is an amount of energy required to form a unit area of a new crack in the material. For opening crack mode I $G_{F,I}$ can be defined as the area under the stress-displacement curve $t_n - \delta_n$ for the fracture process zone as follows

$$G_{F,I} = \int_0^{\delta_{n,crit}} t_n d\delta_n \quad [19]$$

where $\delta_{n,crit}$ is critical crack opening of the crack in normal direction to the crack [mm], δ_n is actual crack opening of the crack in normal direction to the crack [mm] and t_n is the stress acting in normal direction at the crack.

Similarly, fracture energy for pure shear mode II $G_{F,II}$ can be defined as the area under the stress-displacement curve $t_m - \delta_m$ for the fracture process zone as follows

$$G_{F,II} = \int_0^{\delta_{m,crit}} t_m d\delta_m \quad [20]$$

where $\delta_{m,crit}$ is critical crack opening of the crack in tangential direction to the crack [mm], δ_m is actual crack opening of the crack in tangential direction to the crack [mm] and t_m is the stress acting in tangential direction to the crack. (Bostrom, 1992)

2.5.3.4 Test methods for fracture toughness and fracture energy determination

Most specimens for experimental determination of the most important fracture parameters were originally developed for metals (Bostrom, 1992). Several experimental methods that are nowadays used for determination of fracture toughness and energy in wood are as follows:

- Double cantilever beam (DCB) test standardized for carbon fiber reinforced plastics (CFRP) in Japanese Industrial Standards (JIS) (JIS K7086-93, 1998) can be used for measurement of fracture toughness of timber. (Yoshihara and Kawamura, 2005)
- Three point bending test (TPB) according to RILEM and CIB-W18 recommendations (Larsen and Gustafsson, 1989) is classically used for determination of fracture energy in tension perpendicular to grain. (Daudeville, 1999)
- Testing methods based on the standard ASTM E399 (Plain-Strain Fracture Toughness of Metallic Materials) considers fracture mode I only. For the K_{I} test, a modification of the standard is proposed in Fonselius and Riipola (1992).
- Fracture toughness in opening fracture mode I can be determined from displacement fields obtained from digital image correlation for about 400 data points within a $7 \times 9 \text{ mm}^2$ area in front of the tip in conjunction with orthotropic fracture theory. (Samarasinghe, 1999)

2.5.4 Strength properties

Most commonly measured strength (mechanical) properties for design include modulus of rupture in bending, maximum stress in compression parallel or perpendicular to grain, and shear strength parallel to grain. Additional measurements evaluate work to maximum load in bending, impact bending strength, tensile strength perpendicular to grain, and hardness. These characteristics are shortly described in the following text.

- Modulus of rupture in bending reflects the maximum load-carrying capacity of a member in bending and is proportional to the maximum moment borne by the specimen. Modulus of rupture is valid only to the elastic limit.
- Compressive strength parallel or perpendicular to grain represents maximum stress sustained by a specimen with respective orientation of grain.
- Shear strength parallel to grain is the ability to resist internal slipping of one part upon another along the grain.
- Work to maximum load in bending represents ability to absorb shock with some permanent deformation. It is a measure of the combined strength and toughness of wood under bending stresses.
- Impact bending strength is measured in the impact bending test where a hammer of given weight is dropped upon a beam from successively increased heights until rupture occurs or the beam deflects 152 mm or more. The height of the maximum drop (that causes failure) is a comparative value that represents the ability of wood to absorb shocks that cause stresses beyond the proportional limit.
- Tensile strength perpendicular to grain is the resistance of wood to forces acting across the grain that tend to split a member.
- Hardness is generally defined as resistance to indentation using a modified Janka hardness test, measured by the load required to embed a 11.28-mm ball to one-half its diameter. (Kretschmann, 2010)

Among less common properties measured in clear wood is ranged torsion, fracture toughness, rolling shear. Other properties involving time under load include creep and duration of load, fatigue

strength, and creep under mechanical stress and moisture variations (mechanosorptive effect). These properties are briefly defined in the following text.

- Torsion strength is a resistance to twisting about a longitudinal axis. For solid wood members, torsional shear strength may be taken as shear strength parallel to grain. (Kretschmann, 2010)
- Fracture toughness is treated in Chapter 2.5.3.
- Rolling shear strength represents shear strength of wood where shearing force is in a longitudinal plane and is acting perpendicular to the grain. (Kretschmann, 2010)
- Creep and duration of load describes time-dependent deformation of wood under load. If the load is sufficiently high and the duration of load is long, failure (creep–rupture) will eventually occur. The time required to reach rupture is commonly called duration of load. (Kretschmann, 2010)
- Fatigue strength is resistance to failure under specific combinations of cyclic loading conditions: frequency and number of cycles, maximum stress, ratio of maximum to minimum stress, and other less-important factors. (Kretschmann, 2010)
- Mechanosorptive effect is apparent under simultaneous mechanical stress and moisture sorption cycling as creep is increased by moisture variations. This phenomenon also shortens the time to failure of timber. (Kuklík, 2008)

2.6 Natural defects affecting mechanical properties of wood

Clear straight-grained wood is used for determining fundamental mechanical properties of timber. Nevertheless, wood vary in its mechanical properties due to the following natural characteristics (defects): reaction wood, cross grain, knots, pitch pockets, and certain types of cracks. These properties must be taken into account in assessing actual properties of wood products.

2.6.1 Reaction wood

A tree will form reaction wood when the woody organ (e.g. a trunk, a branch) is deflected from the vertical by more than one or two degrees.

In softwoods, the reaction wood is formed on the underside of the leaning organ; this is called compression wood. In **Figure 25a**, we can observe that the pith is not in the center of the trunk with compression wood and the growth rings are much wider in the compression zone. In **Figure 25b**, there is a microscopic view of compression wood in softwood where the tracheids are typically thick-walled and round in outline. (Kretschmann, 2010)

In hardwoods, the reaction wood forms on the top side of the leaning organ; this is referred to as tension wood. In **Figure 25c** is shown a cross-section of tension wood in hardwood where the pith is nearly centered, but the growth rings are wider in the tension wood zone. **Figure 25d** represents a microscopic view of tension wood fibers in hardwood showing prominent gelatinous layers (most pronounced across the top of the image). (Kretschmann, 2010)

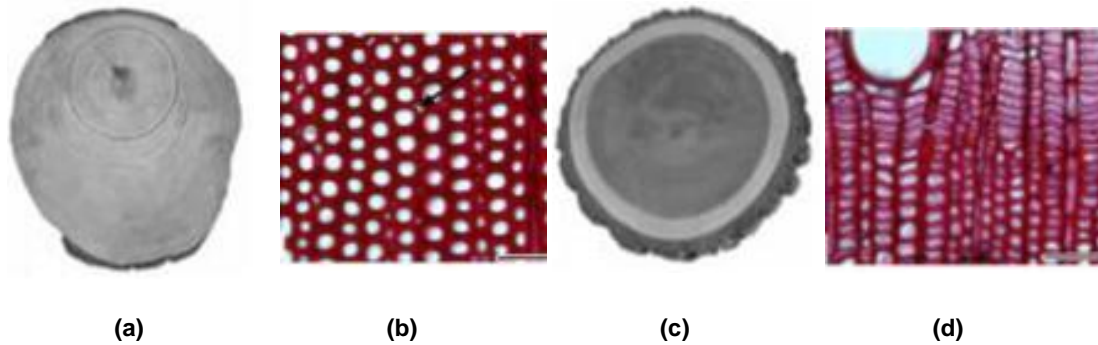


Figure 25 - Views of reaction wood: macroscopic transverse section of compression wood in softwood (a); microscopic view of compression wood in softwood (b), macroscopic transverse section of tension wood in hardwood (c), microscopic view of tension wood fibers (d) (Kretschmann, 2010)

Various features of juvenile wood and reaction wood are similar. In compression wood, the tracheids are shorter, misshapen cells with a large S2 microfibril angle and a high degree of longitudinal shrinkage. In tension wood, the fibers fail to form a proper secondary wall and instead form a highly cellulosic wall layer. Compression wood has the appearance of wider growth rings and a higher latewood portion than normal wood. (Kretschmann, 2010)

Timber containing an area of compression wood is liable to great distortion upon drying. As the compression wood is of higher density, there is no loss in mechanical properties. However, it exhibits a brittle failure in dry conditions. (Kuklík, 2008)

2.6.2 Cross grain

Cross grain is expressed by the term slope of grain that relates the fiber direction to the edges of a piece. Slope of grain indicates that the directions of important stresses may not coincide with the natural axes of fiber orientation in the wood. (Kretschmann, 2010)

Cross grain occurs in the form of spiral grain or diagonal grain. Spiral grain deviation is the case when the wood fibers form a helix around the stem instead of growing axially. This phenomenon is particularly pronounced in young trees. There is no way to saw a board from such a log to produce uniformly straight grain. (Kretschmann, 2010)

When the long edge of a board is not parallel with the grain, the board has what is called diagonal grain. Boards with diagonal grain will show atypical shrinking and swelling with changes in moisture content and altered mechanical properties with regard to the slope of grain. (Kretschmann, 2010)

2.6.3 Knots

Knots are remnants of branches in the tree appearing in sawn timber. Independent of the cut of the board, knots occur in two basic varieties: intergrown knots and encased knots. If the branch was alive at the time when the growth rings making up a board were formed, the wood of the trunk and that branch is continuous; this is referred to as intergrown knot (**Figure 26a**). If the branch was dead at the time when growth rings of a board were formed, knot is not continuous with the stem wood; this produces an encased knot (**Figure 26b**). Encased knots generally disturb the grain angle less than intergrown knots. (Kretschmann, 2010)

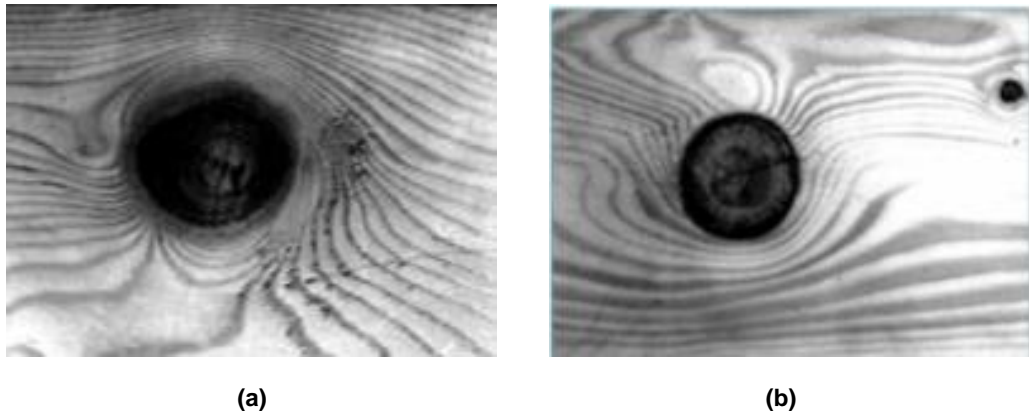


Figure 26 – Intergrown knot (a), encased knot (b) (Kretschmann, 2010)

In sections containing knots, most mechanical properties are lower than in clear straight-grained wood. The reasons for this are:

- the clear wood is displaced by the knot,
- the fibers around the knot are distorted, resulting in cross grain,
- the discontinuity of wood fiber leads to stress concentrations,
- checking usually occurs around the knots during drying,
- knots have a greater effect on strength in axial tension than in axial short-column compression. (Kretschmann, 2010)

2.6.4 Pitch Pockets

A pitch pocket is an opening that contains free resin. The pocket extends parallel to the annual rings. Pitch pockets are confined to certain species, such as pines, spruces, Douglas-fir, tamarack, and western larch. Change in strength of wood depends upon number, size, and location of a pitch pocket. A large number of pitch pockets indicates a lack of bond between annual growth layers. Piece with pitch pockets tends to suffer from shake or separation along the grain. (Kretschmann, 2010)

2.6.5 Cracks

Splits and cracks in wood are ruptures or separations in the grain of the wood which reduce strength and serviceability. There are two categories of natural origin of splits and cracks in wood: resource based and changing moisture content (MC) based.

Resource based splits and cracks occur in a standing tree or in a log as a result of environmental conditions, growth stresses or acting of various microorganisms. Ring shake which appears as longitudinal separation of wood fibers in the tangential direction can be ranged in this group.

Cracks in wood related to changing MC can be grouped as follows: cracks in drier environment than the timber MC (shrinkage), cracks in wetter environment than the timber MC and cycling environment. (Lamb, 1992)

3. Overview of current models of timber

There are currently many types of timber models. Some of them are concentrated on a specific timber construction member, e.g. layered timber beams (Kroflič et al., 2009), ribbed shell frameworks (Gliniorz et al., 2002), components and joints (Serrano and Gustafsson, 2005), timber composite beams with openings (Guan and Zhu, 2008), under specific conditions such as, growth stress formation and distortion of sawn timber (Ormarsson et al., 2008) and timber under fire (Frangi et al., 2009). Some of them are focused on analysis of general piece of wood under different conditions.

In the following subchapters are described a few models concerning the wood modeling where different approaches are taken: micro-macro modeling (Holmberg et al., 1998), models including moisture-induced stresses (Häglund, 2009; Fragiaco et al., 2011; Fortino et al., 2009; Turner, 1996), a model encompassing wood-drying, a model at large deformation taking into account brittle failure (Oudjene and Khelifa, 2009), and a model of fracture in spruce (Larsen and Gustafsson, 1989). In the end, the models of timber presented in this chapter are briefly summarized.

3.1 Micro-macro modeling of wood properties

Two types of models of timber that can be used for an analysis of timber in the refining process in mechanical pulp manufacture have been developed by Holmberg (1997, 1998). This application is a good illustration of modeling spanning from micro to macro scale. It involves large deformations, plasticity, damage and fracture.

Micro models of the cellular microstructure (micro level) are used for analysis of individual fibers deformation. They are very general with a very high degree of resolution, but they allow studying only very small pieces of wood. They are also difficult to handle with the computer resources available today. Compared to micro modeling, macro modeling (continuum modeling) is based on the average material properties that can be obtained from a micro model. It allows analysis of deformation and fracturing of large wood pieces. On the other hand, macro modeling does not permit analysis of the deformation and fracturing of the individual fibers. (Holmberg et al., 1998)

The micro-macro model is based on an experimental study of the defibration process (**Figure 27**) described in Holmberg (1997). The behavior of a specimen is characterized by development of cracks and by large volumetric changes in earlywood under compression. (Holmberg et al., 1998)

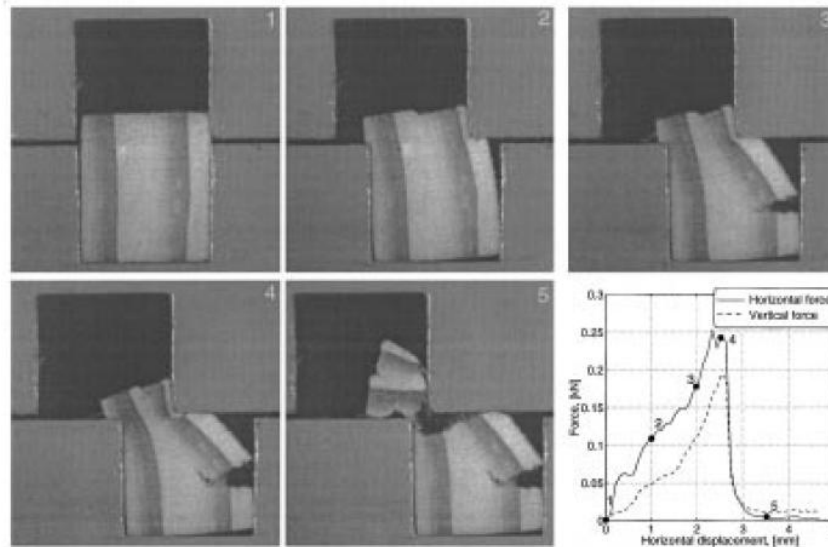


Figure 27 – Failure process in a 5 mm high wood specimen loaded perpendicularly to grain by steel grips (simulation of refiner discs during pulp production); Load-displacement (horizontal, vertical) curve (Holmberg et al., 1998)

3.1.1 Micro-mechanical approach

For the micro model of wood, equivalent stiffness and shrinkage were determined by a homogenization method. The basic equations are solved by means of finite element method (FEM). The equivalent properties were determined in steps presented in Figure 28.

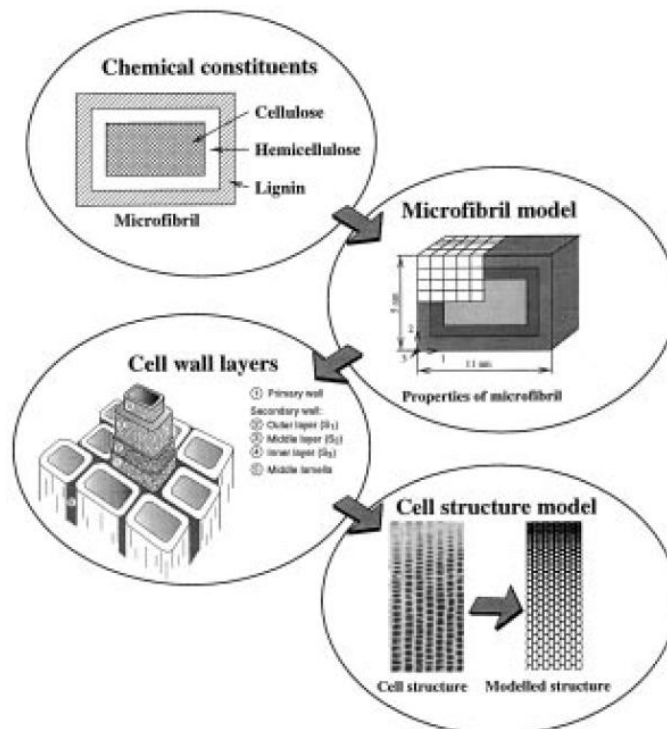


Figure 28 – Modeling scheme of micro-mechanical approach (Holmberg et al., 1998)

In the first step, equivalent properties of cell wall layers were calculated from the properties of cellulose, hemicellulose and lignin. Microfibril models were created for representing the different layers of the cell wall. FEM together with homogenization approach were used to determine the equivalent properties from these macrofibril models. Material stiffnesses were transformed in order to relate the local directions of microfibrils with the global L, R, and T directions. (Holmberg et al., 1998)

The aim of the second step was to determine the equivalent properties of wood structure. In this step, the cell structure was modeled by means of a five-parameter cell structure model with the most representative properties. For this purpose, 3D structures of complete growth rings composed of irregular hexagonal cells were created (**Figure 29a**). A model of a complete growth ring was obtained with respect to the density function and the radial widths of the cells (**Figure 29b**). Density and cell wall thickness were assumed to increase slightly linearly for earlywood, rapidly (quadratically) for transition zone and linearly in latewood zone. Cell width in radial direction was considered constant for the earlywood, decreasing for the transitionwood and constant in the zone of latewood. (Holmberg et al., 1998)

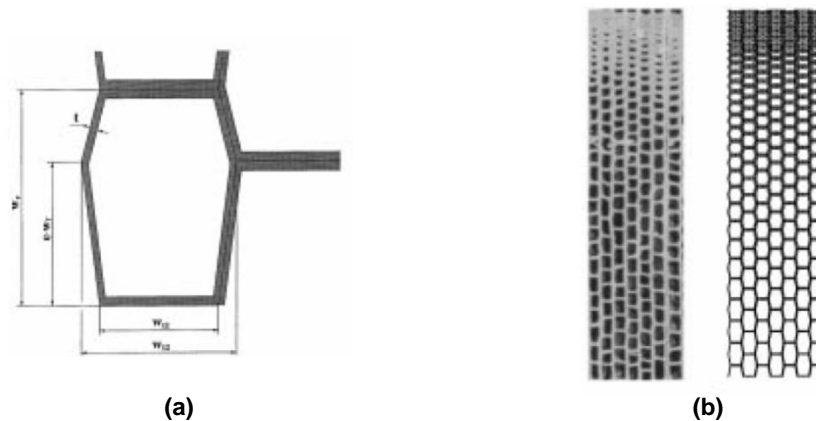


Figure 29 – Modeling of a growth ring: single-cell geometry (a), photographed and modeled cell structures (b) (Holmberg et al., 1998)

This approach cannot be used for simulation of complete cell structures of trees or boards because the models become very large. Nevertheless, parameters obtained by this model, such as average stiffness and shrinkage properties of growth rings with different radial widths and average densities, can be used in various analyses on larger scale, where it is efficient to model wood as an equivalent homogeneous continuum. (Holmberg et al., 1998)

To determine the global constitutive behavior of such equivalent homogeneous continuum, Holmberg et al. (1998) used homogenization procedure and FEM. To this goal, the wood was considered to be composed of subcells of equal shape and equal material properties (**Figure 30**). The periodic structure was divided into equal representative volume elements (base cells, substructures) for which equivalent smeared properties were derived.

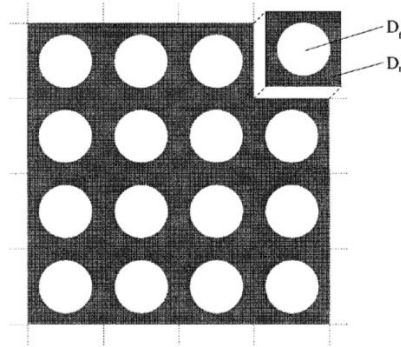


Figure 30 – A periodic structure with representative volume elements composed of two different materials D_f and D_m (Holmberg et al., 1998)

Ray cells with an average density of 400 kg/m^3 and a microfibril angle of the layer S2 of 10° were employed in the model. Properties of growth ring obtained by the above-discussed micro-mechanical approach were close to typical elastic stiffness and shrinkage data of spruce reported by Persson (1997). (Holmberg et al., 1998)

3.1.2 Continuum modeling approach

To analyze mechanical behavior of wood on structural element scale (macro modeling), it is desirable to model it as an equivalent continuum. However, it is necessary to take into account various damage phenomena, such as defibrillation (fracture propagating along wood fibers). In order to perform a proper model of initial defibrillation by means of a continuum model, Holmberg et al. (1998) considered the following characteristics of wood:

- variation in material properties within a growth ring,
- nonlinear inelastic response of earlywood subjected to compression perpendicular to the grain,
- fracture behavior of material. (Holmberg et al., 1998)

In the wood, two parts of growth ring (earlywood and latewood) should be considered in order to describe the variation in properties within a growth ring. The earlywood zone can be subdivided in several layers in radial direction that differ in strength and stiffness. The strain arising when earlywood is subjected to compression should be captured adequately. (Holmberg et al., 1998)

Holmberg et al. (1998) used a crushable foam model for earlywood behavior as the foams are able to deform volumetrically when subjected to compression. The model followed deSouza Neto et al. (1995) and it was based on non-associated compressible plasticity. (Holmberg et al., 1998)

Linear elastic behavior was considered for latewood as long as no cracks had developed.

The stiffness ratio of the radial to tangential direction is usually between 1.5 and 2.0. This ratio is based on conditions in which the material is considered as a continuum. Differences between radial and tangential directions concern only linear elastic part of the material behavior and thus only before the radial cell walls are buckled. For this reason, an isotropic foam model for loading perpendicular to the grain was adopted as reasonable simplification. Nevertheless, an orthotropic foam model should be used for more arbitrary loading conditions. (Holmberg et al., 1998)

Fictitious crack model was used for fracture of the material. The fracturing properties were associated with distinct cracking surfaces and were described by softening stress-relative displacement relations. The crack model was implemented in the finite element simulations by introducing special crack elements between the solid elements. (Holmberg et al., 1998)

In the finite element analysis, the problem was analyzed as constituting a two-dimensional static problem under plane strain conditions using an implicit integration scheme. Four-noded bilinear quadrilateral elements were employed for latewood. Three-noded linear triangular elements were used for earlywood as they are relatively less sensitive to large distortions. Large deformations in the earlywood were simulated by a formulation based on the Jauman stress rate and a logarithmic strain rate. Crack elements were introduced between the solid elements where tensile or shearing fracture criteria were attained. Subsequently, softening behavior was introduced.

A Coulomb friction model was used for the interface elements between the wood specimen and steel grips. The steel grips were modeled as rigid surfaces. A typical FE mesh that was used is shown in **Figure 31**.

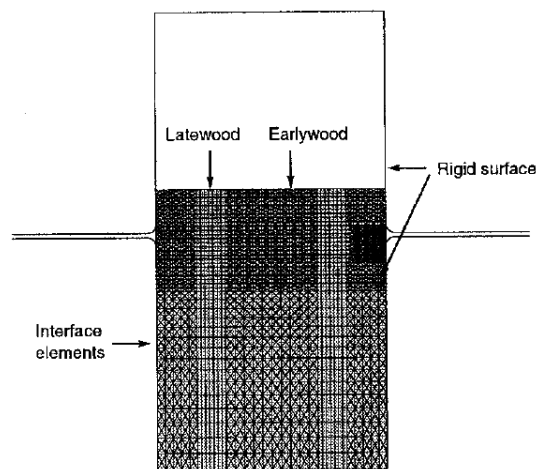


Figure 31 – A typical finite element mesh used in the simulations (Holmberg et al., 1998)

Two specimen types were described: the wood subjected to shear loading in radial and in tangential direction both in dry and wet conditions (**Figure 32**). The deformation and fracture process agree well with the experimental results. (Holmberg et al., 1998)

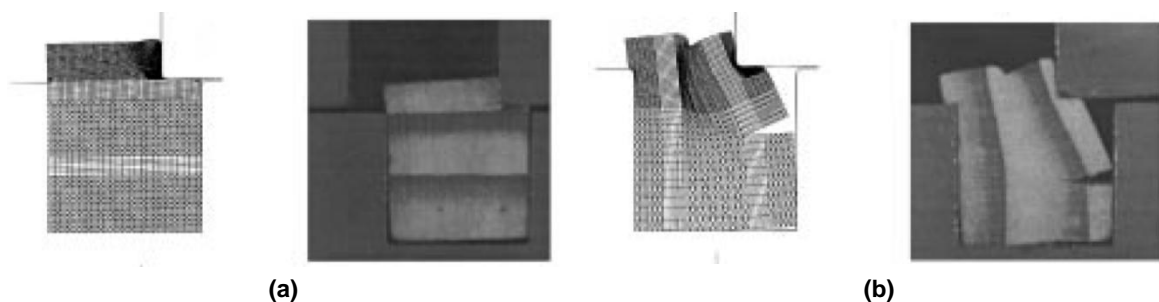


Figure 32 – Comparison between numerical simulation and experimental results: loading in tangential (a) and radial (b) direction (Holmberg et al., 1998)

3.2 Moisture induced eigen-stresses

Moisture content influences physical, mechanical, and rheological properties of wood (durability, shrinkage/swelling, modulus of elasticity, and strength properties). Another important factor is the moisture gradient that is created when the humidity load is variable or different from initial

equilibrium. Moisture gradients induce differences in shrinkage and swelling of wood, which further induce stresses in the wood sections (moisture-induced stresses) and may lead to cracks in the surface or in the central part of the wood sections. The rheological properties of wood, namely creep and mechanosorption have also an important role in the development of internal stresses as they generally decrease the stress magnitudes. Moisture actions on timber are nowadays described by advanced constitutive models.

This subchapter briefly describes one study and three models related to moisture induced eigen-stresses: parameter influence on moisture induced eigen-stresses (Häglund, 2009), moisture-induced stresses under different climates (Fragiacomo et al., 2011), 3D moisture-stress FEM analysis (Fortino et al., 2009), and 2D orthotropic model of wood-drying (Turner, 1996).

3.2.1 Parameter influence on moisture induced eigen-stresses

Moisture induced stress in timber is the result of a few factors. The moisture variation in the surrounding air causes induced stress due to restraint of hygro-expansion within timber elements. A parametric study of the input values of a constitutive model for moisture induced stress was carried out by (Häglund, 2009).

This study encompassed effects of beam size, indoor climate, surface coating and several other parameters. The moisture transport model was based on diffusion process. The calculations were run in a commercial FE program (ComsolMultiphysics) using a one-dimensional model. The wood material was treated as isotropic in the transversal directions. Recorded outdoor climate data was used as a basis for determining indoor relative humidity to represent boundary conditions. The model was validated against laboratory test results of a glulam beam sealed so as the moisture could be transported only perpendicularly to grain (1D).

This investigation confirmed that variation of moisture in the ambient air can cause high induced stresses due to hygro-expansion in timber elements. There is a risk of cracking when the value of induced stress is above the characteristic strength perpendicular to grain. Surface coating was shown to be effective in reducing hygro-expansion and induced stress. Given that the element is in equilibrium during the application of coating, higher stress cannot develop.

The cross-sectional size also affects the distribution and magnitude of the stresses. In general terms, higher maximum stress levels are induced in large widths cross-sections than in small ones. Häglund (2009) questioned whether the Maxwell mechano-sorptive stress model was applicable under conditions with externally applied tensile forces because the results indicate that the applicability does not encompass external loading. Effects of moisture are size dependent and should be considered to help improve the design of timber structures. Influences of other parameters are summarized in **Table 1**. (Häglund, 2009)

Table 1 – Comments on the response of different parameters (Häglund, 2009)

Parameter	Resulting effect on induced stress
<i>Cross-section</i>	See text above.
<i>Restraint</i>	Indication on minor effect. However, difficult to draw any deeper conclusion since complete restraint here defines an ideal situation which is seldom or never found in actual constructions. Restraint caused by, e.g., connectors lies somewhere between no and complete restraint.
<i>External force (stress)</i>	The result is difficult to evaluate since representative cross-sectional measurements for validation of the Maxwell-type mechano-sorptive model under tensile stresses is lacking. It is seen that the applied stress cannot simply be superposed (not even approximately) but whether it is an inherent false effect of the model, or a proper description of the actual response of timber, cannot be concluded without further experiments.
<i>Moisture capacity</i>	Does not show to have any major effect. In literature, the numerical values vary and there are more or less complicated functions describing its variation, but here it is indicated that the importance is low.
<i>Mass transfer coefficient</i>	Significant effect. Lowering the coefficient by, e.g., paint plays an important role in reduction of stress levels.
<i>Indoor moisture production</i>	Minor effect. The average amount of indoor moisture production is however most likely negligible in comparison with effect of <i>changes in production</i> from day to night, or between working days and weekends.
<i>Hygroexpansion (α)</i>	Major effect with a strict proportional response ($\sigma \propto \alpha$). This was expected as the stress model states a linear relation between moisture content and hygroexpansive strain.
<i>Mechano-sorption (m and β)</i>	Minor to moderate effect. Decreasing m leads to higher stress in the middle but otherwise the stresses falls within $\pm 20\%$. In case the mechano-sorptive effect did not exist the stress would be significantly higher (it can be seen as a sort of a stress-relaxing effect which hinders the development of moisture induced stress)
<i>MOE</i>	Resembles the results for the hygroexpansion but with less influence and no strict proportionality.

3.2.2 Moisture-induced stresses under different climates

Main parameters affecting moisture-induced stresses such as type of climate, size of timber cross-section, and type of protective coating are investigated by Fragiacomano et al. (2011). For this purpose, Europe was considered to be divided into a number of climatic regions. For each of them were identified relative humidity and temperature histories. Also, characteristic and mean values of yearly and daily variations were calculated.

A 3D FEM was implemented in ABAQUS software. The model was based on the orthotropic viscoelastic–mechanosorptive material model presented by Fortino et al. (2009) and a combination of Fickian moisture transfer model that was used to compute the moisture distribution and a mechanical model for time-dependent behavior of wood by means of which the corresponding stress distribution was calculated. Moisture content and stress distribution were computed on different timber cross-sections (protected with different types of coating) exposed to the climatic regions. (Fragiacomano et al., 2011)

It was found that the variation of moisture results in stresses of magnitudes that would probably cause cracking of wood in the perimeter of any uncoated cross-section size. The use of a protective coating, however, reduces considerably the moisture-induced stresses, and it can be regarded as an effective protective measure to avoid cracking due to humidity variations. Regarding European climates, Northern climates result in higher surface tensile stresses than Southern climates. (Fragiacomano et al., 2011)

3.2.3 A 3D moisture-stress FEM analysis

A 3D moisture-stress numerical analysis for timber structures under variable humidity and load conditions was developed by Fortino et al. (2009). Both the constitutive model of an orthotropic viscoelastic-mechanosorptive material and the equations needed to describe the moisture flow across the structure were implemented into user subroutines of the ABAQUS FE code. Coupled moisture-stress analysis was performed for several types of mechanical loads and moisture changes. This computational approach was validated by wood tests described in the literature and by comparing the computational results with the reported experimental data.

The constitutive model was based on the 1D model for wood in longitudinal direction and on the 1D model for wood in the perpendicular to grain direction. For both the viscoelastic and the

recoverable mechanosorptive mechanisms, Kelvin elements were used and for irrecoverable mechanosorption a mechanosorptive dashpot scheme is also taken into account. The above creep mechanisms are added to the elastic strain and to the hygroexpansion strain. The temperature was considered to be constant during the studied cases. (Fortino et al., 2009)

The extension of the previous 1D constitutive creep models to 3D was done by writing the problem in a thermodynamic form. 3D elemental compliance matrices were defined for each element of the different creep mechanisms and an algorithm for updating the total stress was used. This computational approach is very general and can also be used for other types of materials where the creep mechanism is described by Kelvin elements. (Fortino et al., 2009)

The constitutive model and the algorithm for stress update were implemented into the UMAT subroutine of the FEM code ABAQUS. The equation describing the flow across the surface was implemented into the user subroutine DFLUX. A coupled moisture-stress analysis was performed by using the analogy with the available temperature-displacement analysis of ABAQUS. (Fortino et al., 2009)

The computational results fitted relatively well the experimental curves for both grain direction and cross grain section. However, more experimental data are needed in order to define viscoelastic and mechanosorptive compliances fully independent of the particular studied case. Both the material model and the computational method can be directly used for analyzing problems in which the effect of temperature is significant. In this case a thermal analysis and the described coupled moisture-stress analysis can be solved sequentially by using the computational tools of ABAQUS. (Fortino et al., 2009)

3.2.4 2D orthotropic model of wood-drying

Wood must be dried before it can be manufactured. Drying is important for the protection of the wood against biological damage and the reduction of the moisture content to final equilibrium levels. In order to allow a numerical investigation of the convective drying of wood, a two-dimensional (2D) orthotropic mathematical model was formulated by Turner (1996). The numerical code of the 2D model was based on a structured mesh cell centered control volume approach.

The modeling of the drying process consists of analyzing the heat and mass transfer phenomena that arise in an anisotropic, nonhomogeneous, and hygroscopic porous medium of wood.

A comparison between two different numerical solution techniques was made. The first numerical method solved the system of equations by treating each equation in an uncoupled form, while the second scheme solved the entire system as a completely coupled set. The most efficient numerical algorithm was obtained when the system was solved using the coupled procedure.

The overall kinetics for both low and high temperature drying was examined. Three different cases of convective drying of wood were considered: the drying of wood below the boiling point at the temperature of 50°C, 80°C, and above the boiling point at the temperature of 120°C.

The 2D model highlights two important facts. First, for an anisotropic medium, where the ratio between longitudinal and transverse permeability is of the order of 10^3 the moisture migration occurs in the longitudinal sense. Second, the behavior of the internal gaseous pressure can have a substantial impact on moisture migration. (Turner, 1996)

3.3 FEM at large deformations and brittle failure prediction

A constitutive model of wood based on both hardening associated with material densification at large compressive deformations and brittle failure modes was developed by Oudjene and Khelifa (2009). Coupling between the anisotropic plasticity and the ductile densification was considered.

The model was implemented in the commercial software ABAQUS and its validation was performed by means of uniaxial compressive test in longitudinal and radial direction and three-points bending (TPB) test.

Material parameters (elasticity, plasticity hardening, densification) were determined using experimental data (stress-strain curves) obtained from uniaxial compression tests in longitudinal and radial direction. Distinction between radial and tangential planes was disregarded. In two-dimensional finite element model was assumed isotropic behavior in the transverse direction (radial and tangential). (Oudjene and Khelifa, 2009)

The coupled model is well suited for analysis with large compressive deformations perpendicular to the grain. The behavior is accurately predicted until 25% of deformation by both the coupled and the uncoupled cases. The densification effect occurs beyond this limit and is well predicted by the coupled model while the uncoupled one provides fairly good agreement with the experiment. (Oudjene and Khelifa, 2009)

The coupled, uncoupled and linear elastic models give almost the same results in linear load-displacement curves as the experiment in bending until a final failure. Hence, the effect of the densification should be neglected since the plastic behavior is not significant. Linear elastic material model is more accurate for the behavior after reaching the compressive yield stress in perpendicular direction than coupled or uncoupled models. (Oudjene and Khelifa, 2009)

The results obtained from the uniaxial compressive test demonstrate the capability of the model to simulate the wood behavior at large compressive deformations and show clearly the effect of the densification on the plastic behavior. The results obtained from the three-points bending test show a good implementation of the brittle failure criterion and demonstrates the suitability of the developed model to analyze and design wooden structures. (Oudjene and Khelifa, 2009)

3.4 Fracture in spruce: damage and linear mechanics

Linear elastic fracture mechanics (LEFM) and damage mechanics (DM) methods were compared in a simulation of three point bending (TPB) test in spruce using FEM by Daudeville (1999).

The LEFM is a theory used for the analysis of brittle materials (metals, ceramics) where all damage phenomena are assumed to be concentrated at the crack tip. The DM treats the problem of fracture in materials that exhibit softening behavior (i.e. quasi-brittle materials). (Daudeville, 1999)

The TPB test (**Figure 33**) was used for the determination of the fracture energy (G_f) in tension perpendicular to grain according to RILEM and CIB-W18 recommendations (Larsen and Gustafsson, 1989). TPB tests were performed in order to obtain a stable crack extension in TL (tangential-radial) and TL (tangential-longitudinal) planes from an initial notch to the complete separation of both crack faces. (Daudeville, 1999)

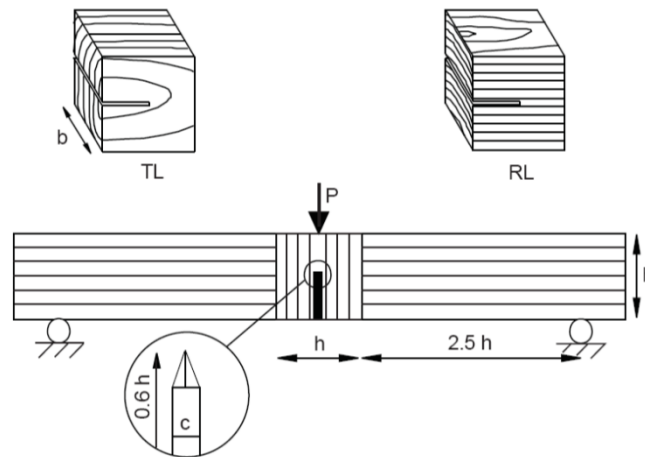


Figure 33 – Three point bending test (Larsen and Gustafsson, 1989)

The TPB test was performed for the mode I fracture analysis. It was carried out first for the determination of fracture energy with respect to wood orientation for a fixed beam width and depth ($h = b = 45$ mm). The influence of variations in beam depth ($h = 45, 67, 100$ mm) with the fixed beam width on the nominal stress was examined. (Daudeville, 1999)

The finite element method (FEM) was used for the analysis of crack propagation. The critical energy release rate (G_c) and fracture energy per unit cracked area (Y_f) were computed from maximum load. (Daudeville, 1999)

Comparisons between simulation results with LEFM and experimental results of the TPB test have shown that LEFM could predict the load-displacement curve but the critical energy release rate G_c could not be equal to the fracture energy G_f . The load-deflection curve is correctly predicted by the DM model. Furthermore, it was shown that the fracture energy G_f was the major parameter that governs fracture propagation in linear (large structures) or in non-linear (small structures) fracture studies and it is not size dependent. (Daudeville, 1999)

3.5 Summary

This chapter briefly summarizes the above-mentioned current model of timber in the context of the constitutive model developed in this work.

The constitutive model developed in this work was inspired by continuum modeling approach described in Holmberg (1997, 1998). That is why the part of micro-macro modeling is treated in more detail than other modeling approaches of timber.

Common features of the constitutive model developed in this work and that of Holmberg (1997, 1998) are as follows:

- mechanical behavior of wood on structural element scale (macro modeling) is modeled as an equivalent continuum,
- wood is regarded as an orthotropic material,
- fictitious crack model for fracture of timber is involved,
- both models can be used for simulation of timber behavior in construction members or details.

On the other hand, the aspect of variation in material properties within a growth ring is disregarded. The model developed in this work can be further enhanced by implementation of other modeling approaches such moisture induced eigen-stresses, wood drying or large deformations. For a

thorough validation of the model should be obtained experimental data that would contain also fracture properties of wood.

4. Constitutive model for timber under tension and shear

A two-dimensional homogeneous constitutive model for mechanical behavior of timber under tensile and shear loading is developed in this work. This model covers the following phenomena:

- elastic and inelastic behavior,
- material orthotropy, both in linear and non-linear range,
- fracture across and along fibers,
- behavior under unloading/reloading is considered to a certain extent,
- only small deformations (lower than 0.05ε) are considered,
- the model can be applied both to hardwood and softwood by selecting appropriate material characteristics.

Within the scope of the present work, we do not consider non-linear behavior and failure of timber under compression. However, the proposed fracture model is ready to be extended to this range, for example, by combining it with plasticity in analogy with the fracture-plastic model developed for concrete by Červenka and Papanikolaou (2008).

A constitutive model in general expresses how a material responds to acting stress. In the present study we idealize timber as a quasi-brittle material. Thus, the material is considered as a continuum with discontinuities (cracks). The continuous part is characterized by a stress-strain law while a traction-separation law describes the behavior of the discontinuities. Fixed smeared crack model is used to represent the fracture.

Finite element method (FEM) is a universal numerical technique applicable to problems with arbitrary geometry and boundary conditions. It is the core of the most of the commercial software packages for engineering computations. The constitutive model proposed in this work is intended to be a basis for a material subroutine of a finite element code. Within the scope of this thesis, the developed model is implemented in a MATLAB computer code to that extent that it calculates stress and tangent material stiffness matrix corresponding to a given strain state (which is attained by a prescribed sequence of increments) at the level of a material point (or integration point in FEM model). The prescribed strain path may involve non-proportional change of strain components, loading and unloading/reloading cycles.

After full implementation into a finite element code, this model can be used as a basis for the following advanced approaches to analysis of timber members:

- A model that can account for the presence of inhomogeneities such as knots. For this purpose, the present model would be used to represent clear timber while the inhomogeneities would be modeled as discrete regions with different properties. This approach may further require representation of the interface between two materials.
- A model that can take into account an influence of moisture (wood drying, moisture induced stresses), which would be assigned as initial stress or eigen-strain. To this end, the moisture distribution would have to be analyzed separately using suitable transport model.

The following text of this chapter deals with aspects regarding the constitutive model developed in this work such as principal assumptions of the model, elastic orthotropy, failure criterion, crack types, smeared crack model and its application in the model, cohesive law, critical crack opening, crack unloading/reloading cycle, characteristic length, transformation between coordinate systems, computational Newton-Raphson method, code scheme and in the end are summarized input data.

4.1 Assumptions

The 2D constitutive model for timber developed in this work is based on the following assumptions:

- Wood is regarded as homogeneous material.
- Prior to cracking, wood obeys rules of elastic orthotropy (chapter 4.2).
- In the proposed 2D model, axes of orthotropy are reduced from 3D space (x,y,z) respectively (R,L,T) to 2D space (x,y) respectively (R,L) . Thus, the direction x corresponds to parallel to grain (longitudinal) direction (L), y corresponds to perpendicular to grain radial direction (R), and in case of 3D z corresponds to perpendicular to grain tangential direction (T), see **Figure 34**. This implies that for the proposed 2D model is considered xy respectively RL plane.

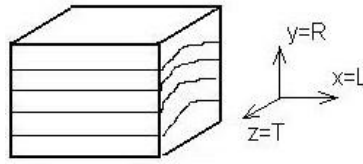


Figure 34 – 2D coordinates in the context of 3D coordinates: longitudinal ($x = L$), radial ($y = R$) and tangential ($z = T$) direction

- A crack is initiated along the fibers or across the fibers and after its initiation, the crack direction is fixed. Treshold angle defines a limit value of principal stress deviation from the grain and specifies which crack type (along or across the grain) is initiated. The crack along the fibers is always initiated in the longitudinal direction while the crack across the fibers is always perpendicular to the principal stress. Only one crack exists at a material point.
- In timber is assumed an equivalent computational crack that is perfectly planar. Nevertheless, in real material of timber, the crack is not planar and it can be accompanied by micro-cracks of different sizes, shapes and orientations.
- The post-cracking behavior is described by a cohesive response at the initiated crack.

4.2 Elastic orthotropic 2D model

Elastic orthotropic properties are described for 3D space in chapter 2.5.1. In 2D space, Hook's law for an orthotropic material of wood in elastic region possesses two principal directions (L, R) and can be expressed as follows:

$$\begin{pmatrix} \varepsilon_{xx} \\ \varepsilon_{yy} \\ \gamma_{xy} \end{pmatrix} = \begin{pmatrix} \frac{1}{E_x} & \frac{-\nu_{xy}}{E_y} & 0 \\ \frac{-\nu_{yx}}{E_y} & \frac{1}{E_x} & 0 \\ 0 & 0 & \frac{1}{G} \end{pmatrix} \begin{pmatrix} \sigma_{xx} \\ \sigma_{yy} \\ \tau_{xy} \end{pmatrix} \quad [21]$$

Finally, there are four independent constants that are necessary for description of elastic behavior of wood in 2D (two moduli of elasticity E , one shear modulus G , and one Poisson's ratio ν).

4.3 Failure criterion

Failure criterion defines conditions under which a crack is initiated in a material. In the proposed model, a function of failure criterion (crack initiation criterion) f_{cic} is derived from the standard Rankine failure criterion that is defined as follows

$$f(\sigma) = \sigma_{\max} - \sigma_t = 0 \quad [22]$$

where required maximum stress σ_{\max} in any direction (maximum principal stress) is to be equal to tensile strength σ_t . Rankine yield surface in the principal stress space in 2D is shown in **Figure 35**.

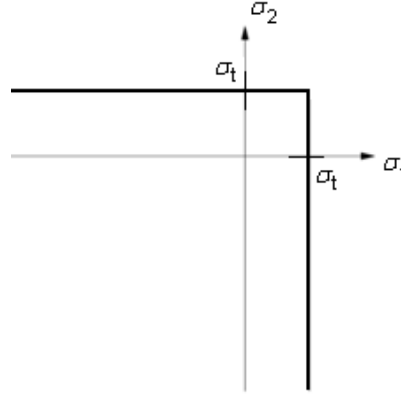


Figure 35 – Rankine yield surface in the principal stress space in 2D

Rankine criterion can be expressed by a single function of the first principal stress and tensile strength (σ_t) in the corresponding direction

$$f_1 = \frac{(\sigma_x + \sigma_y)}{2} + \sqrt{\left(\frac{(\sigma_x - \sigma_y)}{2}\right)^2 + \tau_{xy}^2} - \sigma_t \quad [23]$$

To account for orthotropic material properties of timber, we modify the Rankine criterion following Lourenço et al. (1997). The function of crack initiation criterion f_{cic} is in the proposed model defined as follows

$$f_{cic} = \frac{(\sigma_x - f_{tx}) + (\sigma_y - f_{ty})}{2} + \sqrt{\left(\frac{(\sigma_x - f_{tx}) - (\sigma_y - f_{ty})}{2}\right)^2 + \alpha \tau_{xy}^2} \quad [24]$$

where f_{cic} is the crack initiation function, σ_x , σ_y and τ_{xy} are stress components, f_{tx} and f_{ty} are uniaxial tensile strengths in x and y direction (parallel and perpendicular to fibers, respectively). Parameter α controls the shear stress contribution to the failure and reads

$$\alpha = \frac{f_{tx} f_{ty}}{f_s^2} \quad [25]$$

where f_s is shear strength.

The value of the function of crack initiation criterion f_{cic} refers to elastic or crack initiation state of the material, see **Table 2**.

Table 2 – Status of material defined by the crack initiation criterion (value of f_{cic})

Status	Elastic	Crack initiation
Criterion	$f_{cic} < 0$	$f_{cic} = 0$

For the crack initiation state, the function $f_{cic}(\sigma_x, \sigma_y, \tau_{xy}) = 0$ is shown in **Figure 36** as a failure surface by means of expressing $\tau_{xy}(\sigma_x, \sigma_y)$.

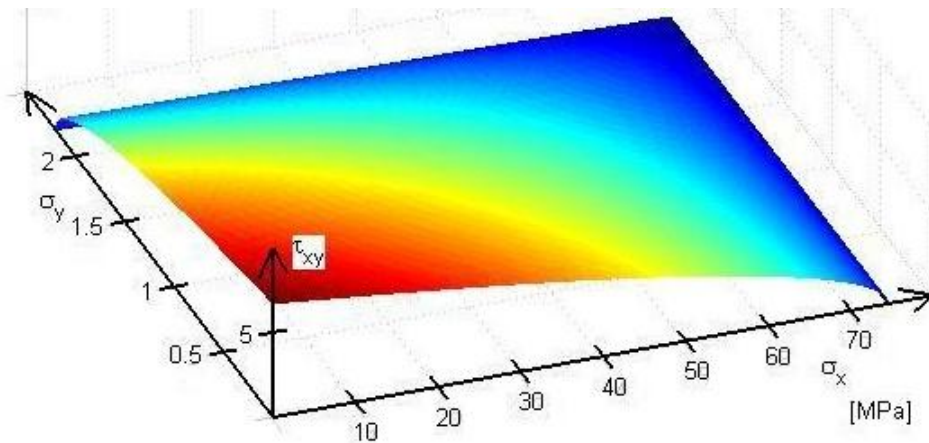


Figure 36 – Visualization of the of failure surface $f_{cic}(\sigma_x, \sigma_y, \tau_{xy}) = 0$ by means of $\tau_{xy}(\sigma_x, \sigma_y)$ for $\tau_{xy} \geq 0$ for spruce (*Picea abies*)

Failure surface can be also visualized for $\sigma_x = 0$, $\sigma_y = 0$ and $\tau_{xy} = 0$ (Figure 37). In this figure is shown that τ_{xy} decreases with increasing σ_y (Figure 37a) which means that for increasing σ_y suffices smaller and smaller τ_{xy} to initiate a crack. A similar assumption is made in the case of τ_{xy} and σ_x (Figure 37b). If $\tau_{xy} = 0$, σ_y is constant with increasing σ_x until ultimate strength in x direction (f_{tx}) is reached (Figure 37c).

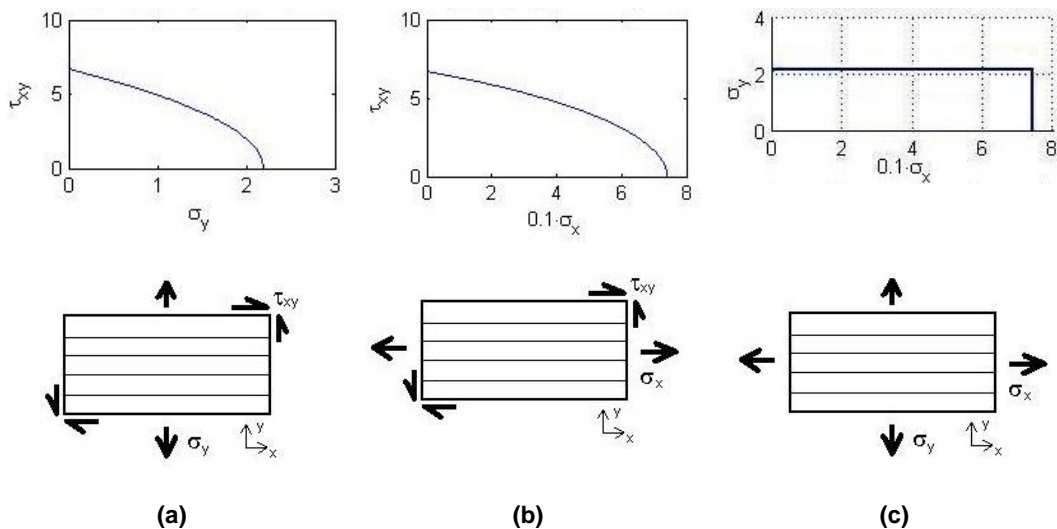


Figure 37 – Visualization of failure surface $f_{cic}(\sigma_x, \sigma_y, \tau_{xy}) = 0$ and a respective loading for spruce (*Picea abies*) for $\sigma_x = 0$ (a), $\sigma_y = 0$ (b) and $\tau_{xy} = 0$ (c)

4.4 Crack types

In the proposed 2D fixed crack model, two crack types are considered: crack across the fibers (CT1) and along the fibers (CT2).

The crack type CT1 includes cracks across the fibers that are initiated under loading where maximum principal stress (σ_1) is deviated from the x direction by crack normal deviation angle $0^\circ \leq \theta \leq \theta_{CT1,max}$, e.g. pure longitudinal loading in tension (σ_x). Crack type is limited by threshold

angle $\theta_{CT1,max}$. As the crack CT1 is perpendicular to the maximum principal stress direction, only normal traction t_n acts on the crack at the moment of its initiation (**Figure 38a**, **Figure 38b**). The crack type CT2 assumes that the crack is initiated in longitudinal direction regardless maximum principal stress direction if crack normal deviation angle is $\theta_{CT1,max} \leq \theta \leq 90^\circ$ (**Figure 38c**, **Figure 38d**).

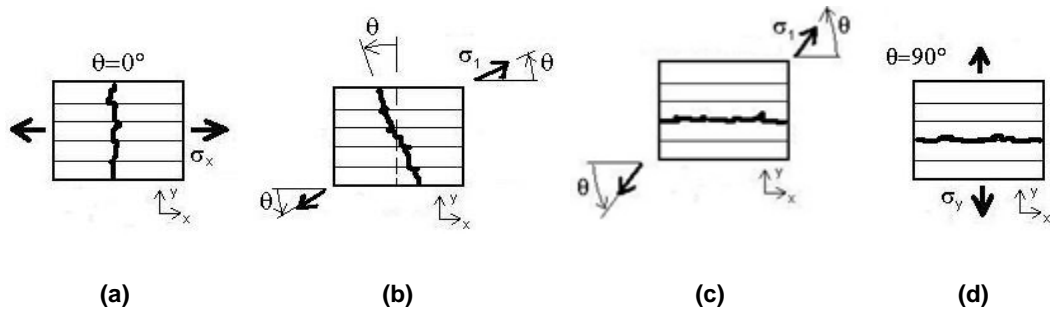


Figure 38 – Crack types according to crack normal deviation angle θ : CT1 under $\theta = 0^\circ$ (a), CT1 under $0^\circ \leq \theta \leq \theta_{CT1,max}$ (b), CT2 under $\theta_{CT1,max} \leq \theta \leq 90^\circ$ (c), CT2 under $\theta = 90^\circ$ (d)

In the developed model, crack type is determined by means of the function of crack type $f_{CT}(\sigma_x, \sigma_y)$ that reads

$$f_{CT} = \tan(2\theta) \cdot \frac{(\sigma_x - \sigma_y)}{2} \quad [26]$$

The function f_{CT} is derived from the standard expression for an angle θ contained by the direction of maximum principal stress (σ_1) and that of longitudinal direction (x) as follows

$$\tan(2\theta) = \frac{\tau_{xy}}{\frac{\sigma_x - \sigma_y}{2}} \quad [27]$$

For a point on the failure surface, the value of $\tau_{xy}(\sigma_x, \sigma_y)$ and the function of crack type $f_{CT}(\sigma_x, \sigma_y)$ are compared (see **Figure 39**). Crack type CT1 is considered if $\tau_{xy} \leq f_{CT}$ and crack type CT2 if $\tau_{xy} > f_{CT}$.

A few examples (A - D) of load conditions and their crack types are introduced in **Table 3**. In this table are presented stress components calculated for prescribed increments of strain in elastic region until reaching the failure surface. These four cases are visualized in **Figure 40** where is highlighted a stress component that initiated the corresponding crack type. Load cases A - D are also visualized on the failure surface in the state of crack initiation in **Figure 41**.

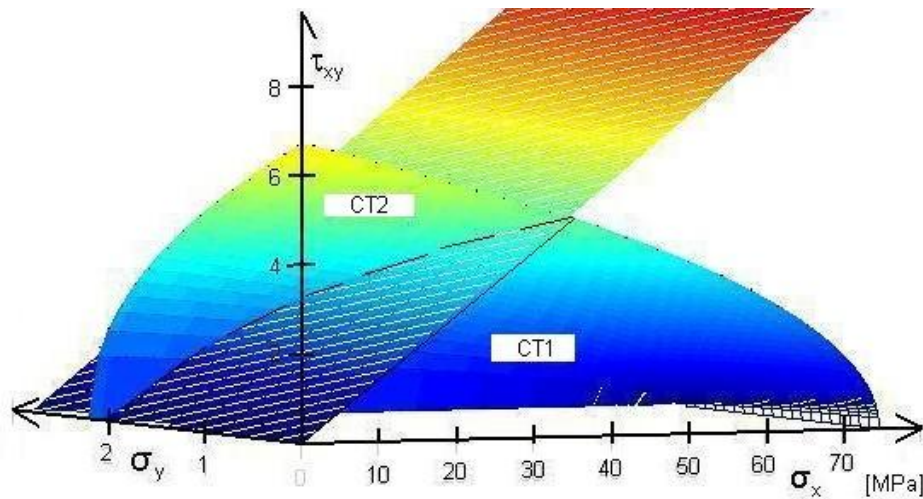


Figure 39 – Failure surface f_{cic} for spruce (*Picea abies*) divided into two parts for crack type CT1 (across the fibers) and CT2 (along the fibers) by the surface of crack type function f_{CT}

Table 3 – Examples of load cases run by strain ϵ , their crack types and crack normal deviation angle θ

Load case	Crack type	Angle θ [°]	ϵ_x [-]	ϵ_y [-]	ϵ_{xy} [-]	σ_x [MPa]	σ_y [MPa]	τ_{xy} [MPa]
A	CT1	0	0.00496	0.00005	0	74.40000	1.86560	0
B	CT2	90	0.00002	0.00072	0	0.53938	2.20000	0
C	CT2	90	0.00005	0.00020	0.00993	0.81002	0.62962	5.61719
D	CT1	4	0.00300	0.00004	0.00505	45.69849	1.17246	2.84399

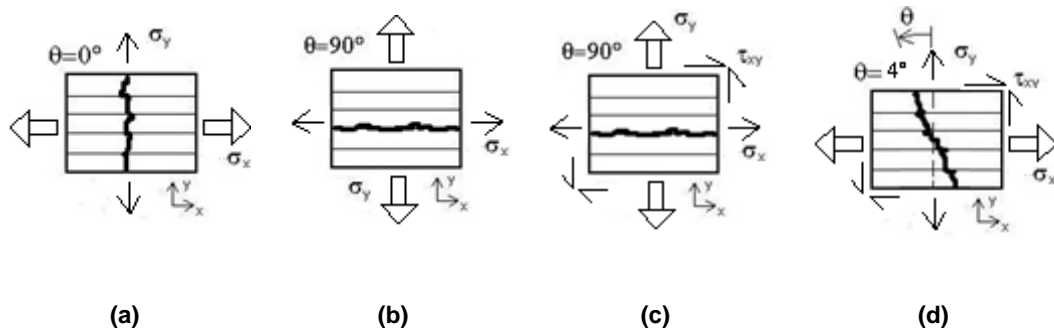


Figure 40 – Crack type and crack normal deviation angles θ for load cases A (CT1, $\theta = 0^\circ$) (a), B (CT2, $\theta = 90^\circ$) (b), C (CT2, $\theta = 90^\circ$) (c), and D (CT1, $\theta = 4^\circ$) (d) where large arrows reflect a dominant stress initiating the corresponding crack type

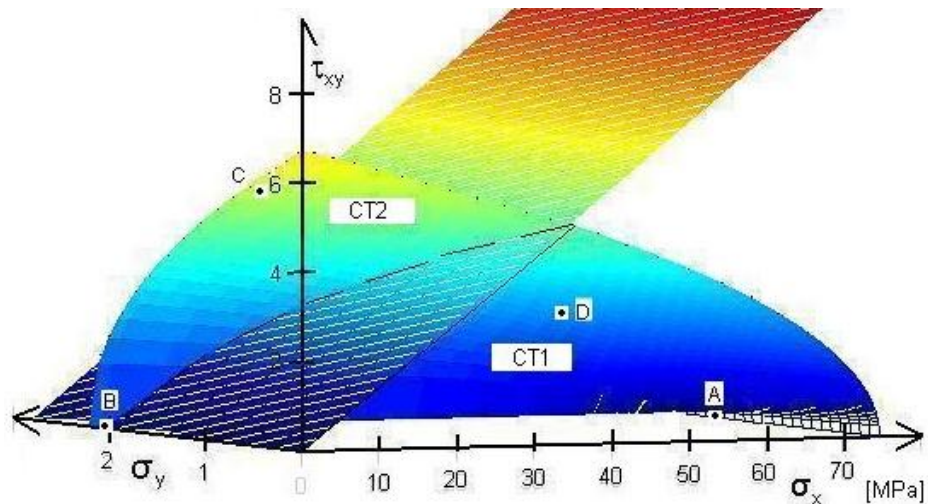


Figure 41 – Visualization of stress components of load cases A, B, C, D at the state of crack initiation in the form of points with coordinates $[\sigma_x, \sigma_y, \tau_{xy}]$ at failure surface

4.5 Smearred crack model (SCM)

By smeared crack model we mean here a particular class of constitutive models developed for quasi-brittle materials under predominantly tensile loading. The basic idea of the model is that the total strain is decomposed into an elastic part and in an inelastic part (cracking strain). The inelastic strain due to crack opening is related directly to the traction transmitted across the crack. (Jirásek, 2012)

Two types of SCM can be distinguished: fixed and rotating crack model. Fixed crack model freezes the crack direction determined at the moment of the crack initiation while rotating crack model assumes that crack normal remains aligned with the current direction of maximal principal strain. In case Rankine criterion is used as an initiation criterion, the crack plane is initially exposed to a non-zero normal traction (of value of tensile strength in the appropriate direction) and zero shear traction. Later, the crack plane remains freezed and principal axes can rotate and shear tractions may arise on the crack. (Jirásek, 2012)

In the following subchapters, basic principles of smeared crack model are described for 1D space. The second and third subchapters provide a general description of 2D fixed smeared crack model and its application to the constitutive model developed in this work, respectively.

4.5.1 One-dimensional smeared crack model

Smeared crack model (SCM) decomposes the total strain (ε) in into two parts: elastic strain ε_e (deformation of the uncracked material) and crack strain ε_c (the contribution of cracking). The one-dimensional (1D) space, strain decomposition is expressed as follows

$$\varepsilon = \varepsilon_e + \varepsilon_c \quad [28]$$

The elastic strain (ε_e) is related to stress (σ) by Hook's law

$$\sigma = E\varepsilon_e \quad [29]$$

where E is modulus of elasticity.

The crack strain represents smeared additional deformation caused by opening of the crack. The additive strain decomposition can be expressed as a rheological model where elastic spring is coupled in series with a unit representing the contribution of the crack (Figure 42). As the coupling is serial, both units transmit the same stress σ .

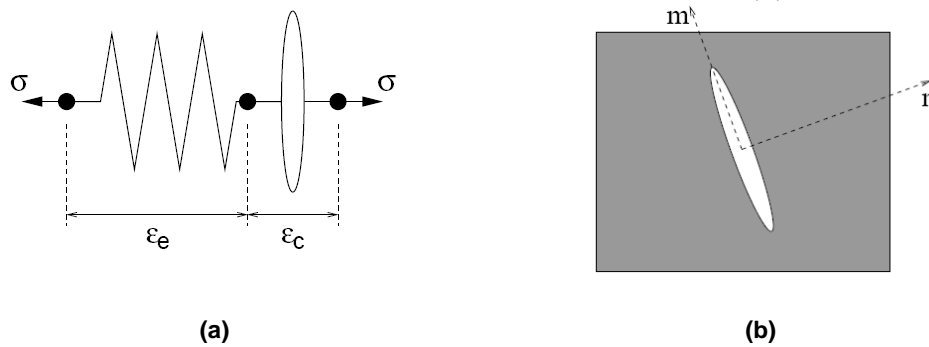


Figure 42 – Smeared crack model: represented as an elastic unit coupled in series to a crack unit (a), local coordinate system aligned with the crack (b) (Jirásek, 2012)

Initially, the material in an uncracked state has linear elastic response. A crack appears when the tensile strength of the material is reached. The loss of cohesion during the crack development is considered as a gradual process. An equivalent cohesive crack which can still transmit stress is introduced. The cohesive stress σ can be expressed as a function of crack strain ε_c (cohesive law) or a function of the crack opening δ (traction-separation law):

$$\sigma = f_c(\varepsilon_c) \quad [30]$$

$$\sigma = f_\delta(\delta) \quad [31]$$

Since the crack strain depends on the gauge length along which the average strain is measured, it is more appropriate to express the cohesive stress σ by means of crack opening δ . Crack opening is defined as the integral of all inelastic deformation across the width of the fracture process zone. Evaluation of stress for a given strain increment (required for numerical simulations) is determined by assuming that the final stress in the elastic spring is equal to the final stress in the cracking unit. This leads to the equation describing the internal equilibrium in the rheological model:

$$\sigma = E(\varepsilon - \varepsilon_c) = f_c(\varepsilon_c) \quad [32]$$

In **Figure 43**, total stress-strain curve obtained by the sum of elastic and crack strain is displayed.

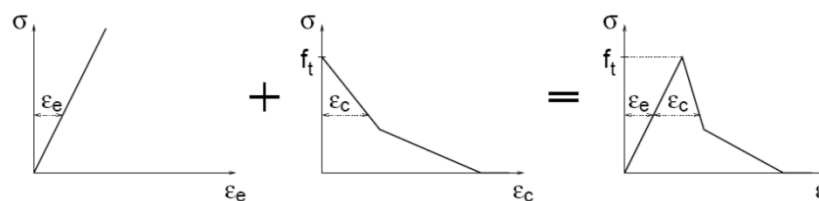


Figure 43 – Total stress-strain curve ($\sigma - \varepsilon$) obtained by summing elastic strain ε_e and crack strain ε_c (Jirásek, 2012)

4.5.2 Two-dimensional fixed smeared crack model

Consistently with the basic assumptions (chapter 4.5), we employ the fixed variant of the smeared crack model. To this end, we introduce a local Cartesian coordinate system n, m (**Figure 42b**): axis n is normal to the crack and m is parallel to it. As previously mentioned, in fixed crack model, the crack direction determined at the moment of the crack initiation remains fixed. The following text is based on Jirásek (2012) and equations are written in tensor notation.

General forms of Eq. [28] and Eq. [29] are written in tensor notation as follows

$$\boldsymbol{\varepsilon} = \boldsymbol{\varepsilon}_e + \boldsymbol{\varepsilon}_c \quad [33]$$

$$\boldsymbol{\sigma} = \mathbf{D}_e : \boldsymbol{\varepsilon}_e \quad [34]$$

where $\boldsymbol{\varepsilon}$ is total strain tensor, $\boldsymbol{\varepsilon}_e$ and $\boldsymbol{\varepsilon}_c$ is elastic and crack strain tensor, respectively, $\boldsymbol{\sigma}$ is stress tensor and \mathbf{D}_e is elastic stiffness tensor.

Crack opening and sliding are affected only by the traction vector \mathbf{t}_c acting on the crack plane defined by a unit normal vector \mathbf{n} :

$$\mathbf{t}_c = \mathbf{n}\boldsymbol{\sigma} \quad [35]$$

Strain components are obtained as follows

$$\mathbf{e}_c = \varepsilon_{nn}^c \mathbf{n} + \gamma_{nm}^c \mathbf{m} \quad [36]$$

$$\boldsymbol{\varepsilon}_c = (\mathbf{n} \otimes \mathbf{e}_c)_{\text{sym}} \quad [37]$$

where \mathbf{e}_c is crack strain vector work-conjugate with \mathbf{t}_c , \mathbf{n} is a unit vector normal to the crack, \mathbf{m} is a unit vector tangential to the crack, ε_{nn}^c is normal crack strain, γ_{nm}^c is shear crack strain, and $\boldsymbol{\varepsilon}_c$ is crack strain tensor that is further described in Jirásek (2012).

Combining equations [33], [34] and [37], stress-strain law is obtained

$$\boldsymbol{\sigma} = \mathbf{D}_e : (\boldsymbol{\varepsilon} - \mathbf{n} \otimes \mathbf{e}_c) \quad [38]$$

where symbol of symmetric part at $\mathbf{n} \otimes \mathbf{e}_c$ can be omitted because of minor symmetry of \mathbf{D}_e . (Jirásek, 2012)

The relation between shear traction and shear crack strain can be expressed by means of a proportionality factor βG , where G is shear modulus of elasticity and $\beta < 1$ is shear retention factor usually decreasing to zero as the crack opening grows.

The cohesive law can be written in the total form

$$\mathbf{t}_c = \mathbf{f}_c(\mathbf{e}_c) \quad [39]$$

or the incremental form

$$\dot{\mathbf{t}}_c = \mathbf{D}_c(\dot{\mathbf{e}}_c) \quad [40]$$

where $\mathbf{D}_c = \partial \mathbf{f}_c / \partial \mathbf{e}_c$ is second-order tangent crack stiffness tensor.

The traction vector must be equal to the projection of the stress tensor which can be computed from the elastic strain. Combining equations [35] and [38] is obtained

$$\mathbf{t}_c = \mathbf{n} \cdot \mathbf{D}_e : \boldsymbol{\varepsilon} - \mathbf{n} \cdot \mathbf{D}_e : (\mathbf{n} \otimes \mathbf{e}_c) = \mathbf{n} \cdot \mathbf{D}_e : \boldsymbol{\varepsilon} - \mathbf{Q}_e \cdot \mathbf{e}_c \quad [41]$$

where $\mathbf{Q}_e = \mathbf{n} \mathbf{D}_e \mathbf{n}$ is called acoustic tensor and an auxiliary function \mathbf{s} can be defined as $\mathbf{s} = \mathbf{n} \cdot \mathbf{D}_e : \boldsymbol{\varepsilon}$. Combining equations [39] and [41], internal equilibrium between tractions in the elastic unit and the crack unit is obtained

$$\mathbf{n} \cdot \mathbf{D}_e : \boldsymbol{\varepsilon} - \mathbf{Q}_e \cdot \mathbf{e}_c = \mathbf{f}_c(\mathbf{e}_c) \quad [42]$$

In case this equation for a given strain increment is non-linear, an iterative computational method is used to solve \mathbf{e}_c , e.g. Newton-Raphson's method (chapter 4.12). (Jirásek, 2012)

In order to derive the tangent material stiffness tensor (relation between stress and strain rate), internal equilibrium equation [42] is expressed in the rate form and crack strain rate is derived

$$\mathbf{n} \cdot \mathbf{D}_e : \dot{\boldsymbol{\varepsilon}} - \mathbf{Q}_e \cdot \dot{\mathbf{e}}_c = \mathbf{D}_c(\dot{\mathbf{e}}_c) \quad [43]$$

$$\dot{\mathbf{e}}_c = (\mathbf{Q}_e + \mathbf{D}_c)^{-1} \cdot \mathbf{n} \cdot \mathbf{D}_e : \dot{\boldsymbol{\varepsilon}} \quad [44]$$

The rate form of stress-strain law is given by substitution of [44] into [38]

$$\dot{\boldsymbol{\sigma}} = \mathbf{D}_e : (\dot{\boldsymbol{\varepsilon}} - \mathbf{n} \otimes \dot{\mathbf{e}}_c) = \mathbf{D}_e : \dot{\boldsymbol{\varepsilon}} - \mathbf{D}_e : [\mathbf{n} \otimes (\mathbf{Q}_e + \mathbf{D}_c)^{-1}] \cdot (\mathbf{n} \cdot \mathbf{D}_e) : \dot{\boldsymbol{\varepsilon}} = \mathbf{D}_{ec} : \dot{\boldsymbol{\varepsilon}} \quad [45]$$

The tangent stiffness tensor of the elastic-cracking material \mathbf{D}_{ec} is then given by

$$\mathbf{D}_{ec} = \mathbf{D}_e - (\mathbf{D}_e \cdot \mathbf{n}) \cdot (\mathbf{Q}_e + \mathbf{D}_c)^{-1} \cdot (\mathbf{n} \cdot \mathbf{D}_e) \quad [46]$$

4.5.3 Application of two-dimensional fixed smeared crack model

The constitutive model developed in this work was based on fixed smeared crack model where only one crack appears. The model was calculated in two-dimensional (2D) space where Voigt's notation (also called matrix notation) was used. Basic variables of 2D fixed smeared crack model used in the developed model are presented in Table 4. Components of an appropriate vector are

considered in the local coordinates of the crack n (normal to the crack) and m (tangential to the crack) (**Figure 42b**).

Table 4 – Basic variables of 2D smeared crack model: t_n – normal traction, t_m – shear traction, δ_n – crack opening in n direction to the crack, δ_m – crack opening in m direction to the crack, ε_{nn}^c – normal crack strain in n direction, ε_{mm}^c – normal crack strain in m direction, γ_{nm}^c – shear crack strain

Traction vector t_c	Crack opening vector δ	Crack strain vector e_c	Crack strain tensor in Voigt's notation ε_c
$t_c = \begin{pmatrix} t_n \\ t_m \end{pmatrix}$	$\delta = \begin{pmatrix} \delta_n \\ \delta_m \end{pmatrix}$	$e_c = \begin{pmatrix} \varepsilon_{nn}^c \\ \gamma_{nm}^c \end{pmatrix}$	$\varepsilon_c = \begin{pmatrix} \varepsilon_{nn}^c \\ \varepsilon_{mm}^c \\ \gamma_{nm}^c \end{pmatrix} = \begin{pmatrix} \varepsilon_{nn}^c \\ 0 \\ \gamma_{nm}^c \end{pmatrix}$

The application of Voigt's notation causes a formal change in previously defined equations. Consideration of orthotropic material calls for consistent distinction between local and global coordinates. For these reasons we present the most important equations for fixed crack model ([33]-[46]) in matrix notation as they were applied in the developed model.

A transformation of crack strain vector e_c to crack strain tensor in Voigt's notation ε_c is calculated in local coordinates (denoted by superscript L) as follows

$$\varepsilon_c^L = N \cdot e_c^L \quad [47]$$

where N is a transformation matrix defined by

$$N = \begin{pmatrix} 1 & 0 \\ 0 & 0 \\ 0 & 1 \end{pmatrix} \quad [48]$$

The equation of internal equilibrium between tractions in the elastic unit and the crack unit (Eq. [42]) in local coordinates is obtained

$$N \cdot D_e^L \cdot \varepsilon^L - Q_e^L \cdot e_c^L = f_c(e_c^L) \quad [49]$$

where D_e^L is elastic stiffness matrix in local coordinates, $Q_e^L = N \cdot D_e^L \cdot N^T$ is acoustic matrix in local coordinates, $f_c(e_c^L)$ is a vector of functions of cohesive law in n and m direction, and an auxiliary function s is defined as $s = N \cdot D_e^L \cdot \varepsilon^L$. In case this equation for a given strain increment is non-linear, an iterative computational method ought to be used to solve the equation for crack strain vector e_c^L (e.g. Newton-Raphson).

Eq. [44] of crack strain rate is in Voigt's notation computed

$$\dot{e}_c^L = (Q_e^L + D_c^L)^{-1} \cdot N \cdot D_e^L \cdot \dot{\varepsilon}^L \quad [50]$$

where \dot{e}_c^L is an increment of crack strain vector in local coordinates, $\dot{\varepsilon}^L$ is an increment of crack strain tensor in Voigt's notation in local coordinates, and $D_c^L = \partial f_c / \partial e_c^L$ is tangent crack stiffness matrix.

Similarly to Eq. [45], the rate form of stress-strain law is expressed in local coordinates

$$\dot{\sigma}^L = D_e^L \cdot (\dot{\varepsilon}^L - \dot{\varepsilon}_c^L) = D_e^L \cdot \dot{\varepsilon}^L - D_e^L \cdot N(Q_e^L + D_c^L)^{-1} \cdot N \cdot D_e^L \cdot \dot{\varepsilon}^L = D_{ec}^L \cdot \dot{\varepsilon}^L \quad [51]$$

Accordingly to Eq. [46], the tangent stiffness matrix of the elastic-cracking material in local coordinates D_{ec}^L is given by

$$D_{ec}^L = D_e^L - D_e^L \cdot N(Q_e^L + D_c^L)^{-1} \cdot N \cdot D_e^L \quad [52]$$

Transformation between local and global coordinate systems is further treated in chapter 4.11. Full version of the code of the model developed in this work is available in Appendix 2.

4.6 Cohesive law in n direction

The cohesive law (softening curve) in the direction normal to the fixed crack can be expressed by different functions (according to the experimental data). In **Figure 44**, a comparison of various

softening laws for a material with given strength $f_t = 3.5$ MPa and fracture energy $G_F = 140$ J/m² is presented. The deviations of exponential, bilinear and Reinhardt-Hordijk's (Reinhardt et al., 1986) curves are relatively small while the linear softening curve substantially differs from the non-linear ones. (Jirásek, 2012)

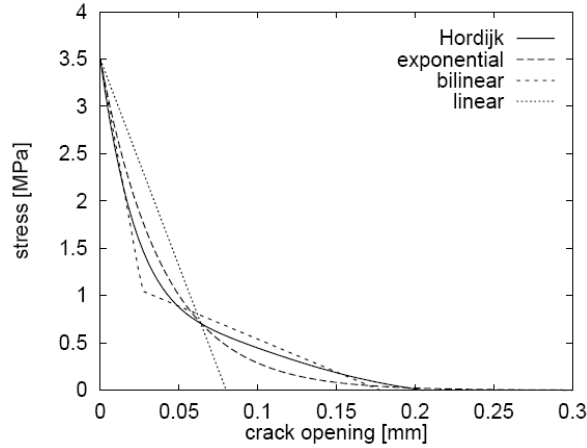


Figure 44 – Comparison of various softening laws in for a given strength $f_t = 3.5$ MPa and fracture energy $G_F = 140$ J/m² (Jirásek, 2012)

For the developed model, the component t_n (cohesive law in n direction) of the traction vector \mathbf{t}_c is calculated on the basis of Reinhardt-Hordijk traction-separation law proposed by Reinhardt et al. (1986) as it is qualitatively consistent with experimentally observed softening of wood (e.g. spruce) in Reiterer et al. (2002) (**Figure 22**)

$$t_n(\varepsilon_{nn}^c) = \begin{cases} t_{n,ci} \left(\left[1 + \left(\frac{c_1 \delta_n}{\delta_{crit}} \right)^3 \right] \exp \left(\frac{c_2 \delta_n}{\delta_{crit}} \right) - e^{-c_2} (1 + c_1^3) \frac{\delta_n}{\delta_{crit}} \right) & \text{if } \delta_n \in [0; \delta_{crit}) \\ 0 & \text{if } \delta_n \geq \delta_{crit} \end{cases} \quad [53]$$

where $t_{n,ci}$ is the normal traction at the state of crack initiation which existed at the crack plane [MPa], $\delta_n = l_{ch} \varepsilon_{nn}^c$ is crack opening normal to the crack direction [mm], l_{ch} is equivalent length expressing the size of an element [mm] where the crack is smeared, δ_{crit} is critical crack opening in n (and also for the proposed model in m) direction [mm]. Material parameters c_1 and c_2 are dimensionless. They control the shape of the softening curve and their default values recommended by Hordijk (1991) are $c_1 = 3$ and $c_2 = 6.93$. The softening t_n function according to Reinhardt et al. (1986) expressed as a cohesive law is displayed in **Figure 45**.

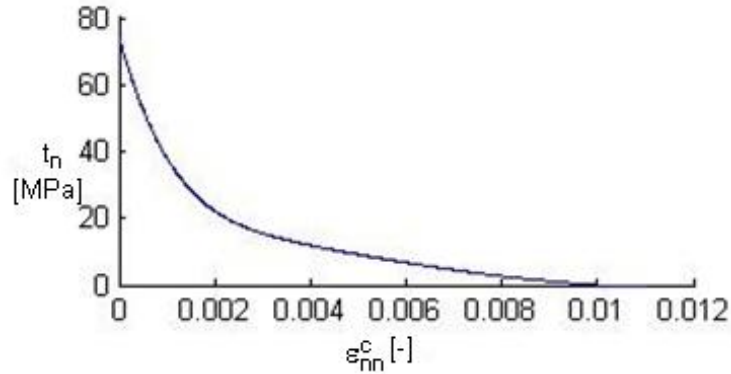


Figure 45 – Reinhardt–Hordijk cohesive law in n direction $t_n(\varepsilon_{nn}^c)$ for $\delta_{crit} = 0.1$ mm, $\sigma_{nn} = 74.4$ MPa, $c_1 = 3$ and $c_2 = 6.93$ and $l_{ch} = 10$ mm

4.7 Cohesive law in m direction

The component shear traction t_m of traction vector t_c is proposed to be calculated according to linear-based function or arctangential function. The latter function is used because, as opposed to the former one, it allows us to limit the maximum shear traction that can develop on the crack.

For the crack type CT1, the value of shear traction t_m is always zero ($t_m = 0$) at crack initiation as the crack is always perpendicular to the principal stress direction when it is initiated. On the contrary, for the crack type CT2, the value of t_m can be $t_m \in [0, f_s)$, limited by shear strength f_s , at crack initiation as the crack is always parallel with wood fibers and does not have to be perpendicular to the principal stress.

4.7.1 Linear-based function t_m

If shear traction t_m is taken proportional to local total shear strain γ_{nm} with a proportionality factor βG , the linear-based function can be derived in local coordinates in 2D as follows

$$t_m = \beta G \gamma_{nm} \quad [54]$$

$$t_m = G \gamma_{nm}^c \quad [55]$$

$$\gamma_{nm} = \gamma_{nm}^e + \gamma_{nm}^c \quad [56]$$

$$t_m = \beta G (\gamma_{nm}^e + \gamma_{nm}^c) = \beta t_m + \beta G \gamma_{nm}^c \quad [57]$$

$$t_m (1 - \beta) = \beta G \gamma_{nm}^c \quad [58]$$

$$t_m = \frac{\beta}{1 - \beta} G \gamma_{nm}^c \quad [59]$$

where γ_{nm}^e is elastic part of total shear strain and $\beta(\varepsilon_{nn}^c)$ is a function of shear retention factor that depends on normal crack strain in n direction ε_{nn}^c .

The linear-based function t_m can be finally calculated according to the following equation:

$$t_m(\varepsilon_{nn}^c, \gamma_{nm}^c) = \frac{\beta(\varepsilon_{nn}^c)}{1 - \beta(\varepsilon_{nn}^c)} G \gamma_{nm}^c \quad [60]$$

Due to lack of available experimental evidence on shear behavior of cracks in wood, we assume that the shear retention factor beta linearly decreases with increasing crack opening displacement, i.e. it can be expressed as:

$$\beta(\varepsilon_{nn}^c) = \begin{cases} 1 - \frac{\delta_n}{\delta_{crit}} & \text{if } \delta_n \in [0; \delta_{crit}) \\ 0 & \text{if } \delta_n \geq \delta_{crit} \end{cases} \quad [61]$$

where $\delta_n = l_{ch} \varepsilon_{nn}^c$ is crack opening normal to the crack direction [mm], δ_{crit} is critical crack opening in n direction [mm] which is further described in chapter 4.8. Both functions $t_m(\varepsilon_{nn}^c, \gamma_{nm}^c)$ and $\beta(\varepsilon_{nn}^c)$ are displayed in **Figure 46**.

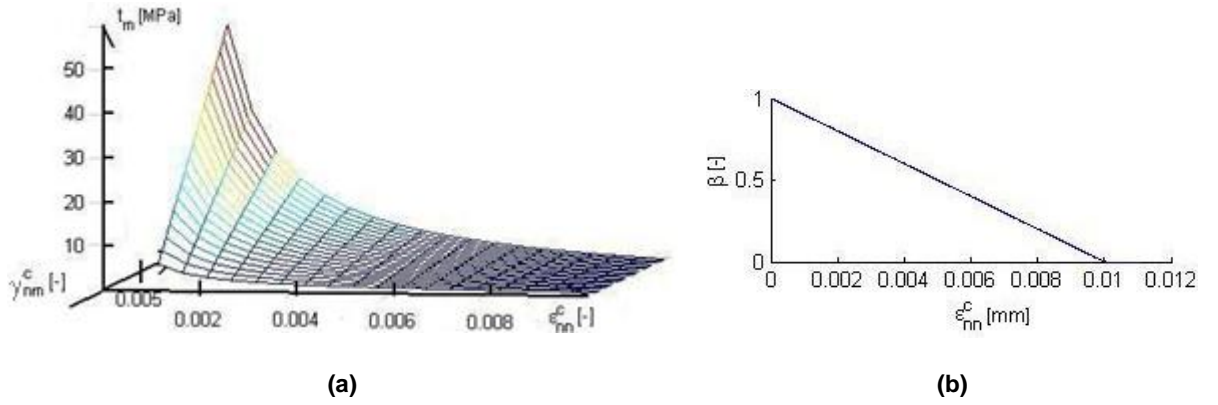


Figure 46 – Display of the cohesive law in m direction (linear-based function) $t_m(\varepsilon_{nn}^c, \gamma_{nm}^c)$ (a) and function of shear retention factor $\beta(\varepsilon_{nn}^c)$ (b) for $\delta_{crit} = 0.1$ mm and $l_{ch} = 10$ mm

The linear-based function $t_m(\varepsilon_{nn}^c, \gamma_{nm}^c)$ is not defined at $\varepsilon_{nn}^c = 0$. If crack strain is approaching zero ($\varepsilon_{nn}^c \rightarrow 0, \gamma_{nm}^c \rightarrow 0$), the function $t_m(\varepsilon_{nn}^c, \gamma_{nm}^c)$ approaches vertical axis. This implies that if the crack is initiated at $t_m > 0$ (e.g. crack type CT2), the linear-based description of $t_m(\varepsilon_{nn}^c, \gamma_{nm}^c)$ allows a smooth transition from the stress state on the failure surface to the proposed cracking cohesive relationship

For a constant value of γ_{nm}^c , shear traction t_m decreases with increasing ε_{nn}^c . For a constant value of $\varepsilon_{nn}^c \in (0, \delta_{crit} / l_{ch})$, shear traction t_m linearly increases without limits with increasing γ_{nm}^c and thus the function $t_m(\varepsilon_{nn}^c, \gamma_{nm}^c)$ is unbounded.

To conclude, the linear-based function $t_m(\varepsilon_{nn}^c, \gamma_{nm}^c)$ is advantageous to use as it enables a smooth transition from the stress state on the failure surface to the proposed cracking cohesive relationship. On the other hand, its weakness consists in the fact, that it is unbounded ($t_m(\varepsilon_{nn}^c, \gamma_{nm}^c) \rightarrow \infty$) and thus shear traction t_m can exceed shear strength f_s , which is unrealistic.

4.7.2 Arctangential function of t_m

In order to describe cohesive law by a more appropriate function than by the linear-based one (chapter 4.7.1), an arctangential function is proposed. The arctangential function enables that shear traction t_m is limited by shear strength f_s and takes the value of $t_m \in [0, f_s)$ at crack initiation state.

Shear traction t_m is expressed using arctangential function as follows

$$t_m(\varepsilon_{nn}^c, \gamma_{nm}^c) = f_s \frac{\pi}{2} \operatorname{atan} \left(\gamma_{nm}^c \frac{\beta(\varepsilon_{nn}^c)}{1 - \beta(\varepsilon_{nn}^c)} \right) \quad [62]$$

where ε_{nn}^c and γ_{nm}^c are components of crack strain vector e_c . The function of shear retention factor $\beta(\varepsilon_{nn}^c)$ is considered as follows

$$\beta(\varepsilon_{nn}^c) = \begin{cases} 1 - \left(\frac{\delta_n}{\delta_{crit}} \right)^p & \text{if } \delta_n \in [0; \delta_{crit}) \\ 0 & \text{if } \delta_n \geq \delta_{crit} \end{cases} \quad [63]$$

where $\delta_n = l_{ch} \varepsilon_{nn}^c$ is crack opening normal to the crack direction [mm], δ_{crit} is critical crack opening in n direction [mm] which is further described in chapter 4.8, and p is a material parameter that determines the slope of the function $\beta(\varepsilon_{nn}^c)$. For an assumed slope, the exponent p is set to $p = 2$.

It should be noted that for negative shear crack strain γ_{nm}^c , the function $t_m(\varepsilon_{nn}^c, \gamma_{nm}^c)$ is considered odd to $t_m(\varepsilon_{nn}^c, \gamma_{nm}^c)$ function for positive γ_{nm}^c . Thus, shear traction t_m is expressed using arctangential function for negative γ_{nm}^c as follows

$$t_m(\varepsilon_{nn}^c, \gamma_{nm}^c) = -f_s \frac{\pi}{2} \operatorname{atan} \left(-\gamma_{nm}^c \frac{\beta(\varepsilon_{nn}^c)}{1 - \beta(\varepsilon_{nn}^c)} \right) \quad [64]$$

where the function of shear retention factor $\beta(\varepsilon_{nn}^c)$ is calculated according to Eq. [63].

Function $t_m(\varepsilon_{nn}^c, \gamma_{nm}^c)$ for positive and negative γ_{nm}^c is displayed in **Figure 47**. The function $\beta(\varepsilon_{nn}^c)$ is displayed in **Figure 48**.

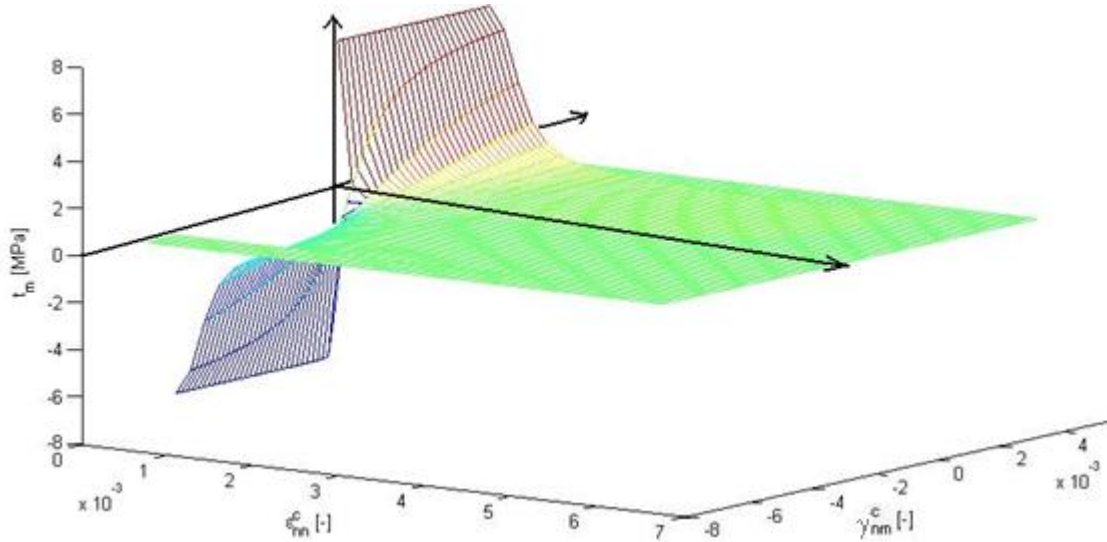


Figure 47 – Display of the arctangential function of cohesive law in m direction $t_m(\varepsilon_{nn}^c, \gamma_{nm}^c)$ for positive and negative γ_{nm}^c where $\delta_{\text{crit}} = 0.15 \text{ mm}$ and $l_{\text{ch}} = 30 \text{ mm}$

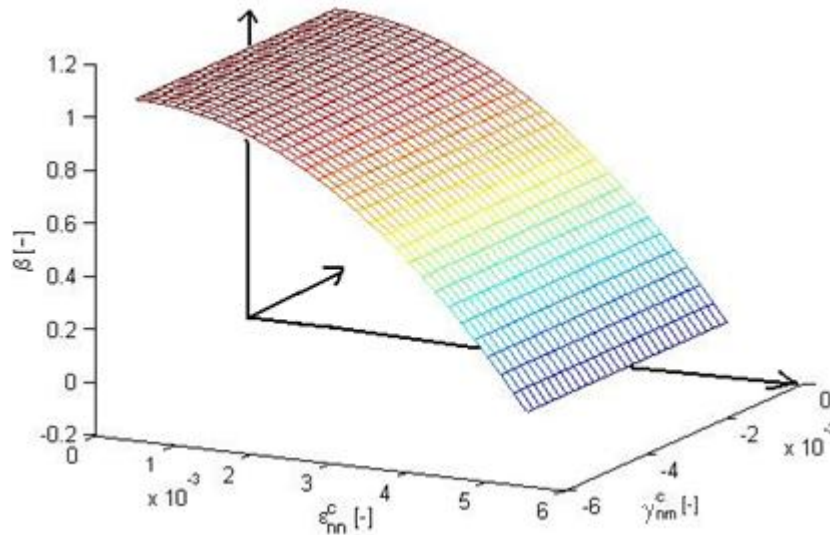


Figure 48 – Display of the function of shear retention factor $\beta(\varepsilon_{nn}^c)$ for arctangential function of cohesive law in m direction $t_m(\varepsilon_{nn}^c, \gamma_{nm}^c)$ where $\delta_{\text{crit}} = 0.15 \text{ mm}$ and $l_{\text{ch}} = 30 \text{ mm}$

The arctangential function $t_m(\varepsilon_{nn}^c, \gamma_{nm}^c)$ behaves in an analogous way with the linear-based function (chapter 4.7.1) as the arctangential function $t_m(\varepsilon_{nn}^c, \gamma_{nm}^c)$ allows a smooth transition from the stress state on the failure surface to the proposed cracking cohesive relationship and it is not defined at $\varepsilon_{nn}^c = 0$.

Difference between these functions consists in the fact that the arctangential function $t_m(\varepsilon_{nn}^c, \gamma_{nm}^c)$ is limited by shear strength and thus shear traction takes the value of $t_m \in [0, f_s)$. Unlike the linear-

based function, for a constant value of $\varepsilon_{nn}^c \in (0, \delta_{crit} / l_{ch})$, shear traction t_m increases with increasing γ_{nm}^c in a non-linear way.

If the crack is initiated under pure shear, the value of shear strength f_s is approached at the beginning of inelastic calculation ($t_m \rightarrow f_s$). If the pure shear loading goes on, the shear traction t_m keeps approaching f_s ($t_m \rightarrow f_s$) and the behavior is plastic.

The arctangential function $t_m(\varepsilon_{nn}^c, \gamma_{nm}^c)$ counts with non-linear elastic behavior of the material after crack is initiated which describes behavior of bridging fibers that tie the two crack faces together. This assumption of bridging fibers is more suitable for crack type CT1 than CT2.

To conclude, the arctangential function $t_m(\varepsilon_{nn}^c, \gamma_{nm}^c)$ is advantageous to use as it not only enables a smooth transition from the stress state on the failure surface to the proposed cracking cohesive relationship, but also it is limited by shear strength f_s .

4.8 Critical crack opening δ_{crit}

In the proposed model, critical crack opening δ_{crit} is a parameter that determines a complete separation of crack surfaces both in n and m direction.

Here, critical crack opening δ_{crit} is calculated for the normalized Reinhardt–Hordijk softening curve (Reinhardt et al., 1986). The area under the normalized Reinhardt–Hordijk curve is for default parameters 0.1947. The fracture energy G_F can be evaluated as

$$G_F = 0.1947 f_t \delta_{crit} \quad [65]$$

where f_t is tensile strength.

When a material is described by tensile strength f_t and fracture energy G_F , the critical crack opening δ_{crit} can be evaluated as

$$\delta_{crit} = \frac{5.136 G_F}{f_t} \quad [66]$$

4.9 Crack unloading/reloading cycle

This subchapter describes basic principles of unloading/reloading and their implementation in the 2D constitutive model developed in this work.

To consider unloading/reloading cycles in the calculation, a history variable K is introduced as a sum of positive increments of crack strain $\Delta\varepsilon_c$ (maximum previously reached ε_c). Linear unloading/reloading is the simplest approach. Three basic types of unloading are presented in **Figure 49**.

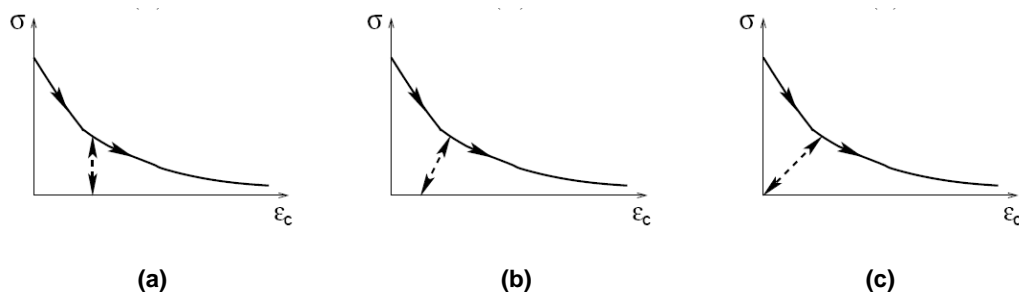


Figure 49 – Basic types of unloading/reloading cycles: permanent crack strain ε_c (a), partial reduction of ε_c due to crack closure (the most realistic case) (b), complete reduction of ε_c due to crack closure (c) (Jirásek, 2012)

In the constitutive model developed in this work, the crack unloading/reloading is intended for one cycle and it needs to be tested in more details for further use.

The implementation of unloading into the developed model is depicted in the following text:

- A new internal variable K is introduced. This variable expresses a sum of all positive increments of crack strain vector $\Delta\varepsilon_{nn}^c$ that are not part of unloading/reloading cycle (see **Figure 50a**).
- In the first step of unloading, the calculated value of $\Delta\varepsilon_{nn}^c$ is rectified by means of a new calculation of $\Delta\varepsilon_{nn}^c$ where is used a function $t_{n,UNL}(\varepsilon_{nn}^c)$ instead of cohesive law function $t_n(\varepsilon_{nn}^c)$. The function $t_m(\varepsilon_{nn}^c, \gamma_{nm}^c)$ is considered the same both for loading and unloading.
- The function $t_{n,UNL}(\varepsilon_{nn}^c)$ is based on simplified assumption of complete reduction of $\Delta\varepsilon_{nn}^c$ due to crack closure (**Figure 49c**). This function includes a constant value of the starting point (S) of unloading expressed by an actual value of normal traction at point S ($t_{n,S}$) and the value of internal variable K at point S (K_S) (**Figure 50b**) as follows

$$t_{n,UNL}(\varepsilon_{nn}^c) = \frac{t_{n,S}}{K_S} \varepsilon_{nn}^c \quad [67]$$

- The next steps of unloading are calculated directly on the basis of $f_{c,UNL}(\mathbf{e}_c) = [t_{n,UNL}(\varepsilon_{nn}^c); t_m(\varepsilon_{nn}^c, \gamma_{nm}^c)]^T$ until the last step of unloading/reloading cycle is finished. Then, the calculation is again the same as before the unloading/reloading cycle until the next negative increment of normal crack strain ε_{nn}^c is calculated.

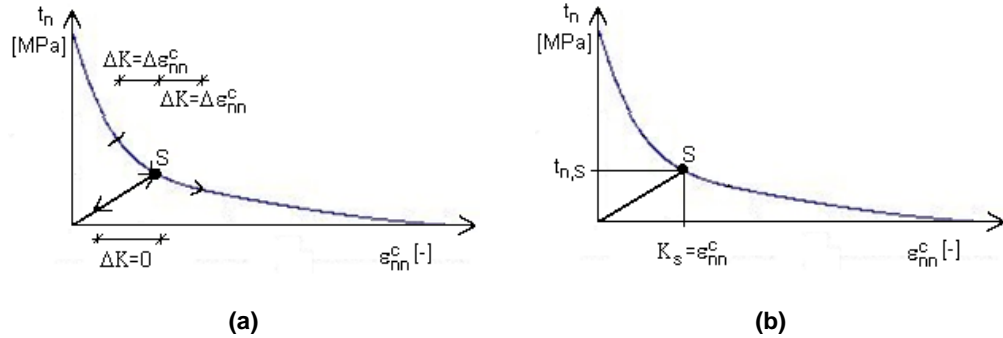


Figure 50 – Unloading/reloading function $t_{n,UNL}(\varepsilon_{nn}^c)$: Internal variable K as a sum of all positive increments $\Delta\varepsilon_{nn}^c$ (a), input values of $t_{n,UNL}(\varepsilon_{nn}^c)$ at point S (b)

4.10 Characteristic length l_{ch}

In smeared crack model, characteristic length l_{ch} [mm] is a size of an element across which a fictitious crack is smeared. The parameter of l_{ch} relates crack opening (δ_n, δ_m) [mm] and crack strain components ($\varepsilon_{nn}^c, \gamma_{nm}^c$) [-], respectively, as follows

$$\delta_n = l_{ch} \varepsilon_{nn}^c \quad [68]$$

$$\delta_m = l_{ch} \gamma_{nm}^c \quad [69]$$

In finite element calculations, the value of l_{ch} is often related to the area of a finite element. (Feenstra, 1993).

Generally, characteristic length l_{ch} is not a material property (length) that can be measured. It is derived from three different material properties and therefore it can be regarded as a material property. The characteristic length is defined as

$$l_{ch} = \frac{EG_F}{f_t^2} \quad [70]$$

where E is modulus of elasticity in the respective direction [MPa], G_F is fracture energy [N/mm] and f_t is tensile strength [MPa].

If the value of characteristic length l_{ch} is higher than a limit value $l_{ch,lim}$, snap-back occurs in the calculation. An effect of snap-back is shown in **Figure 51** for load – displacement curve. When elastic region of the curve is abandoned, snap-back occurs with negative increments of displacement and load at the same time.

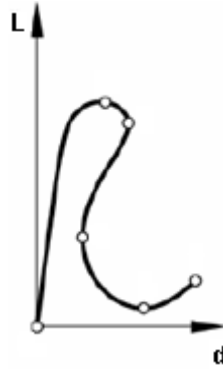


Figure 51 – Non-linear response: snap-back in load (L) – displacement (d) curve

To avoid snap-back e.g. in a stress-strain relation, the derivative of the stress-strain curve after the maximum stress is reached must be negative. The influence of characteristic length l_{ch} on stress-strain curve is shown in **Figure 52**. It can be observed that the higher is the value of l_{ch} , the closer is the softening part of the curve to snap-back.

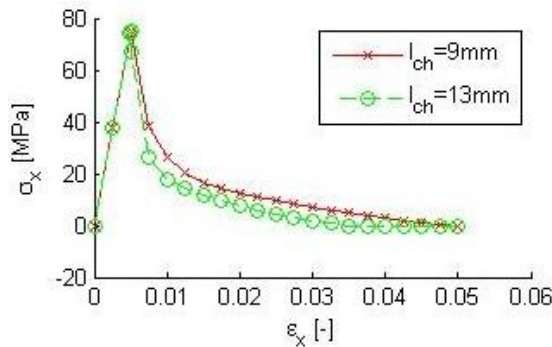


Figure 52 – Stress-strain curve $\sigma_x - \varepsilon_x$ calculated by the proposed model for 1D inputs $\Delta\varepsilon_x = 2.5 \cdot 10^{-3}$, $\nu_{xy} = 0$, $l_{ch} = 9 \text{ mm}$, $l_{ch} = 13 \text{ mm}$

4.11 Transformation between coordinate systems

In the model developed in this work, for transformation between local (n, m) and global (x, y) coordinates was used rotation matrix R . This rotation matrix for counterclockwise transformation by an angle α of strain and stress second order tensor in 2D ($R_{\varepsilon, \sigma}$) is defined as follows

$$R_{\varepsilon, \sigma} = \begin{pmatrix} \cos \alpha & -\sin \alpha \\ \sin \alpha & \cos \alpha \end{pmatrix} \quad [71]$$

The transformation of stress or strain second order tensor from global (G) to local (L) coordinates counterclockwise can be calculated as follows

$$\boldsymbol{\varepsilon}_L = \mathbf{R}_{\varepsilon,\sigma} \boldsymbol{\varepsilon}_G (\mathbf{R}_{\varepsilon,\sigma})^T \quad [72]$$

$$\boldsymbol{\sigma}_L = \mathbf{R}_{\varepsilon,\sigma} \boldsymbol{\sigma}_G (\mathbf{R}_{\varepsilon,\sigma})^T \quad [73]$$

The transformation of stress or strain second order tensor from local (L) to global (G) coordinates clockwise can be calculated as follows

$$\boldsymbol{\varepsilon}_G = (\mathbf{R}_{\varepsilon,\sigma})^{-1} \boldsymbol{\varepsilon}_L ((\mathbf{R}_{\varepsilon,\sigma})^T)^{-1} \quad [74]$$

$$\boldsymbol{\sigma}_G = (\mathbf{R}_{\varepsilon,\sigma})^{-1} \boldsymbol{\sigma}_L ((\mathbf{R}_{\varepsilon,\sigma})^T)^{-1} \quad [75]$$

Rotation matrix for counterclockwise transformation by an angle α of a stiffness matrix (Voigt's notation of fourth order stiffness tensor) in 2D (\mathbf{R}_D) is defined as follows

$$\mathbf{R}_D = \begin{pmatrix} (\cos \alpha)^2 & (\sin \alpha)^2 & -\sin \alpha \cos \alpha \\ (\sin \alpha)^2 & (\cos \alpha)^2 & \sin \alpha \cos \alpha \\ 2 \cos \alpha \sin \alpha & 2(-\sin \alpha) \cos \alpha & (\cos \alpha)^2 - (\sin \alpha)^2 \end{pmatrix} \quad [76]$$

The transformation of stiffness matrix \mathbf{D} from global (G) to local (L) coordinates counterclockwise and then back from local (L) to global (G) coordinates clockwise can be calculated as follows

$$\mathbf{D}_L = (\mathbf{R}_D)^T \mathbf{D}_G \mathbf{R}_D \quad [77]$$

$$\mathbf{D}_G = ((\mathbf{R}_D)^T)^{-1} \mathbf{D}_L (\mathbf{R}_D)^{-1} \quad [78]$$

4.12 Computational Newton-Raphson method

In the proposed constitutive model, Newton-Raphson method is used for solving a set of two non-linear equations (Eq. [49]) used in the calculation of fixed crack model as it is not possible to find a direct solution.

Generally, an iterative procedure to solve a non-linear problem which is rewritten in incremental form is called incremental-iterative (or prediction-correction) procedure. An example of this method is the Newton-Raphson (N-R) method (tangent stiffness method) where the stiffness matrix is updated after each iteration. Basic description of this method is as follows:

- given: $\bar{f}_{\text{ext}}^{(1)}, \bar{f}_{\text{ext}}^{(2)}, \bar{f}_{\text{ext}}^{(3)}, \dots$
- to find: $d^{(1)}, d^{(2)}, d^{(3)}, \dots$
- such that: $(f_{\text{int}}(d^{(n)})) = \bar{f}_{\text{ext}}^{(n)}; n = 1, 2, 3, \dots$

An example of N-R method calculation for a known size of step $(\bar{f}_{\text{ext}}^{(1)} - \bar{f}_{\text{ext}}^{(n-1)})$ and a known non-linear function $(f_{\text{int}}(d^{(n)})) = \bar{f}_{\text{ext}}^{(n)}$ is shown for the first iteration (**Figure 53**) and second iteration (**Figure 54**) within the first step n . The iteration process for a step n is terminated if a chosen condition is fulfilled, e.g. $(\bar{f}_{\text{ext}}^{(n)} - \bar{f}_{\text{int}}^{(n,1)}) < 0.01$.

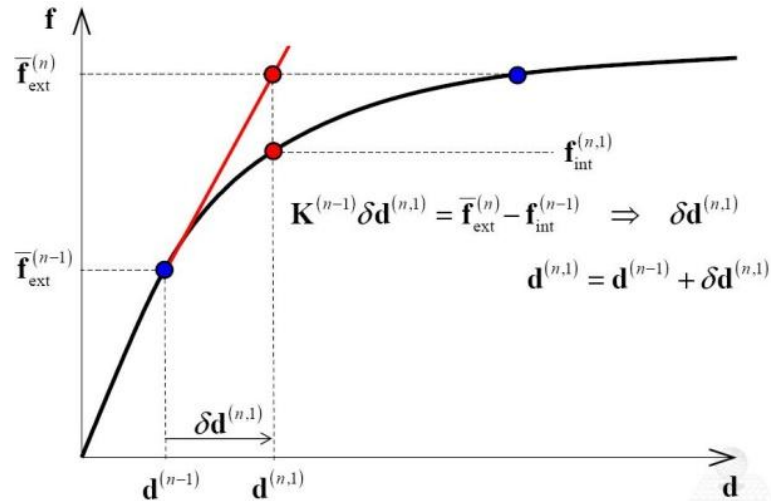


Figure 53 – An example of the first iteration within the first step of N-R method calculation for a known size of step ($\bar{f}_{\text{ext}}^{(n)} - \bar{f}_{\text{ext}}^{(n-1)}$) and a known non-linear function ($f_{\text{int}}(d^{(n)}) = \bar{f}_{\text{ext}}^{(n)}$)

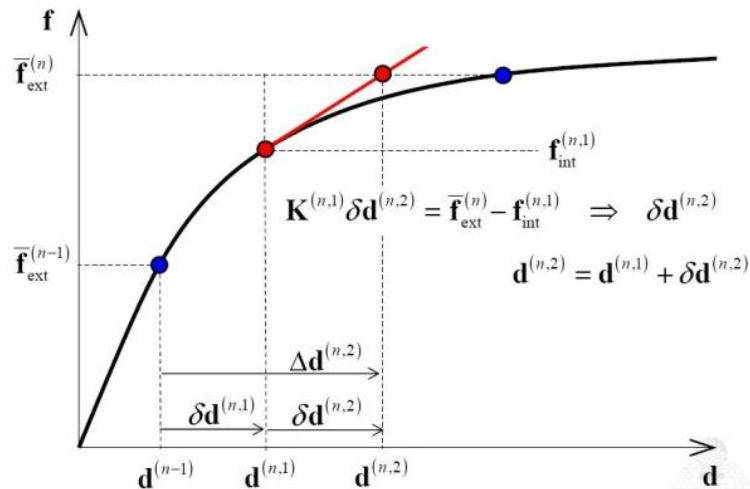


Figure 54 – An example of the second iteration within the first step of N-R method calculation for a known size of step ($\bar{f}_{\text{ext}}^{(n)} - \bar{f}_{\text{ext}}^{(n-1)}$) and a known non-linear function ($f_{\text{int}}(d^{(n)}) = \bar{f}_{\text{ext}}^{(n)}$)

N-R method was used in the developed model for a loop of equations ([50] - [49] - [50] - [49] ...) where was established a new variable s and its increment \dot{s} (in Voigt's notation) for the purpose of iterations as follows:

$$\mathbf{s} = \mathbf{N} \cdot \mathbf{D}_e^L \cdot \boldsymbol{\varepsilon}^L \quad [79]$$

$$\dot{\mathbf{s}} = \mathbf{N} \cdot \mathbf{D}_e^L \cdot \dot{\boldsymbol{\varepsilon}}^L \quad [80]$$

An example of N-R method in the developed model calculation for 2 steps where the first component of \dot{s} vector ($\dot{s}(1)$) and the actual value of the first component of s vector $s(1)$ were known is shown in **Figure 55**. In this Figure, the curve $s(1)$ represents the iterated function $s(e_c(1)) = f_c(e_c(1)) + (Q_e e_c)(1)$, lines $s(1)_{\text{iterN_Step1,2}}$ represent the actual value of the function $s(e_c(1))$ calculated for an iteration of the appropriate step and polylines $s(1)_{\text{Step1,2,3}}$ represent a known increment of the auxiliary function $\dot{s}(1)$ for the respective step. All variables used in this iteration are considered in local coordinates.

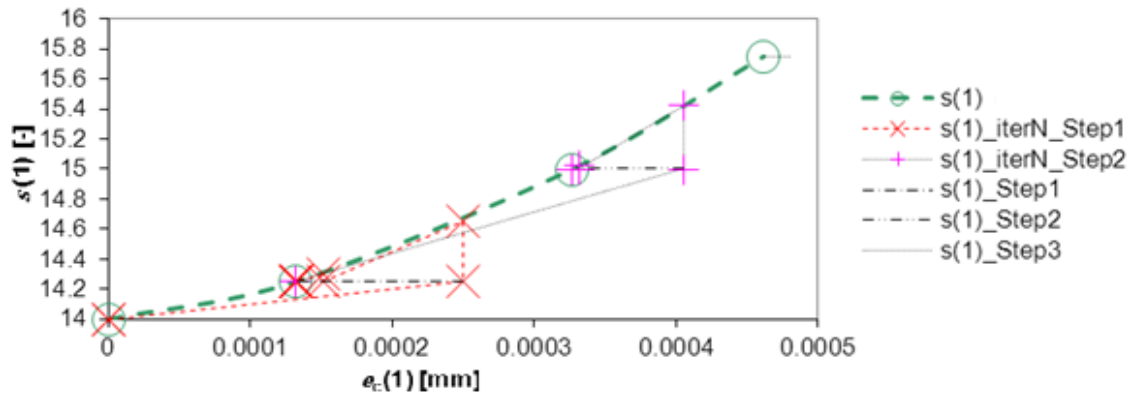


Figure 55 – An example of N-R method calculation for known increments of auxiliary function $\dot{s}(1)$ and a known non-linear function $s(1) = f_c(e_c(1)) + (Q_e e_c)(1)$

4.13 Code scheme

The proposed model calculation consists of two main parts: elastic calculation (EL) and fixed smeared crack calculation (SC). A code scheme of the model is briefly outlined in the following text:

- input data (1): loading path in the form of strain increments ($\Delta\varepsilon$),
- input data for EL (2): definition of elastic orthotropic material parameters (strength f , modulus of elasticity E , Poisson's ratio ν) and assembly of compliance (C_G) and stiffness matrix (D_G) in global coordinates,
- input data for SC (3): critical crack opening (δ_{crit}) and characteristic length (l_{ch}) for crack types CT1 and CT2,
- A. ELASTIC CALCULATION (EL):
 - calculation of peak values of stress (σ_p), strain (ε_p) and strain for the second part of the mixed (EL-SC) step ($\Delta\varepsilon_{1st,sc}$) which is used as strain increment for the first SC step,
 - definition of crack type (CT1, CT2) by means of failure surface (f_{cic}) and the crack type function (f_{CT}),
 - calculation of unit normal vector (\mathbf{n}) and crack normal deviation angle (θ) at the crack initiation state, normal and shear traction in local coordinates ($\sigma_{nn,L}, \sigma_{nm,L}$),
- input data for SC (4): transformation of peak values of stress and strain and stiffness matrix from global to local coordinates,
- input data for SC (5): determination of transformation matrix (N), acoustic matrix (Q_e), tangent crack stiffness matrix (D_c), functions for cohesive law (t_n, t_m), approximation of crack strain vector at crack initiation ($e_{c,0}$),
- B. SMEARED CRACK CALCULATION (SC): cyclic calculation for each loading step $\Delta\varepsilon$:
 - calculation of crack strain increment (Δe_c) by an iterative method,
 - unloading/reloading part of the calculation (chapter 4.9),
 - stress increments ($\Delta\sigma$) and total stress (σ) in local coordinates, tangent stiffness matrix in local coordinates ($D_{ec,L}$),
 - transformation of calculated stress and tangent stiffness matrix into global coordinates,
- output graphs and files.

Full version of the MATLAB code of the developed model is available in Appendix 2.

4.14 Input data

This chapter summarizes input data for developed 2D constitutive model such as elastic material characteristics of several species of hardwoods and softwoods (strength, MoE, Poisson's ratio), threshold angle $\theta_{CT1,max}$, characteristic length l_{ch} , fracture energy G_F and critical crack opening δ_{crit} . Basic average material characteristics of spruce (*Picea abies*) based on Požgaj et al. (1993), chestnut (*Castanea Sativa* Mill.) according to Sousa (2012) and Bartůňková (2010) enhanced by values of deciduous species D70 according to ČSN EN 338 are introduced in Table 5.

Table 5 – Average elastic material characteristics of spruce (*Picea abies*) and oak (*Quercus L.*) according to Požgaj et al. (1993), chestnut (*Castanea sativa* Mill.) according to Sousa (2012) and Bartůňková (2010), deciduous species D70 according to ČSN EN 338 and approximate values (a. v.) of chestnut at $w = 12\%$

Species	Strength [MPa]			MoE in tension [MPa]			Poisson's ratio [-]
	f_{tx}	f_{ty}	f_s	E_x	E_y	G	ν_{xy}
Spruce	74.4	2.2	6.7	14 956	3 088	573	0.023
Chestnut	73.0	-	-	13 048	-	-	-
D70	71.3	1.0	10.2	20 000	1 330	1 250	-
Oak	132.4	5.8	5.8	-	-	-	0.014
Chestnut (a. v.)	73.0	3.4	8.0	13 048	1 330	1 250	0.014

In the proposed model, threshold angle $\theta_{CT1,max}$ defines which crack type was initiated at the crack initiation state. It is set to $\theta_{CT1,max} = 8^\circ$.

Characteristic length l_{ch} is set to $l_{ch} = 10$ mm for CT1 and $l_{ch} = 30$ mm for CT2 for spruce.

The value of critical crack opening of spruce for crack type CT2 $\delta_{crit,CT2}$ was calculated according to the equation [66]. The value of fracture energy G_F was approximated by means of mean value of fracture energy of Eastern Canadian spruce measured on end-tapered double cantilever beam specimens by wedge-splitting test method in Vasic and Smith (2001). The value of tensile strength in normal direction to the crack plane of CT2 is $f_{ty} = 2.2$ MPa. Due to lack of available experimental data, critical crack opening of spruce for CT2 was calculated using a simplified estimation that $\delta_{crit,CT1} = 3\delta_{crit,CT2}$.

In case of chestnut, critical crack opening for CT1 is considered according to tension test results $\delta_{crit,CT1} = 0.18$ mm (Appendix 1) and $\delta_{crit,CT2}$ is calculated as $\delta_{crit,CT2} = 1/3\delta_{crit,CT1}$ and fracture energy is obtained by relation [65], see Table 6.

Table 6 – Critical crack opening for crack type CT1 and CT2 ($\delta_{crit,CT1}$, $\delta_{crit,CT2}$) for spruce and chestnut timber used in the proposed model; values written in bold are based on Vasic and Smith (2001), Bartůňková (2010) and Požgaj et al. (1993) while the others are computed from them

Species	Crack type CT1			Crack type CT2		
	$G_{F,CT1}$ [N/mm]	f_{tx} [N/mm ²]	$\delta_{crit,CT1}$ [mm]	$G_{F,CT2}$ [N/mm]	f_{ty} [N/mm ²]	$\delta_{crit,CT2}$ [mm]
Spruce	6.519	74.4	0.45	0.064	2.2	0.15
Chestnut	2.558	73.0	0.18	0.012	1.0	0.06

5. Results

Results obtained by the developed 2D homogeneous constitutive model are presented in this chapter. The first part of this chapter describes verification of the proposed model by comparison of results obtained from different load cases where isotropic and slightly orthotropic material input data were used. In the second part of this chapter are presented and discussed results of the proposed model for different load cases (LCs) and crack types (crack across fibers CT1, crack along fibers CT2) where orthotropic material of spruce was considered. Last part of this chapter describes model performance during unloading/reloading cycle.

In calculations of fixed crack model were used the following softening functions:

- Reinhardt–Hordijk cohesive law in n direction $t_n(\varepsilon_{nn}^c)$,
- arctangential function of $t_m(\varepsilon_{nn}^c, \gamma_{nm}^c)$,
- input data an orthotropic material of spruce (chapter 4.14).

5.1 Model performance with isotropic material properties

The constitutive model developed in this work was verified by comparing results obtained under different loading paths for isotropic material input data shown in the form of compliance matrix as follows

$$\mathbf{C} = \begin{pmatrix} \frac{1}{E} & \frac{-\nu}{E} & 0 \\ \frac{-\nu}{E} & \frac{1}{E} & 0 \\ 0 & 0 & \frac{1}{G} \end{pmatrix} = \begin{pmatrix} \frac{1}{15000} & \frac{-0.2}{15000} & 0 \\ \frac{-0.2}{15000} & \frac{1}{15000} & 0 \\ 0 & 0 & \frac{1}{6250} \end{pmatrix} \quad [81]$$

where \mathbf{C} is compliance matrix, E is Young modulus of elasticity [MPa] (in both x and y direction), G is shear modulus [MPa] and ν is Poisson's coefficient [-]. These material characteristics were used in load cases V1, V2 and V3 while in V4 was considered minor anisotropy in the form of slightly different values of Young modulus in x and y direction $E_y = 0.9E_x$.

5.1.1 LC V1: $\Delta\varepsilon_x$ and then $\Delta\gamma_{xy}$, CT1, $\theta = 0^\circ$

Load case V1 prescribes increments of strain $\Delta\varepsilon_x^1 = 2 \cdot 10^{-4}$ for step 1 and $\Delta\varepsilon_x^{2-10} = 2 \cdot 10^{-5}$ for steps 2-10 and then $\Delta\gamma_{xy}^{11-20} = 2 \cdot 10^{-4}$ for steps 11-20 while $\Delta\varepsilon_y = 0$ (**Figure 56a**). The results are plotted in **Figure 56 - Figure 61**. **Figure 56b** shows the course of crack opening first in n direction and then in m direction as the load is applied in x and y direction which is in fact n and m direction, respectively. Due to non-zero ν , stress results in y direction (σ_y) is non-zero. Stress-strain curves (**Figure 57**) in non-elastic region (after the peak stress is reached) correspond to the course of iterated normal traction t_n (**Figure 58**) and shear traction t_m (**Figure 59**) based on iterated values of iteration functions $s(1)$ and $s(2)$ (**Figure 60** and **Figure 61**). In **Figure 58 - Figure 61** are marked points of changes A (crack initiation), B (end of uniaxial loading and start of pure shear) and C (end of loading).

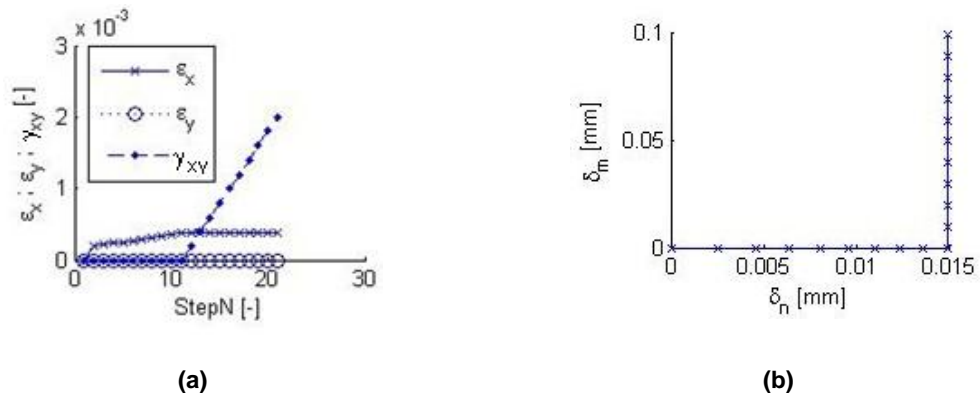


Figure 56 – LC V1: Course of loading run by strain increments $\Delta\varepsilon_x$, $\Delta\varepsilon_y$, $\Delta\gamma_{xy}$ (a), development of crack opening δ_m with respect to δ_n (b)

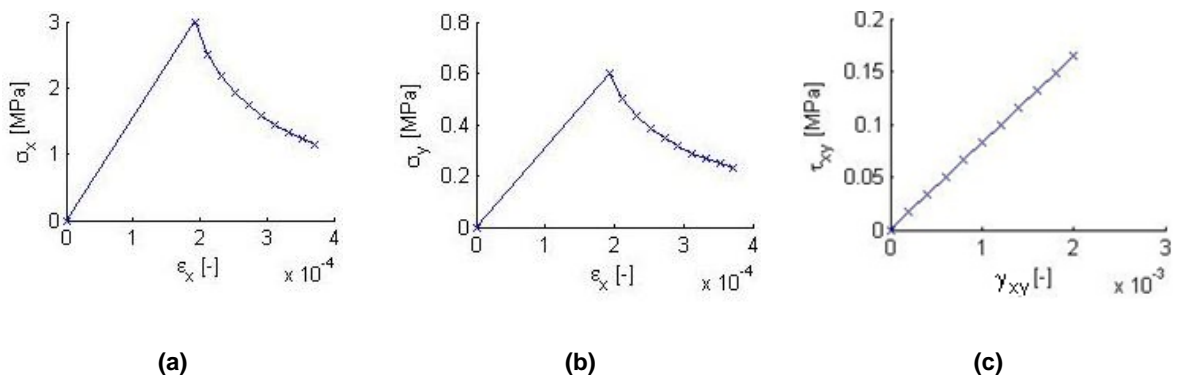


Figure 57 – LC V1: Stress-strain curves $\sigma_x - \varepsilon_x$ (a), $\sigma_y - \varepsilon_x$ (b), $\tau_{xy} - \gamma_{xy}$ (c)

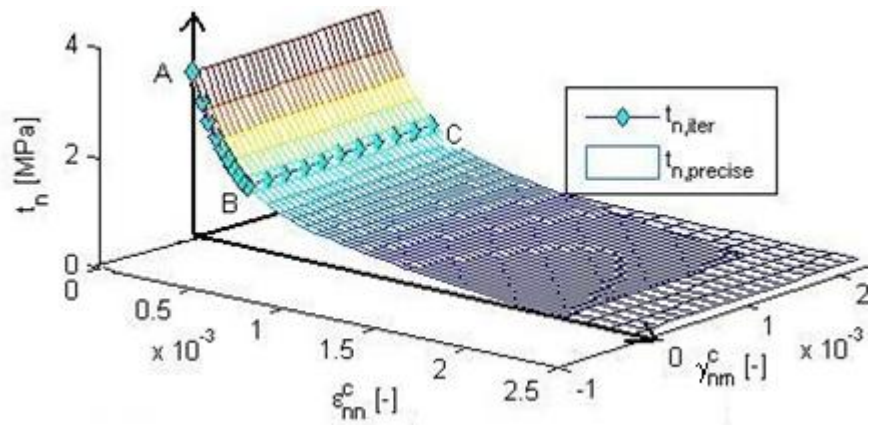


Figure 58 – LC V1: Iterated normal traction $t_{n,iter}$ and normal traction function $t_n(\varepsilon_{nn}^c)$ ($t_{n,precise}$)

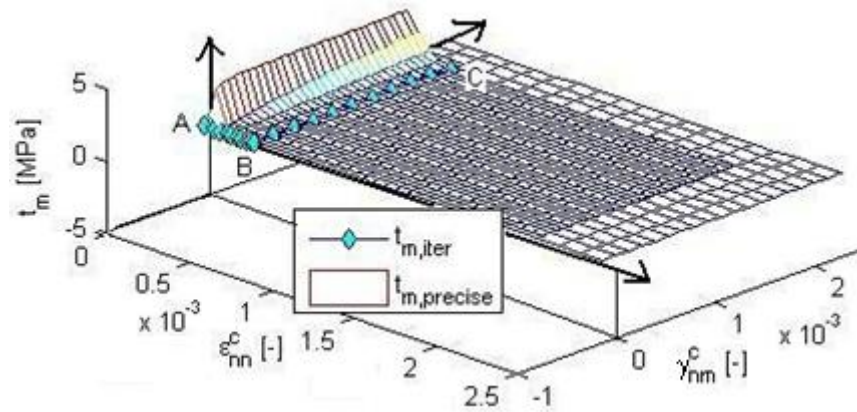


Figure 59 – LC V1: Iterated shear traction $t_{m,iter}$ and shear traction function $t_m(\epsilon_{nn}^c, \gamma_{nm}^c)$ ($t_{m,precise}$)

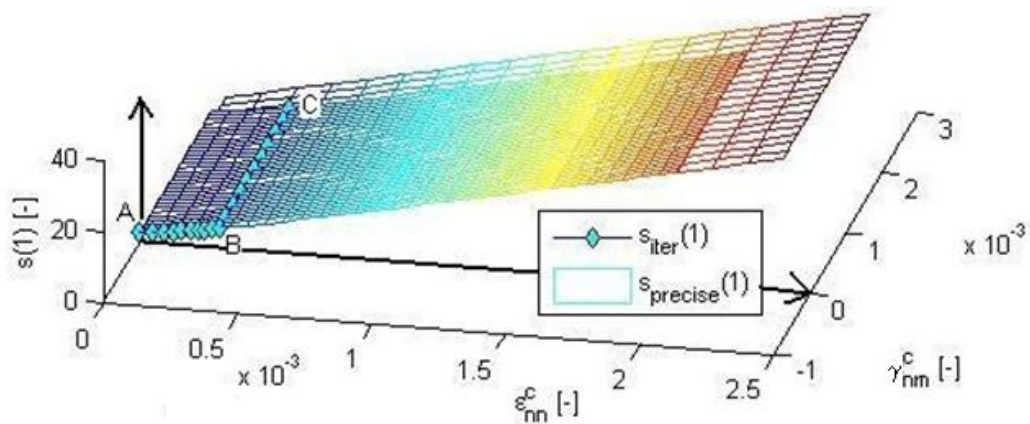


Figure 60 – LC V1: Iteration function $s(1)$: iterated ($s_{iter}(1)$) and the precise function ($s_{precise}(1)$)

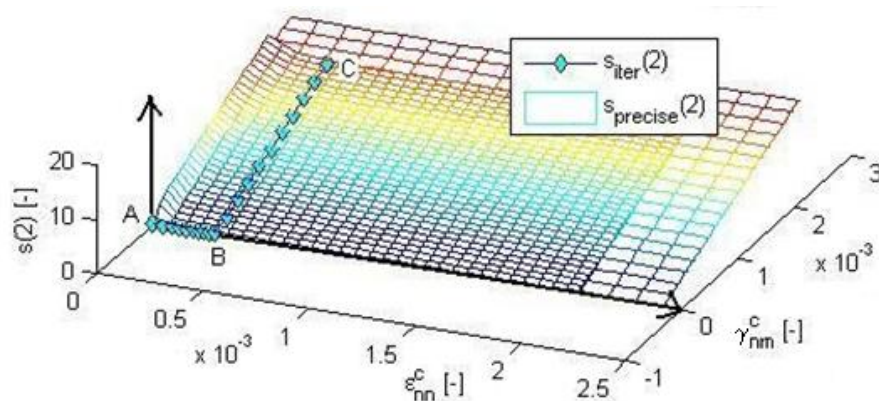


Figure 61 – LC V1: Iteration function $s(2)$: iterated ($s_{iter}(2)$) and the precise function ($s_{precise}(2)$)

5.1.2 LC V2: $\Delta\epsilon_y$ and then $\Delta\gamma_{xy}$, CT2, $\theta = 90^\circ$

Load case V2 prescribes increments of strain in global coordinates $\Delta\epsilon_y^1 = 2 \cdot 10^{-4}$ for step 1 and $\Delta\epsilon_y^{2-10} = 2 \cdot 10^{-5}$ for steps 2-10 and then $\Delta\gamma_{xy}^{11-20} = 2 \cdot 10^{-4}$ for steps 11-20 while $\Delta\epsilon_y = 0$ (see **Figure 62a**). The prescribed strain in local coordinates (n, m) for LC V2 is the same as the prescribed strain in global coordinates (x, y) for LC V1. They both are compared in **Figure 62a** and

Figure 62b. It can be observed that for LC V2 in global coordinates are prescribed positive increments $\Delta\varepsilon_y > 0$ and $\Delta\gamma_{xy} > 0$ ($\Delta\varepsilon_x = 0$) while in local coordinates is strain vector rotated and thus the increment of shear strain is negative $\Delta\gamma_{xy} < 0$ and that of normal strain in x direction is positive $\Delta\varepsilon_x > 0$ ($\Delta\varepsilon_y = 0$).

The course of crack opening is shown in **Figure 62c** where the crack opens first in n direction and then in m direction. The values of crack opening δ_n are the same as in LC V1 ($\delta_n^{V1} = \delta_n^{V2}$) while $\delta_m^{V1} = -\delta_m^{V2}$ due to the opposite orientation of prescribed $\Delta\varepsilon_{xy}$ in local and global coordinates. Stress-strain curves $\sigma_x - \varepsilon_y$, $\sigma_y - \varepsilon_y$ and $\tau_{xy} - \gamma_{xy}$ in LC V2 (**Figure 63**) correspond to $\sigma_x - \varepsilon_x$, $\sigma_y - \varepsilon_x$ and $\tau_{xy} - \gamma_{xy}$ in LC V1 (**Figure 57**).

Results in local coordinates for normal t_n and shear traction t_m and iteration functions $s(1)$, $s(2)$ depend on negative shear crack strain ($\gamma_{nm}^c < 0$), see **Figure 64 - Figure 67**. In **Figure 64 - Figure 67** are marked points of changes A (crack initiation), B (end of uniaxial loading and start of pure shear) and C (end of loading). Thus, normal traction t_n being independent of γ_{nm}^c is defined in CT2 in the same way as in CT1 while t_m is defined in CT2 as an odd function to t_m in CT1.

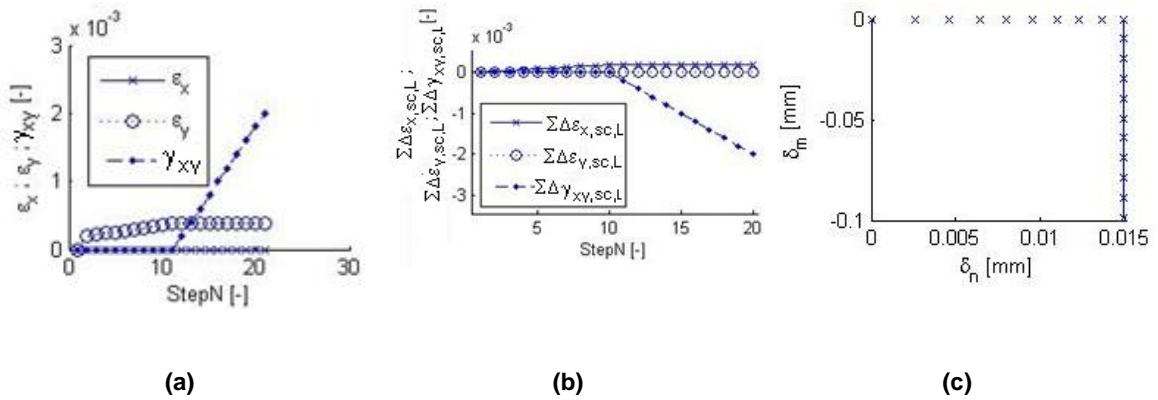


Figure 62 – LC V2: Course of loading strain in global coordinates $\Delta\varepsilon_x, \Delta\varepsilon_y, \Delta\gamma_{xy}$ (a), sum of strain increments in smeared crack region in local coordinates $\Sigma\Delta\varepsilon_{x,sc,L}, \Sigma\Delta\varepsilon_{y,sc,L}, \Sigma\Delta\gamma_{xy,sc,L}$ (b), development of crack opening δ_m with respect to δ_n (c)

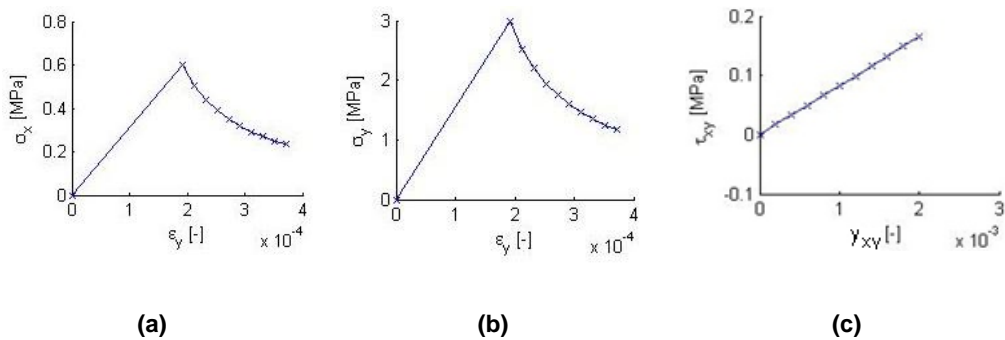


Figure 63 – LC V2: Stress-strain curves in global coordinates $\sigma_x - \varepsilon_y$ (a), $\sigma_y - \varepsilon_y$ (b), $\tau_{xy} - \gamma_{xy}$ (c)

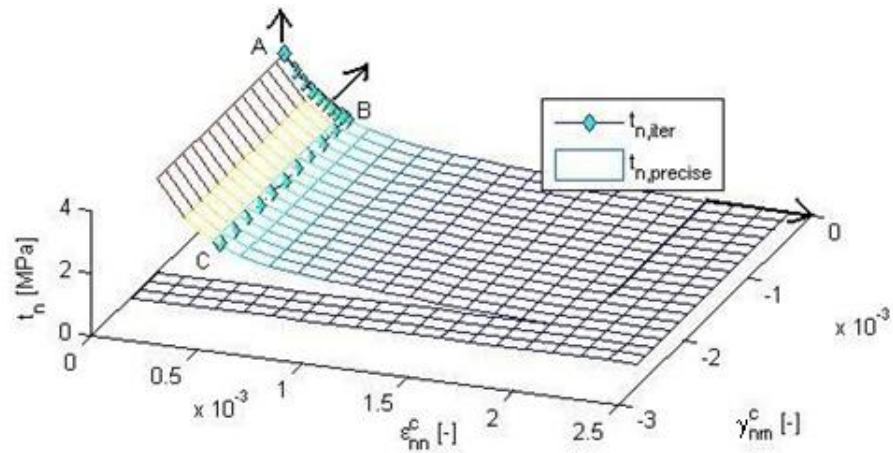


Figure 64 – LC V2: Iterated normal traction $t_{n,iter}$ and normal traction function $t_n(\epsilon_{nn}^c)$ ($t_{n,precise}$)

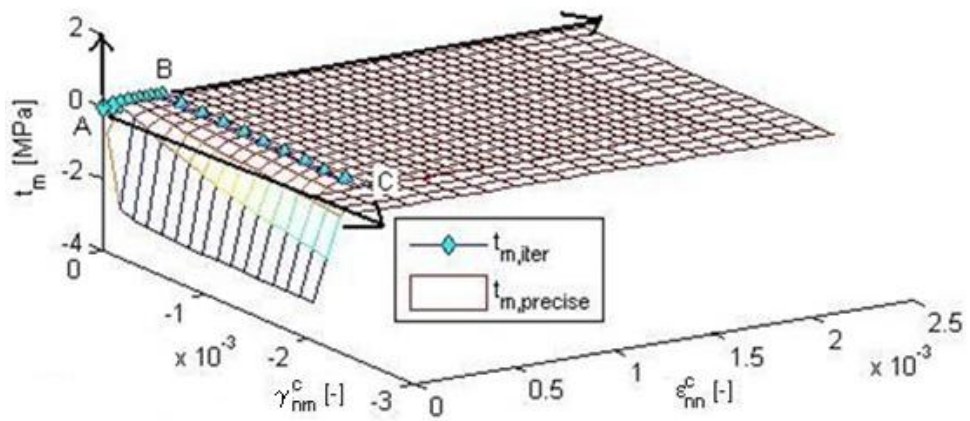


Figure 65 – LC V2: Iterated shear traction $t_{m,iter}$ and shear traction function $t_m(\epsilon_{nn}^c, \gamma_{nm}^c)$ ($t_{m,precise}$)

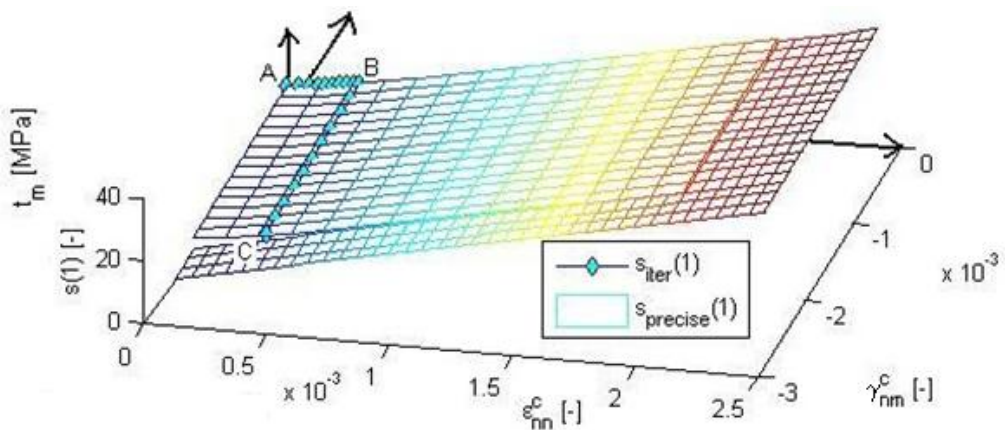


Figure 66 – LC V2: Iteration function $s(1)$: iterated ($s_{iter}(1)$) and the precise function ($s_{precise}(1)$)

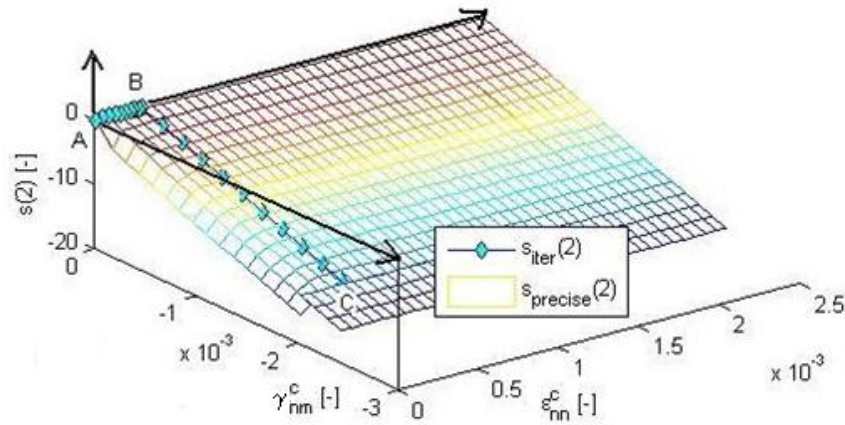


Figure 67 – LC V2: Iteration function $s(2)$: iterated ($s_{iter}(2)$) and the precise function ($s_{precise}(2)$)

5.1.3 LC V3: $\Delta\varepsilon_x$ and then $\Delta\gamma_{xy}$, CT1, $\theta = 20^\circ$

Load case V3 prescribes strain increments for step 1 $\Delta\varepsilon_x^1 = 0.164 \cdot 10^{-3}$, $\Delta\varepsilon_y^1 = 0.095 \cdot 10^{-3}$ and $\Delta\gamma_{xy}^1 = 0.058 \cdot 10^{-3}$ in order to initiate crack deviated by $\theta = 20^\circ$ from positive x axis. For this purpose, the threshold angle is set to $\theta_{CT1,max} = 20^\circ$.

The rest of the loading increments is derived from the global strain increments of LC V1 ($\Delta\varepsilon_G^{V1}$) which are equal to local strain increments of LC V2 ($\Delta\varepsilon_L^{V2}$). In order to use these strain increments in local coordinates for LC V3, they must be prescribed as global strain increments $\Delta\varepsilon_G^{V3}$. Thus, the strain increments $\Delta\varepsilon_L^{V2} = \Delta\varepsilon_L^{V3}$ are transformed in global strain increments $\Delta\varepsilon_G^{V3}$ as follows

$$\Delta\varepsilon_L^{V2} \xrightarrow{\text{transformation}} \Delta\varepsilon_G^{V3} \quad [82]$$

The strain increment was calculated as follows

$$\Delta\varepsilon_G^{V3;2-10} = 2 \cdot 10^{-5} (0.88, 0.12, -0.32)^T; \quad \Delta\varepsilon_G^{V3;10-20} = 2 \cdot 10^{-4} (0.64, -0.64, 0.77)^T \quad [83]$$

The loading is shown in **Figure 68** in global and local coordinates.

It is important to mention that to initiate crack type CT1 across the grain at crack normal deviation angle $\theta = 0^\circ$ and at $\theta = 20^\circ$, the loading in elastic region must be different. Due to the fact, that in fixed smeared crack calculation is used the value of total strain (the sum of elastic and crack strain) both in elastic and inelastic region, it is necessary to replace calculated values of stress and strain in point peak in LC V3 by the values obtained in LC V1. In this way, the results can correspond. Furthermore, we can verify that calculated stress increments in local coordinates in LC V3 are the same as in LC V1 (**Figure 69** and **Figure 57**) (where local and global coordinates are identical) if we compare the course of sum of increments in inelastic region of stress ($\Sigma\Delta\sigma_{sc,L}$) and strain ($\Sigma\Delta\varepsilon_{sc,L}$).

The results in local coordinates for normal traction t_n and shear traction t_m (**Figure 58**, **Figure 59**) and iteration functions $s(1)$ and $s(2)$ (**Figure 60** and **Figure 61**) are the same as in LC V1 or LC V2.

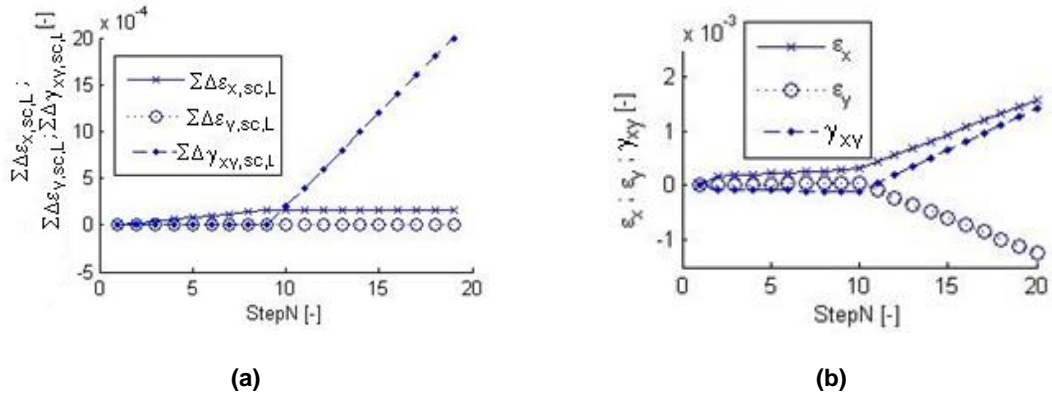


Figure 68 – LC V3: Course of sum of strain increments in smeared crack region in local coordinates $\Sigma \Delta \varepsilon_{x,sc,L}$, $\Sigma \Delta \varepsilon_{y,sc,L}$, $\Sigma \Delta \gamma_{xy,sc,L}$ (a), strain increments in global coordinates $\Delta \varepsilon_x$, $\Delta \varepsilon_y$, $\Delta \gamma_{xy}$ (b)

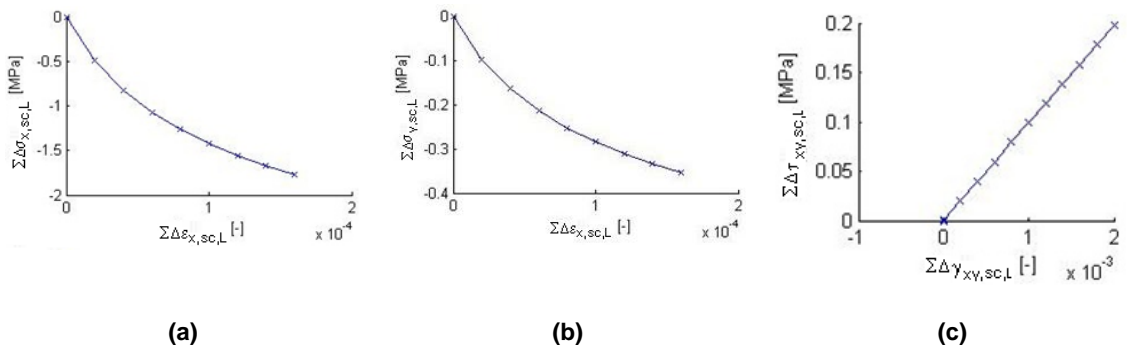


Figure 69 – LC V3: Course of sum of increments in smeared crack region in local coordinates: $\Sigma \Delta \sigma_{x,sc,L}$ - $\Sigma \Delta \varepsilon_{x,sc,L}$ (a), $\Sigma \Delta \sigma_{y,sc,L}$ - $\Sigma \Delta \varepsilon_{x,sc,L}$ (b), $\Sigma \Delta \tau_{xy,sc,L}$ - $\Sigma \Delta \gamma_{xy,sc,L}$ (c)

5.1.4 LC V4: $\Delta \varepsilon_x$ and then $\Delta \gamma_{xy}$, CT1, $\theta = 20^\circ$, minor orthotropy

Load case V4 considers minor orthotropy of the material in the form of $E_y = 0.9E_x$. Other material parameters are the same as in LC V1 – V3. Prescribed strain increment for the first step is $\Delta \varepsilon_x^1 = 0.161 \cdot 10^{-3}$, $\Delta \varepsilon_y^1 = 0.110 \cdot 10^{-3}$ and $\Delta \gamma_{xy}^1 = 0.058 \cdot 10^{-3}$ which is very near to the values in LC V3. These values were calculated considering minor orthotropy for crack type CT1 under $\theta = 20^\circ$.

The rest of the prescribed deformation increments is identical with LC V3. As the loading path of LC V4 is almost the same as the loading path in LC V3 and the orthotropy in LC V4 is almost negligible, almost no difference in results is noticed. For this reason, only course of sum of increments of stress and strain in smeared crack region in local coordinates (Figure 70) are presented in this subchapter.

From visual comparison of sum of increments of stress and strain in smeared crack region in local coordinates for LC V4 (Figure 70) and LC V3 (Figure 69) can be concluded, that resulting increments $\Delta \sigma_{y,p,L}$ slightly decreased as modulus of elasticity E_y was decreased in LC V4. Orthotropic material parameters caused that local stiffness matrix has its elements (1,3), (2,3), (3,1) and (3,2) non-zero and thus resulting shear stress τ_{xy} is influenced not only by shear strain increments $\Delta \varepsilon_{xy}$ but also by normal strain increments $\Delta \varepsilon_x$ and $\Delta \varepsilon_y$. Similarly, stress σ_x is influenced

by $\Delta\gamma_{xy}$ and $\Delta\varepsilon_y$. Local and global stiffness matrices (\mathbf{D}_e^L , \mathbf{D}_e^G) are evaluated for this load case in Eq. [84] and Eq. [85].

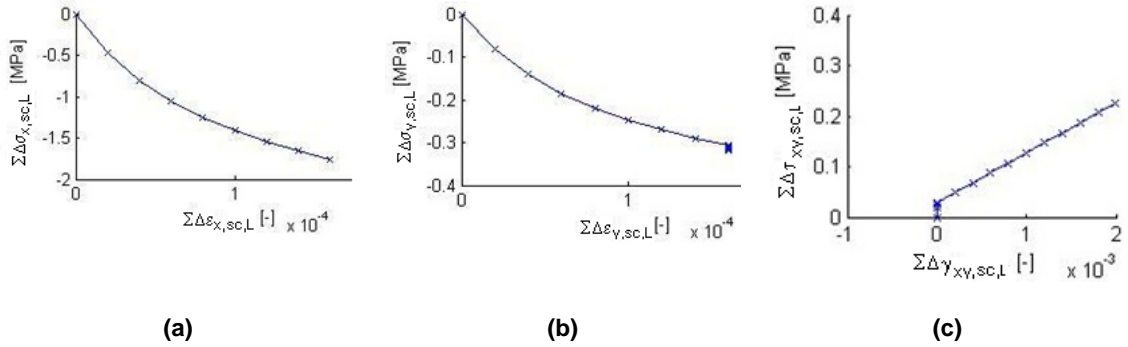


Figure 70 – LC V4: Course of sum of increments of stress and strain in smeared crack region in local coordinates: $\Sigma\Delta\sigma_{x,sc,L} - \Sigma\Delta\varepsilon_{x,sc,L}$ (a), $\Sigma\Delta\sigma_{y,sc,L} - \Sigma\Delta\varepsilon_{y,sc,L}$ (b), $\Sigma\Delta\tau_{xy,sc,L} - \Sigma\Delta\gamma_{xy,sc,L}$ (c)

$$\mathbf{D}_e^L = \begin{pmatrix} 15\,571 & 2\,959 & -47 \\ 2\,720 & 14\,374 & -355 \\ -147 & -455 & 6\,121 \end{pmatrix} \quad [84]$$

$$\mathbf{D}_e^G = \begin{pmatrix} 15\,625 & 3\,125 & 0 \\ 2\,813 & 14\,063 & 0 \\ 0 & 0 & 6\,250 \end{pmatrix} \quad [85]$$

5.2 Model performance with orthotropic material properties

This subchapter describes and discusses results for different load cases (LC) that were obtained by the developed constitutive model with orthotropic material parameters. Load cases are denoted LC CT1-x if they cause a crack across the fibers (CT1) with crack normal deviation from the grain by an angle $\theta \in [0^\circ; \theta_{CT1,max}]$ and LC CT2-x if they cause a crack along the fibers (CT2) with crack normal deviation from the grain by an angle $\theta = 90^\circ$.

5.2.1 LC CT1-1: $\Delta\varepsilon_x$, $\theta = 0^\circ$ (pure tension parallel to grain)

Load case CT1-1 prescribes strain increments $\Delta\varepsilon_x^{1-20} = 2.4 \cdot 10^{-3}$ for all 20 load steps (Figure 71a). Poisson's coefficient is set to zero ($\nu_{xy} = \nu_{yx} = 0$). In Figure 71 - Figure 77, results for LC CT1-1 are plotted.

Crack opens only in n direction ($\delta_n \geq 0$) while in m direction is closed ($\delta_n = 0$), see Figure 71b. Due to zero Poisson's ratio and loading path, the only non-zero stress component is σ_x (Figure 72, Figure 73a). In Figure 73b, development of non-zero elements of tangent stiffness matrix \mathbf{D}_{ec} is shown. Non-zero values are obtained in calculation for iterated normal traction t_n while shear traction t_m is zero. Stress-strain curves in smeared crack region (after the peak stress is reached) correspond to the course of iterated components of traction vector t_n (Figure 74) and t_m (Figure 75) based on iterated values of iteration functions $s(1)$ and $s(2)$ (Figure 76 and Figure 77). Turning points A (crack initiation) and B (end of loading path) are denoted in Figure 74 - Figure 77.

In case Poisson's ratio is non-zero ($\nu_{xy} = \nu_{yx} = 0.023$), calculated stress σ_y is also non-zero and influenced by $\Delta\varepsilon_x$, see Figure 78.

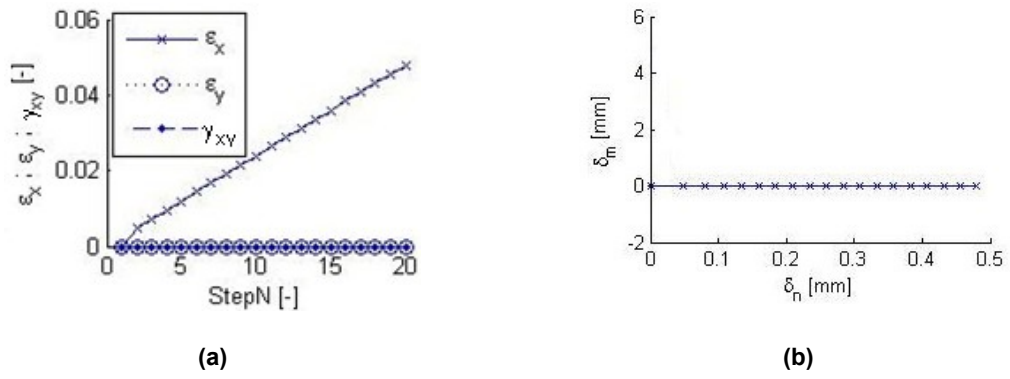


Figure 71 – LC CT1-1: Course of loading run by strain increments $\Delta\varepsilon_x$, $\Delta\varepsilon_y$, $\Delta\gamma_{xy}$ (a), development of crack opening δ_m with respect to δ_n (b)

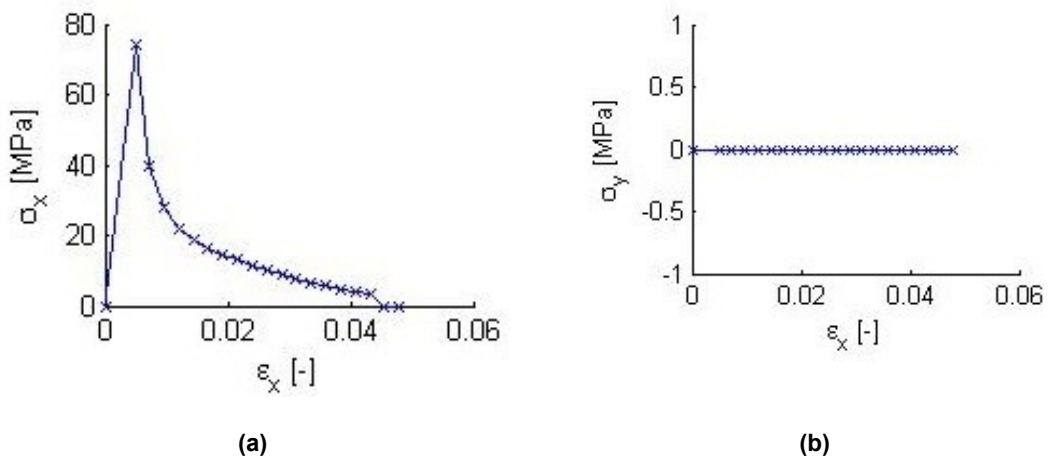


Figure 72 – LC CT1-1: Stress-strain curve $\sigma_x - \varepsilon_x$ (a), $\sigma_y - \varepsilon_x$ (b)

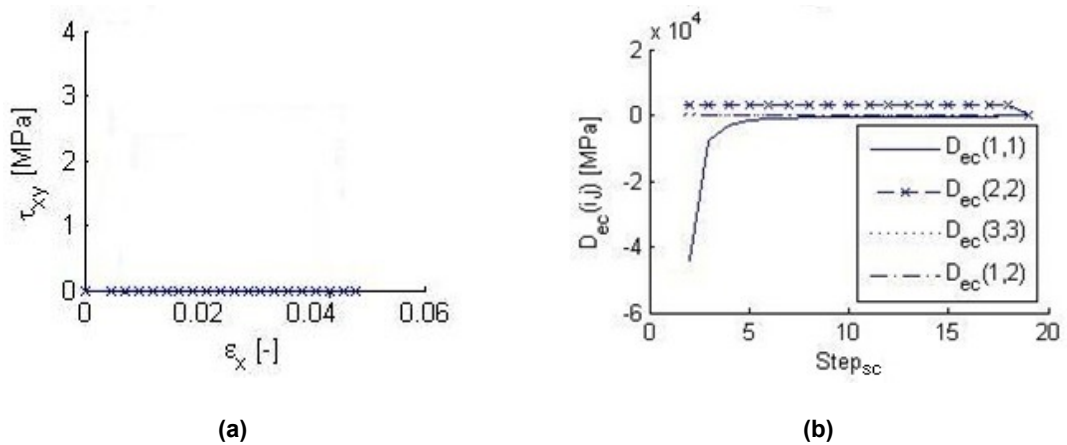


Figure 73 – LC CT1-1: Stress-strain curve $\tau_{xy} - \varepsilon_x$ (a), development of non-zero elements of tangent stiffness matrix D_{ec} (b)

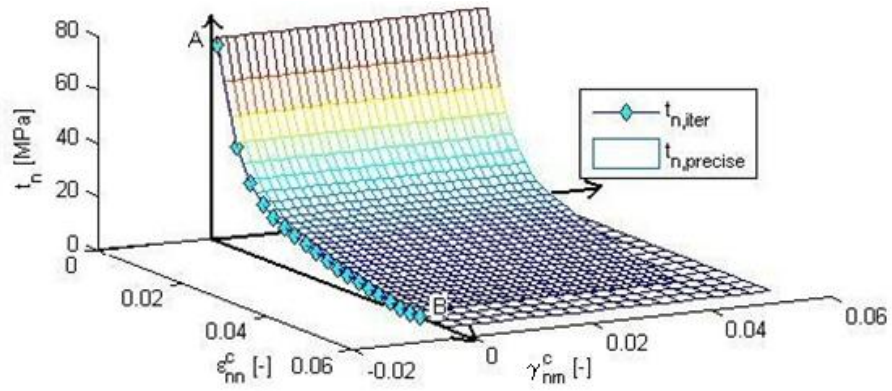


Figure 74 – LC CT1-1: Iterated normal traction $t_{n,iter}$ and normal traction function $t_n(\epsilon_{nn}^c)$ ($t_{n,precise}$)

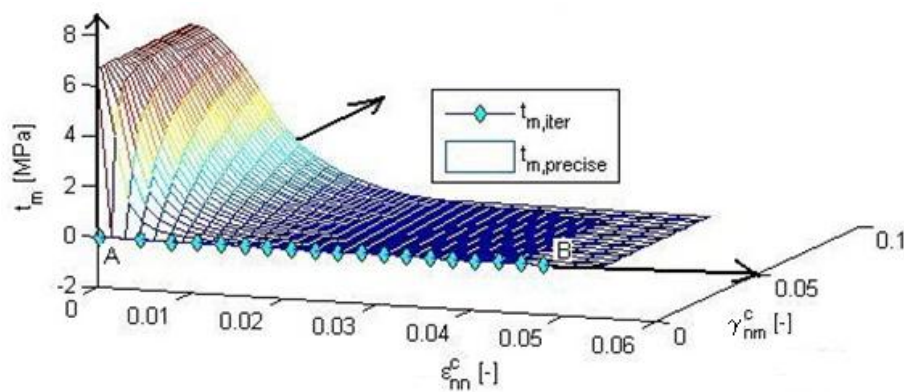


Figure 75 – LC CT1-1: Iterated shear traction $t_{m,iter}$ and shear traction function $t_m(\epsilon_{nn}^c, \gamma_{nm}^c)$ ($t_{m,precise}$)

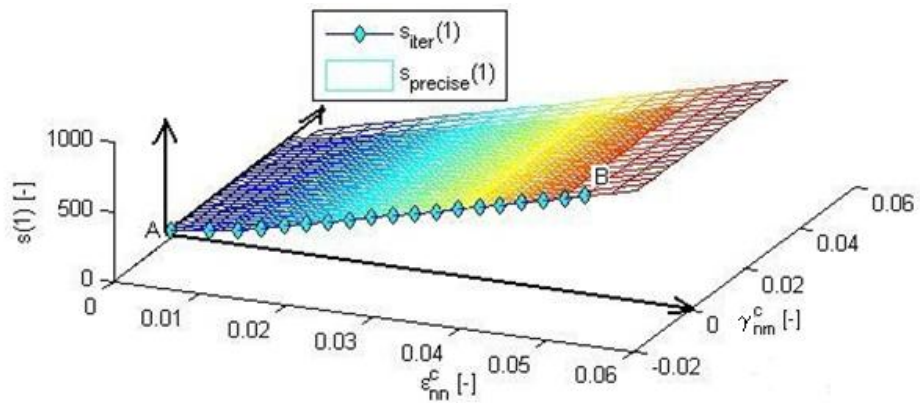


Figure 76 – LC CT1-1: Iteration function $s(1)$: iterated ($s_{iter}(1)$) and the precise function ($s_{precise}(1)$)

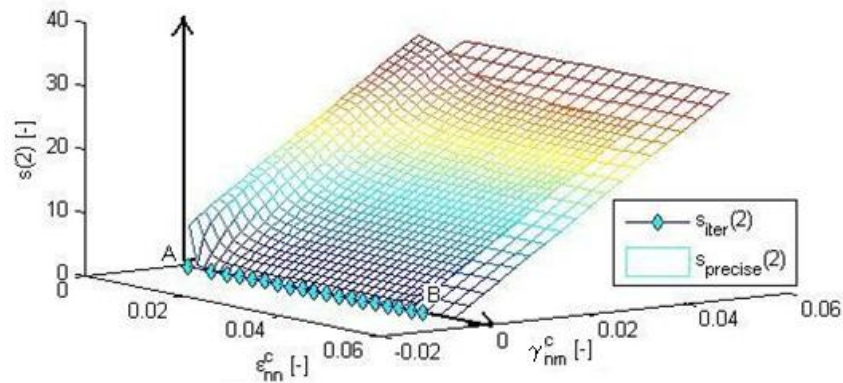


Figure 77 – LC CT1-1: Iteration function $s(2)$: iterated ($s_{iter}(2)$) and the precise function ($s_{precise}(2)$)

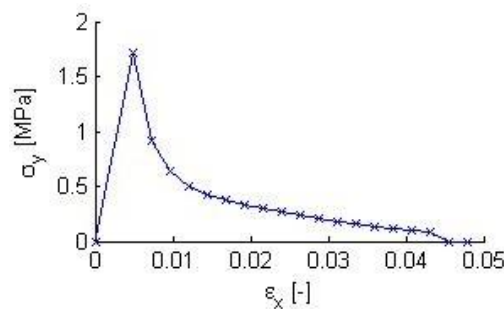


Figure 78 – LC CT1-1: Stress-strain curve $\sigma_y - \epsilon_x$ if $\nu_{xy} = \nu_{yx} = 0.023$

5.2.2 LC CT1-2: $\Delta\epsilon_x$ and then $\Delta\gamma_{xy}$, $\theta = 0^\circ$

Load case CT1-2 prescribes strain increments $\Delta\epsilon_x^{1-10} = 8 \cdot 10^{-4}$ and $\Delta\epsilon_x^{11-20} = 6 \cdot 10^{-3}$ for load steps 1-10 and 11-20 (Figure 79a). Results for this LC CT1-2 are plotted in Figure 79 – Figure 85.

Crack opens in n direction ($\delta_n \geq 0$) if $\Delta\epsilon_x > 0$ and in m direction ($\delta_m \geq 0$) if $\Delta\epsilon_{xy} > 0$ (Figure 79b).

Stress-strain curves are plotted in Figure 80 and Figure 81.

Course of the calculation is expressed by means of iterated components of traction vector t_n and t_m (Figure 82, Figure 83) and iterated values of iteration functions $s(1)$ and $s(2)$ (Figure 84 and Figure 85). In Figure 82 - Figure 85 are denoted turning points A (crack initiation), B (end of pure tension, start of pure shear), C (value of critical crack opening δ_{crit} is reached) and D (end of loading path). It can be observed that crack stops transferring stresses at point C as stress σ and iterated components of traction vector ($t_{n,iter}$, $t_{m,iter}$) drop to zero.

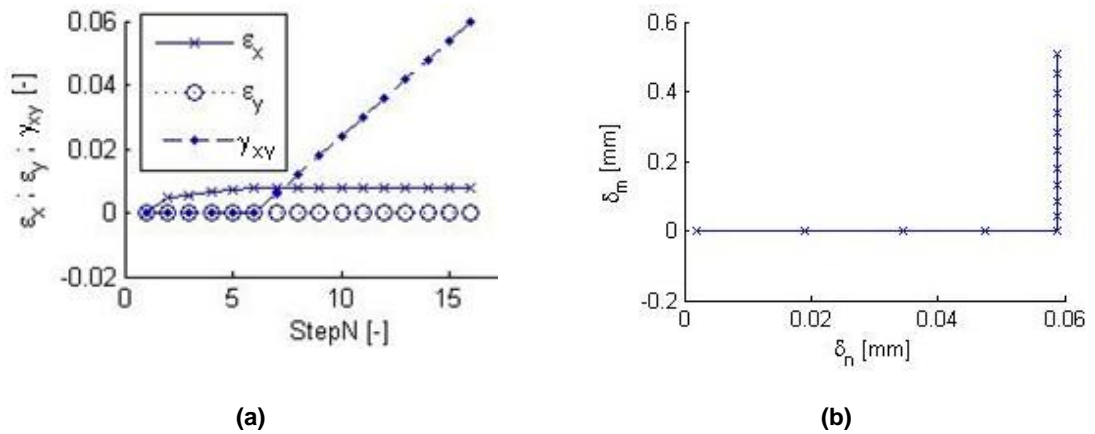


Figure 79 – LC CT1-2: Course of loading run by strain increments $\Delta\varepsilon_x$, $\Delta\varepsilon_y$, $\Delta\gamma_{xy}$ (a), development of crack opening δ_m with respect to δ_n (b)

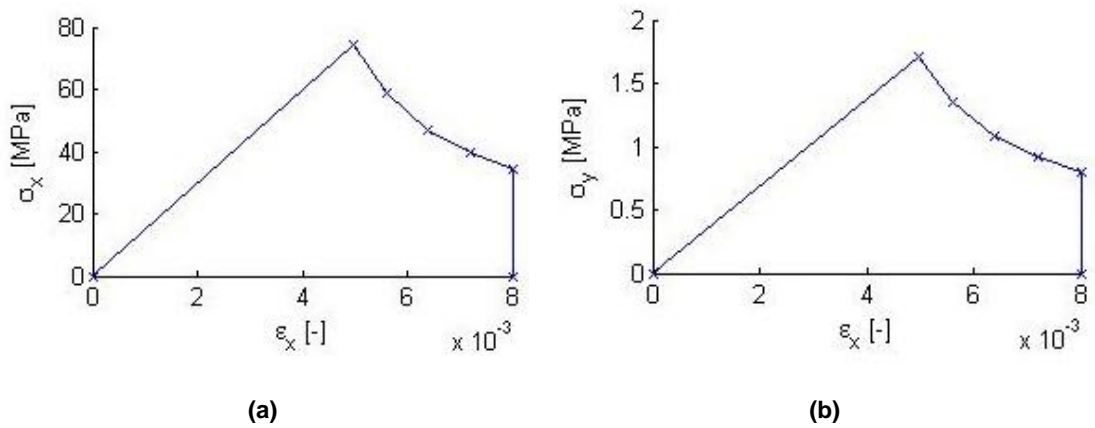


Figure 80 – LC CT1-2: Stress-strain curve $\sigma_x - \varepsilon_x$ (a), $\sigma_y - \varepsilon_x$ (b)

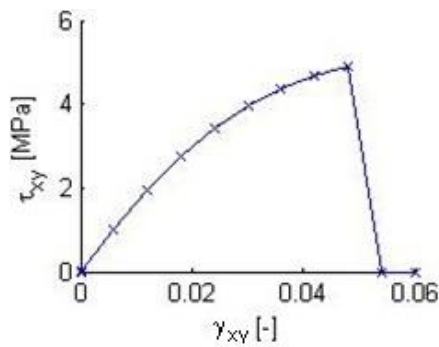


Figure 81 – LC CT1-2: Stress-strain curve $\tau_{xy} - \gamma_{xy}$

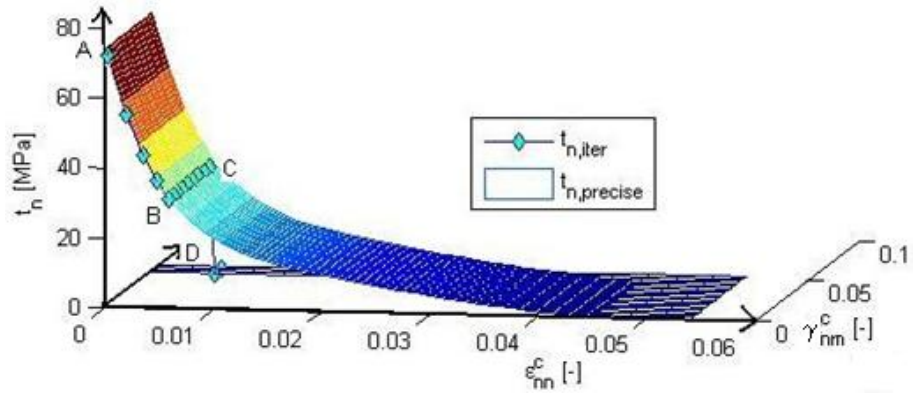


Figure 82 – LC CT1-2: Iterated normal traction $t_{n,iter}$ and normal traction function $t_n(\epsilon_{nn}^c)$ ($t_{n,precise}$)

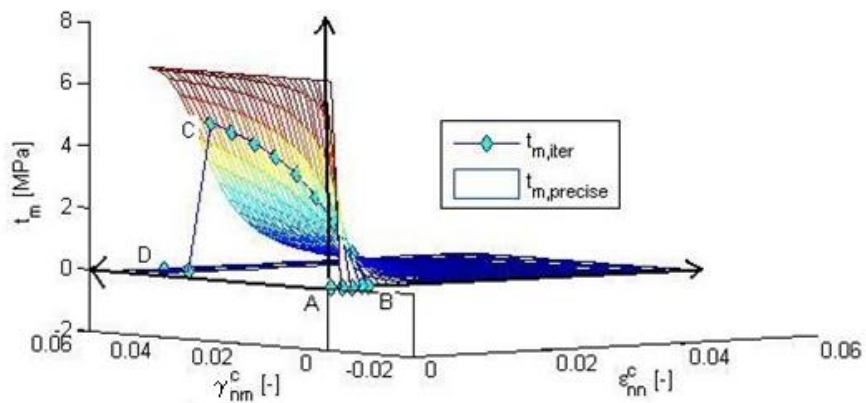


Figure 83 – LC CT1-2: Iterated shear traction $t_{m,iter}$ and shear traction function $t_m(\epsilon_{nn}^c, \gamma_{nm}^c)$ ($t_{m,precise}$)

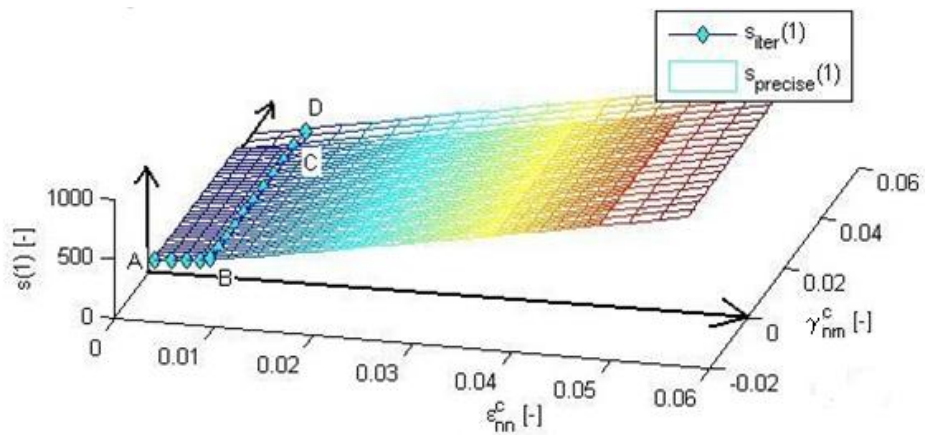


Figure 84 – LC CT1-2: Iteration function $s(1)$: iterated ($s_{iter}(1)$) and the precise function ($s_{precise}(1)$)

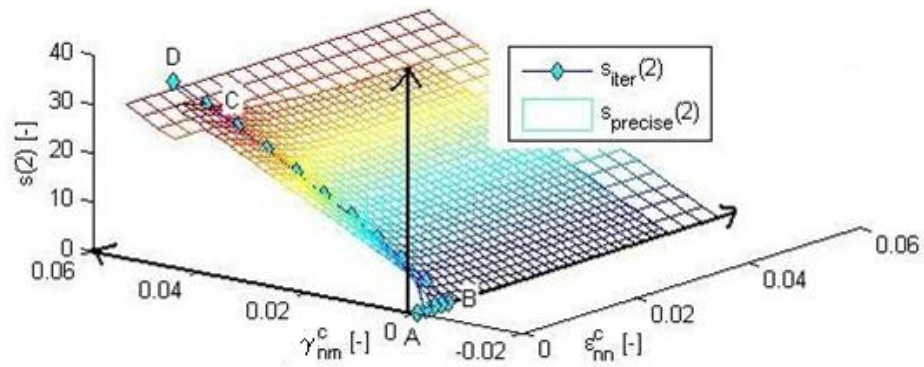


Figure 85 – LC CT1-2: Iteration function $s(2)$: iterated ($s_{iter}(2)$) and the precise function ($s_{precise}(2)$)

5.2.3 LC CT1-3: $\Delta\epsilon_x \wedge \Delta\gamma_{xy}$, $\theta = 4.5^\circ$

LC CT1-3 prescribes strain increments $\Delta\epsilon_x^{1,3} = 3 \cdot 10^{-3}$, $\Delta\epsilon_x^{4-18} = 2 \cdot 10^{-3}$ and $\Delta\gamma_{xy}^{2-18} = 3 \cdot 10^{-3}$ (Figure 86a). First two steps ensure the crack type CT1 and crack normal deviation angle $\theta = 4.5^\circ$ of an initiated crack. Results for this LC CT1-3 are plotted in Figure 86 - Figure 92.

Crack opens in both n and m direction ($\delta_n \geq 0$ and $\delta_m \geq 0$) for $\Delta\epsilon_x > 0$ and $\Delta\gamma_{xy} > 0$ (Figure 86b). Stress-strain curves are plotted in Figure 87 and Figure 88 where can be observed that the shape of stress-strain curve with respect to ϵ_x is very similar to that with respect to γ_{xy} .

Course of the calculation is expressed by means of iterated components of traction vector t_n and t_m (Figure 88, Figure 89) and iterated values of iteration functions $s(1)$ and $s(2)$ (Figure 91 and Figure 92). In Figure 88 - Figure 85 are denoted turning points A (crack initiation), B (value of critical crack opening δ_{crit} is reached) and C (the end of the loading path). It can be observed that crack stops transferring stresses at point C as stress σ and iterated components of traction vector ($t_{n,iter}$, $t_{m,iter}$) drop to zero.

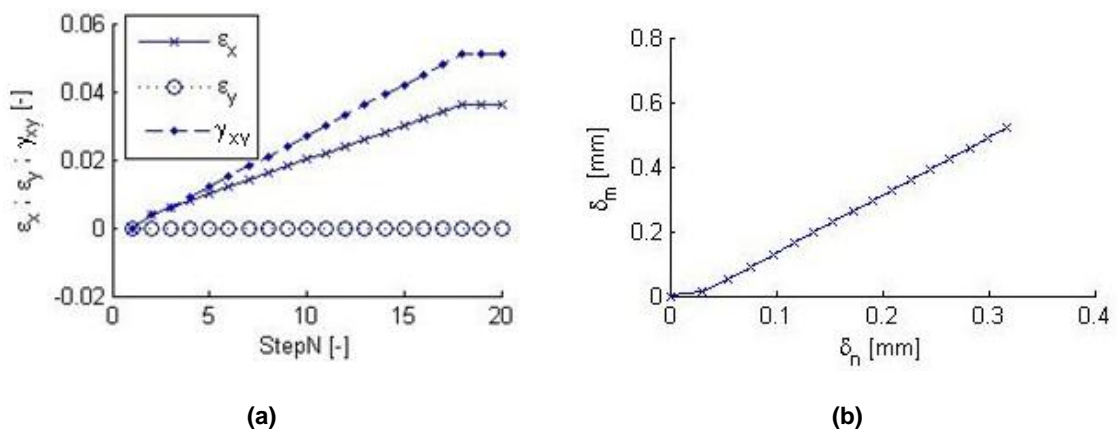


Figure 86 – LC CT1-3: Course of loading run by strain increments $\Delta\epsilon_x$, $\Delta\epsilon_y$, $\Delta\gamma_{xy}$ (a), development of crack opening δ_m with respect to δ_n (b)

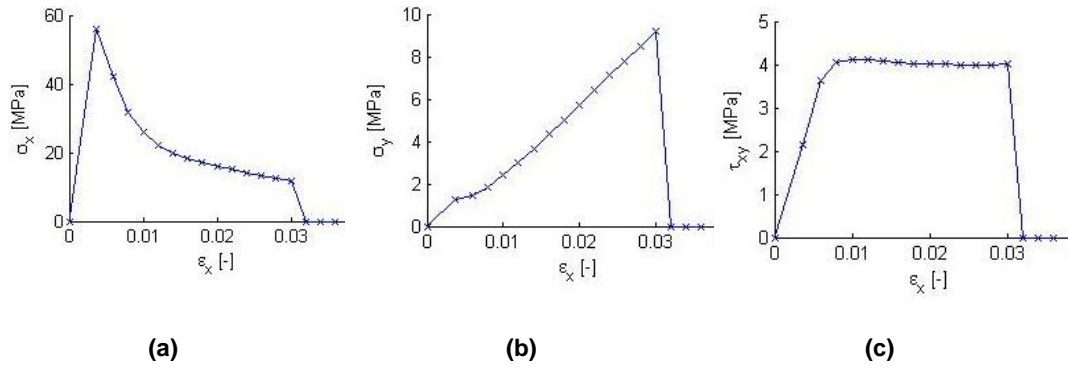


Figure 87 – LC CT1-3: Stress-strain curves $\sigma_x - \epsilon_x$ (a), $\sigma_y - \epsilon_x$ (b), $\tau_{xy} - \epsilon_x$ (c)

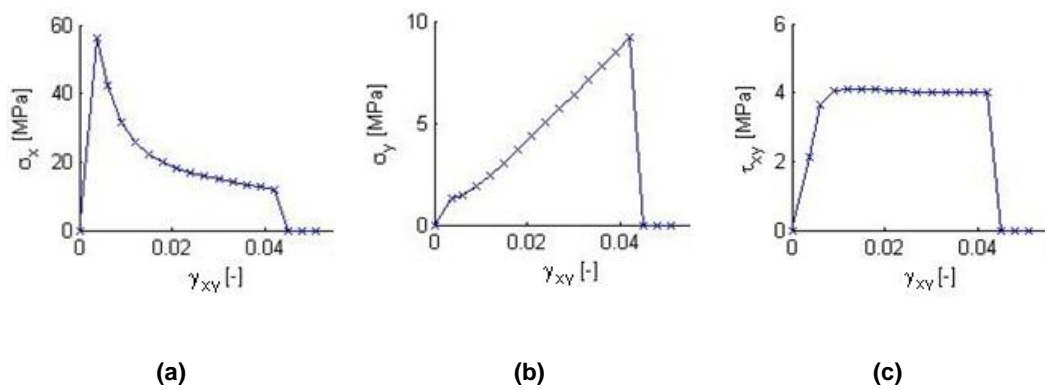


Figure 88 – LC CT1-3: Stress-strain curves $\sigma_x - \gamma_{xy}$ (a), $\sigma_y - \gamma_{xy}$ (b), $\tau_{xy} - \gamma_{xy}$ (c)

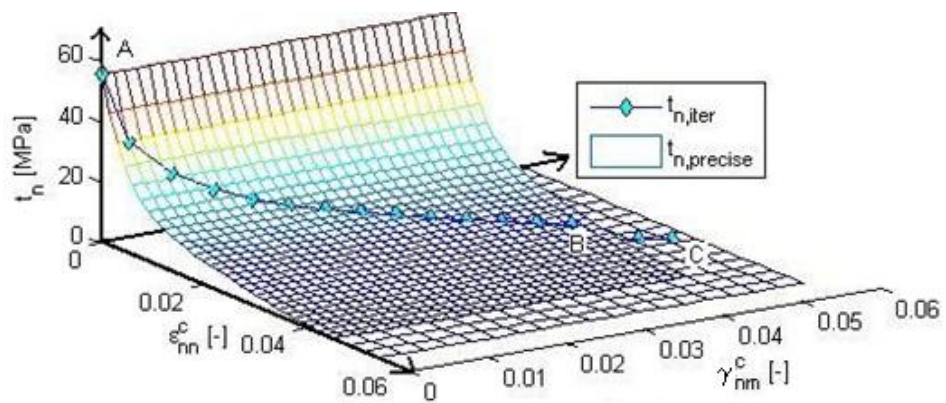


Figure 89 – LC CT1-3: Iterated normal traction $t_{n,iter}$ and normal traction function $t_n(\epsilon_{nn}^c)$ ($t_{n,precise}$)

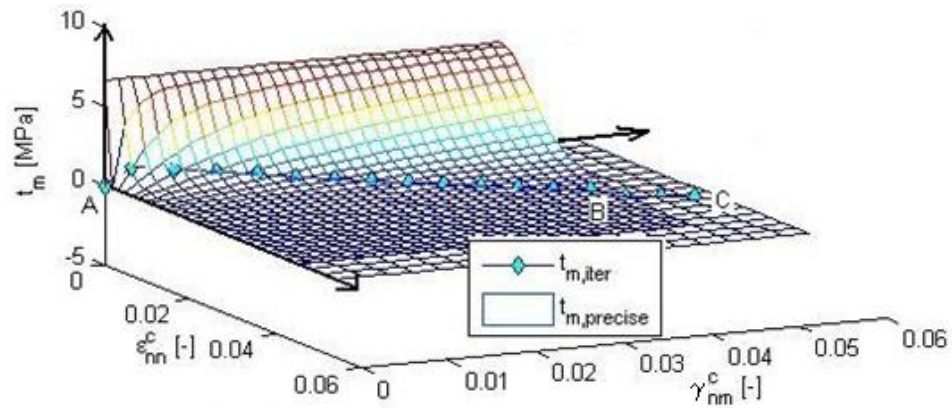


Figure 90 – LC CT1-3: Iterated shear traction $t_{m,iter}$ and shear traction function $t_m(\epsilon_{nn}^c, \gamma_{nm}^c)$ ($t_{m,precise}$)

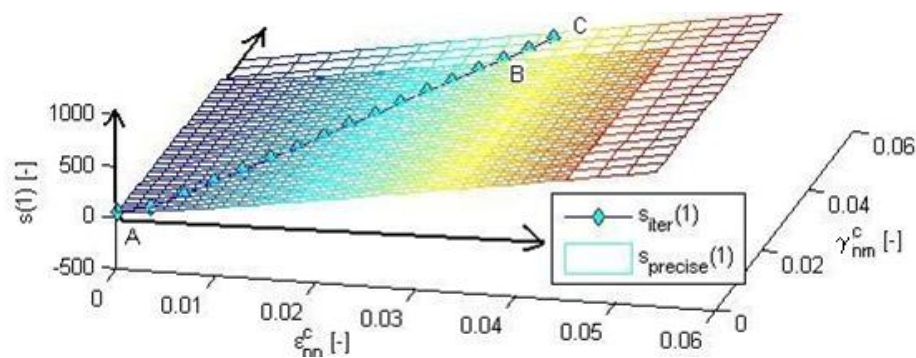


Figure 91 – LC CT1-3: Iteration function $s(1)$: iterated ($s_{iter}(1)$) and precise ($s_{precise}(1)$)

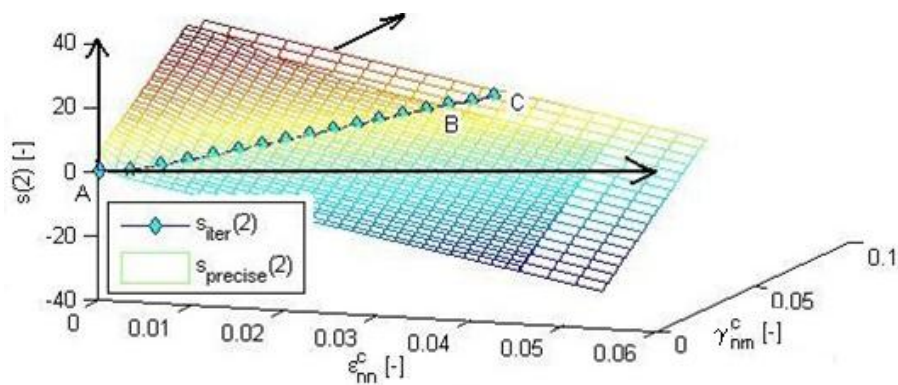


Figure 92 – LC CT1-3: Iteration function $s(2)$: iterated ($s_{iter}(2)$) and precise ($s_{precise}(2)$)

5.2.4 LC CT1-4: $\Delta\epsilon_x$ or $\pm\Delta\gamma_{xy}$, $\theta = 0^\circ$

Load case CT1-4 prescribes strain increments for different steps $\Delta\epsilon_x^{1-2} = \Delta\epsilon_x^{13-14} = 5 \cdot 10^{-3}$, $\Delta\gamma_{xy}^{3-7} = \Delta\gamma_{xy}^{15-18} = 2 \cdot 10^{-3}$ and $\Delta\gamma_{xy}^{8-12} = -2 \cdot 10^{-3}$ (Figure 93a). The results are plotted in Figure 93 - Figure 99.

Crack opens in n or m direction if $\Delta\epsilon_x > 0$ or $\Delta\gamma_{xy} > 0$, see Figure 93b. Stress-strain curves are plotted in Figure 94 and Figure 95 where can be observed that $\Delta\epsilon_x$ does not influence τ_{xy} and $\Delta\gamma_{xy}$ does not influence σ_x .

Course of the calculation is expressed by means of iterated components of traction vector t_n and t_m (Figure 96, Figure 97) and iterated values of iteration functions $s(1)$ and $s(2)$ (Figure 98 and Figure 99). In Figure 96 - Figure 99 are denoted turning points A (crack initiation), B (end of $\Delta\varepsilon_x$, beginning of $+\Delta\gamma_{xy}$), C (beginning of $-\Delta\gamma_{xy}$), D (beginning of $\Delta\varepsilon_x$), E(end of $\Delta\varepsilon_x$, beginning of $+\Delta\varepsilon_{xy}$) and F (end of loading path). It can be observed that the crack does not reach its critical opening δ_{crit} and thus it can transfer all stresses during the whole loading path.

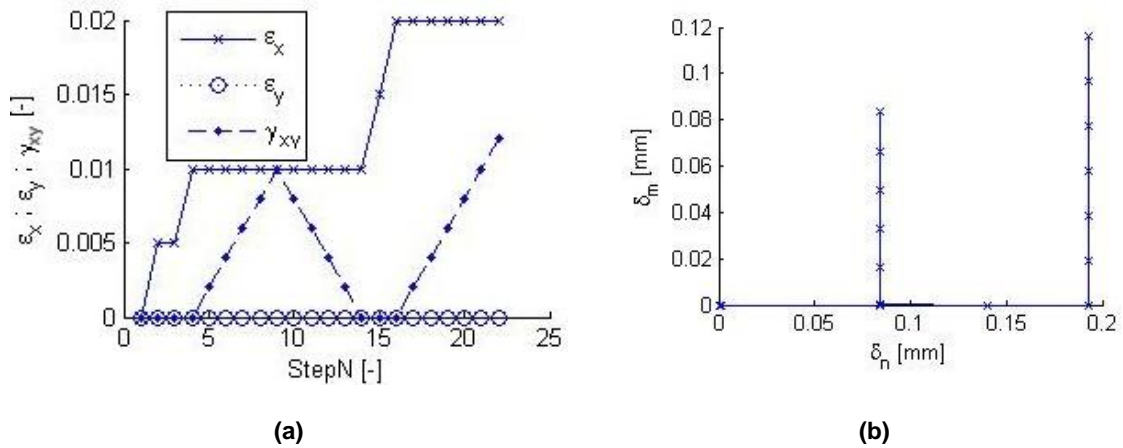


Figure 93 – LC CT1-4: Course of loading run by strain increments $\Delta\varepsilon_x$, $\Delta\varepsilon_y$, $\Delta\gamma_{xy}$ (a), development of crack opening δ_m with respect to δ_n (b)

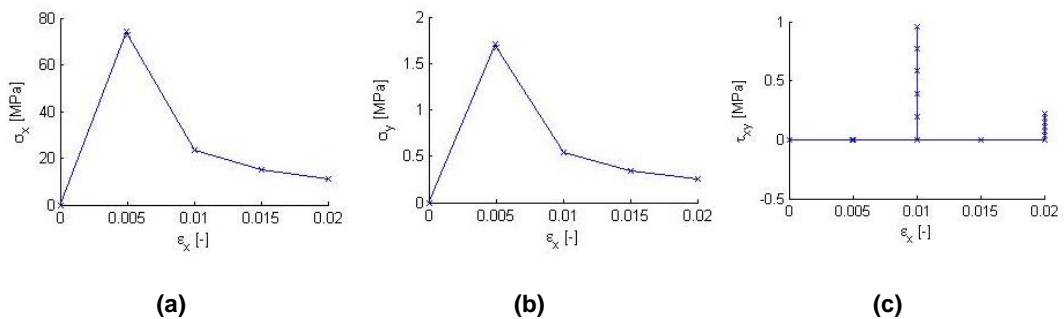


Figure 94 – LC CT1-4: Stress-strain curves $\sigma_x - \varepsilon_x$ (a), $\sigma_y - \varepsilon_x$ (b), $\tau_{xy} - \varepsilon_x$ (c)

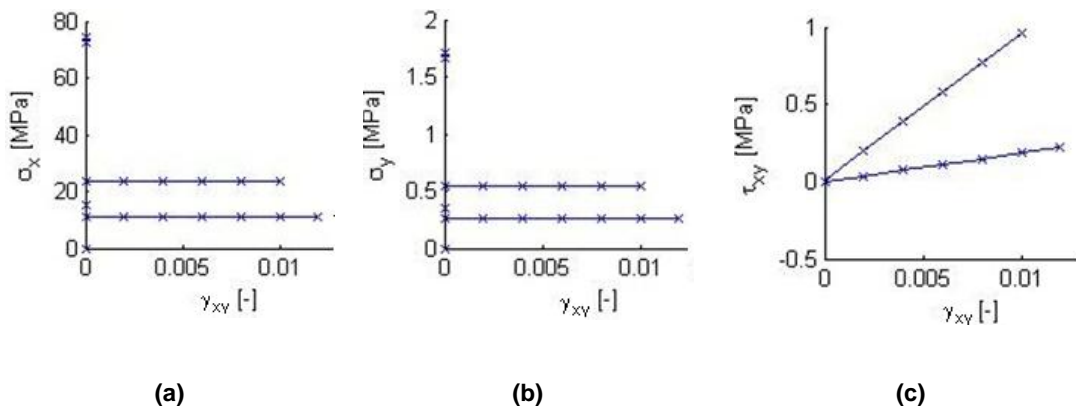


Figure 95 – LC CT1-4: Stress-strain curves $\sigma_x - \gamma_{xy}$ (a), $\sigma_y - \gamma_{xy}$ (b), $\tau_{xy} - \gamma_{xy}$ (c)

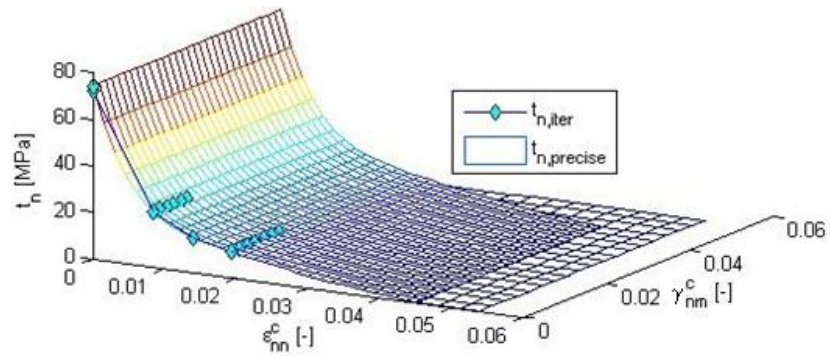


Figure 96 – LC CT1-4: Iterated normal traction $t_{n,iter}$ and normal traction function $t_n(\epsilon_{nn}^c)$ ($t_{n,precise}$)

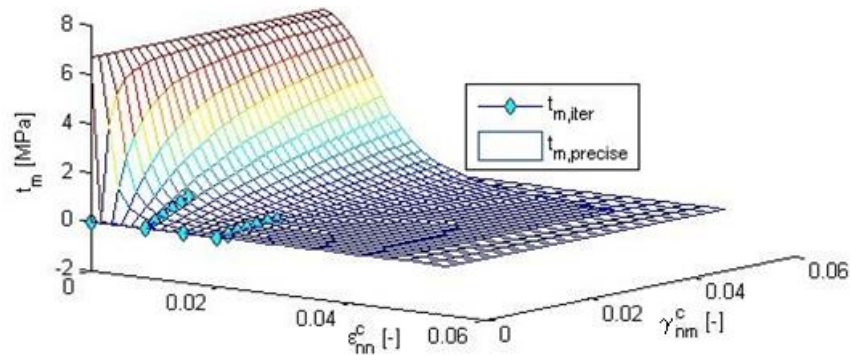


Figure 97 – LC CT1-4: Iterated shear traction $t_{m,iter}$ and shear traction function $t_m(\epsilon_{nn}^c, \gamma_{nm}^c)$ ($t_{m,precise}$)

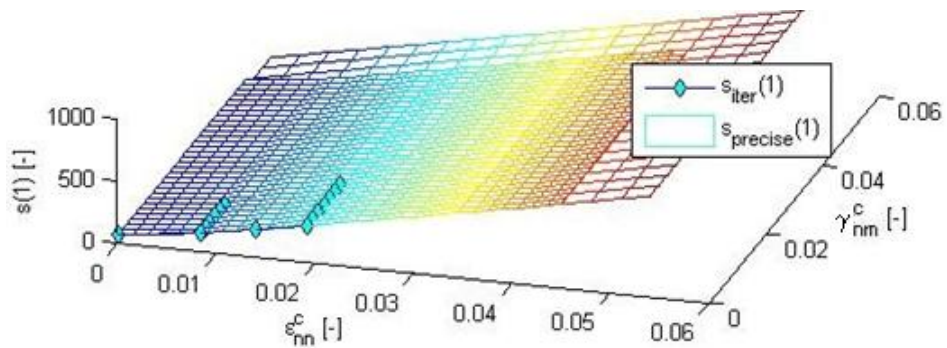


Figure 98 – LC CT1-4: Iteration function $s(1)$: iterated ($s_{iter}(1)$) and the precise function ($s_{precise}(1)$)

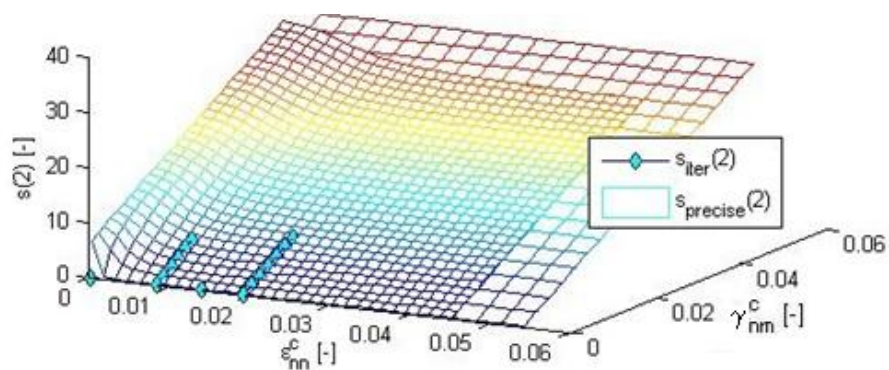


Figure 99 – LC CT1-4: Iteration function $s(2)$: iterated ($s_{iter}(2)$) and the precise function ($s_{precise}(2)$)

5.2.5 LC CT2-1: $\Delta\varepsilon_y, \theta = 90^\circ$ (pure tension perpendicular to the grain)

Load case CT2-1 prescribes strain increments $\Delta\varepsilon_y^{1-20} = 4 \cdot 10^{-4}$ (Figure 100a). Behavior of the material in CT2 under load conditions CT2-1 (pure tension perpendicular to the grain) is analogical to LC CT1-1 (pure tension parallel to grain). The difference consists in rotation between local and global coordinates. The results are plotted in Figure 100 – Figure 105.

Crack opens only in n direction as $\Delta\varepsilon_y > 0$, see Figure 100b. Stress-strain curves are plotted in Figure 101 where can be observed that $\Delta\varepsilon_y$ does not influence τ_{xy} ($\tau_{xy} = 0$).

Course of the calculation is expressed by means of iterated components of traction vector t_n and t_m (Figure 102 and Figure 103, respectively) and iterated values of iteration functions $s(1)$ and $s(2)$ (Figure 104 and Figure 105, respectively). In Figure 102 - Figure 105 are denoted turning points A (crack initiation), B (value of critical crack opening δ_{crit} is reached) and C (end of loading path). It can be observed that the crack reaches its critical opening δ_{crit} in n direction and thus no sudden drop in stress occurs and the course of stress is continuous.

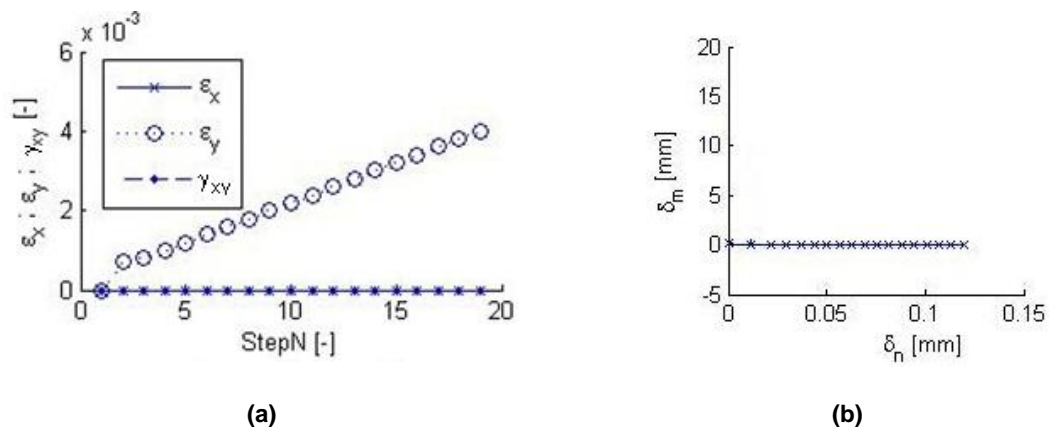


Figure 100 – LC CT2-1: Course of loading run by strain increments $\Delta\varepsilon_x, \Delta\varepsilon_y, \Delta\gamma_{xy}$ (a), development of crack opening δ_m with respect to δ_n (b)

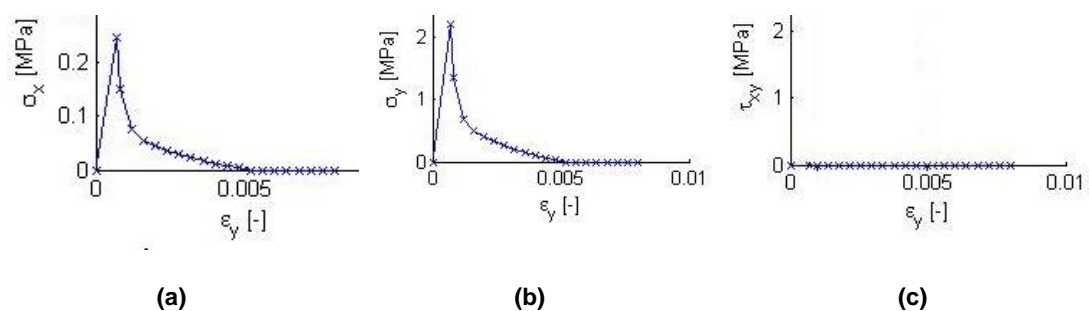


Figure 101 – LC CT2-1: Stress-strain curves $\sigma_x - \varepsilon_y$ (a), $\sigma_y - \varepsilon_y$ (b), $\tau_{xy} - \varepsilon_y$ (c)

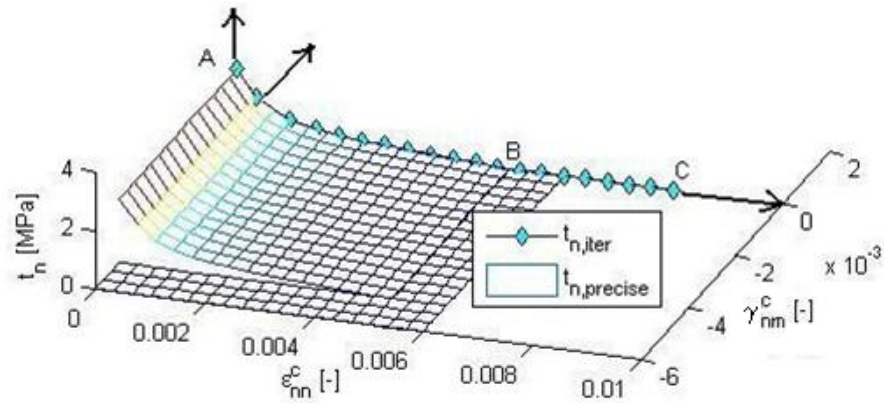


Figure 102 – LC CT2-1: Iterated normal traction $t_{n,iter}$ and normal traction function $t_n(\epsilon_{nn}^c)$ ($t_{n,precise}$)

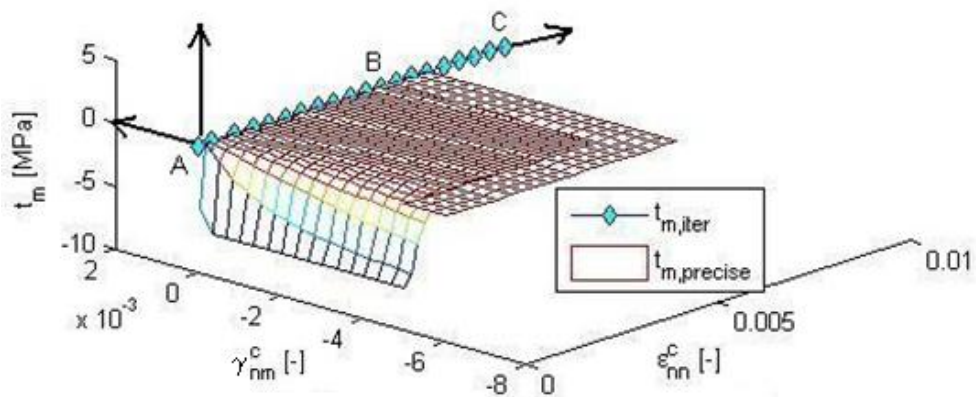


Figure 103 – LC CT2-1: Iterated shear traction $t_{m,iter}$, shear traction function $t_m(\epsilon_{nn}^c, \gamma_{nm}^c)$ ($t_{m,precise}$)

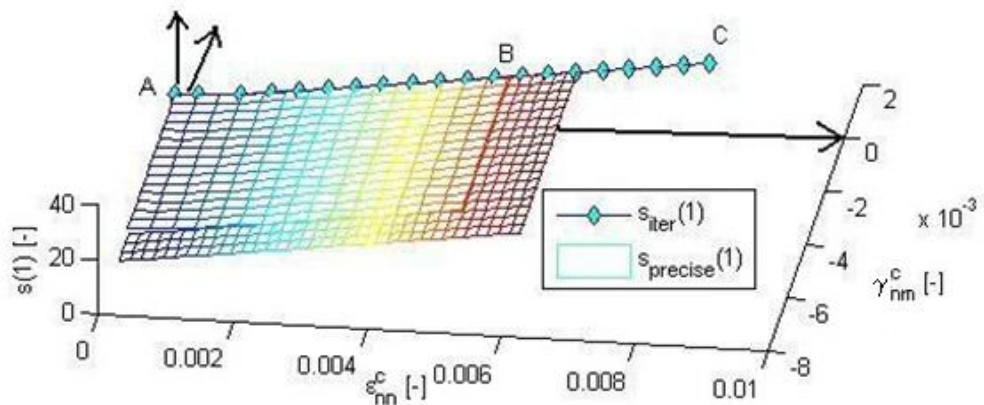


Figure 104 – LC CT2-1: Iteration function $s(1)$: iterated ($s_{iter}(1)$) and the precise function ($s_{precise}(1)$)

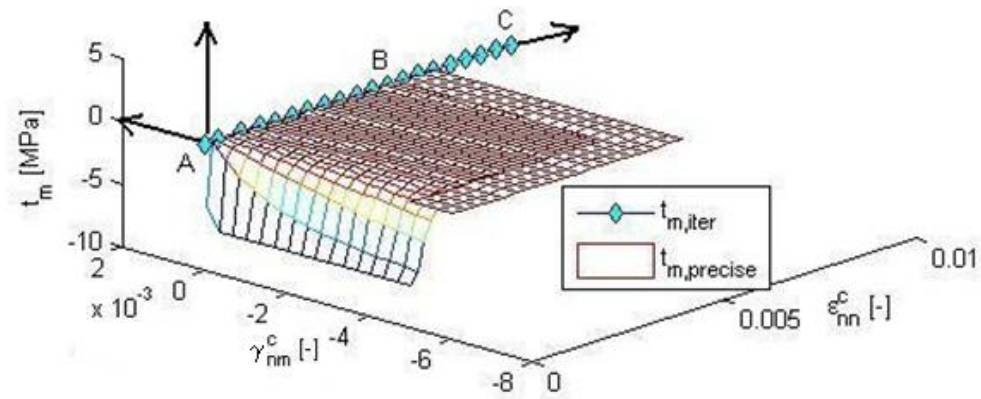


Figure 105 – LC CT2-1: Iteration function $s(2)$: iterated ($s_{iter}(2)$) and the precise function ($s_{precise}(2)$)

5.2.6 LC CT2-2: $\Delta\epsilon_y \wedge \Delta\gamma_{xy}$, $\theta = 90^\circ$

Load case CT2-2 prescribes strain increments $\Delta\epsilon_y^{1-20} = 3 \cdot 10^{-4}$, $\Delta\gamma_{xy}^{1-10} = 5 \cdot 10^{-4}$ and $\Delta\gamma_{xy}^{11-20} = 1 \cdot 10^{-4}$ (Figure 106a). Behavior of the material in LC CT2-2 is analogical to LC CT1-3. The difference consists in rotation between local and global coordinates and its impact on stiffness matrix. The results are plotted in Figure 106 - Figure 112.

Crack opens only in both n and m direction as $\Delta\epsilon_y > 0$ and $\Delta\epsilon_{xy} > 0$, see Figure 106b. Stress-strain curves are plotted in Figure 107 and Figure 108. It ought to be noticed that course of τ_{xy} is similar to the course of σ_x not due to the shape of softening function of cohesive law t_n but due to its path on the surface t_m . The values of $t_{m,iter}$ are negative but the calculated stress is finally positive as their values in local coordinates are transformed into global coordinates.

Course of the calculation is expressed by means of iterated components of traction vector t_n and t_m (Figure 109, Figure 110) and iterated values of iteration functions $s(1)$ and $s(2)$ (Figure 111, Figure 112). In Figure 109 and Figure 110 can be observed that the values of t_n and t_m at the crack initiation state are non-zero. In Figure 109 - Figure 112 are denoted turning points A (crack initiation), B (decrease in $\Delta\gamma_{xy}$ and reach of critical opening δ_{crit} in m direction) and C (end of loading path). It can be observed that the crack reaches its critical opening δ_{crit} in m direction and thus a sudden drop in stress occurs and the course of stress is not continuous.

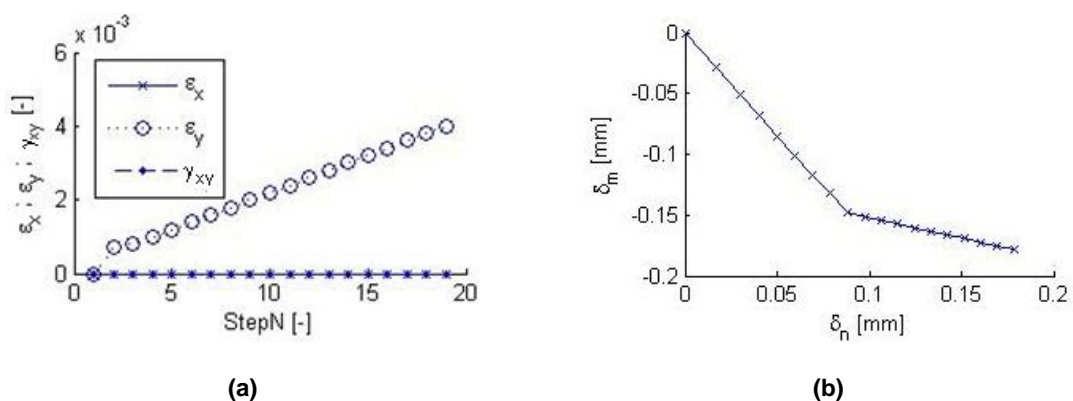


Figure 106 – LC CT2-2: Course of loading run by strain increments $\Delta\epsilon_x$, $\Delta\epsilon_y$, $\Delta\gamma_{xy}$ (a), development of crack opening δ_m with respect to δ_n (b)

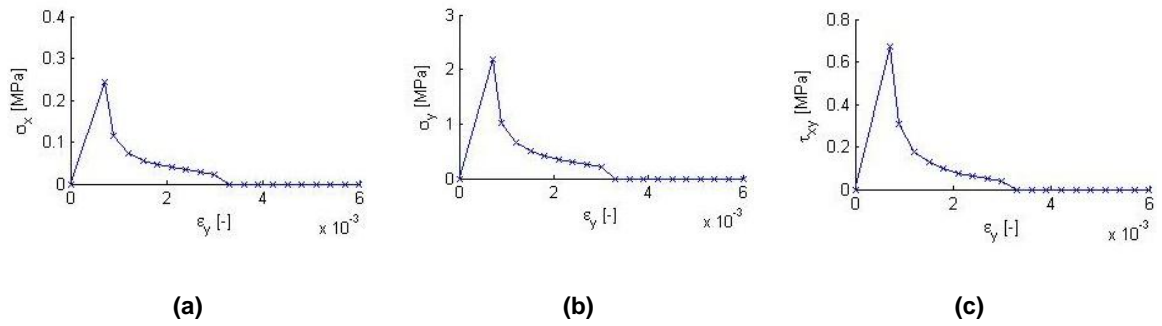


Figure 107 – LC CT2-2: Stress-strain curves $\sigma_x - \epsilon_y$ (a), $\sigma_y - \epsilon_y$ (b), $\tau_{xy} - \epsilon_y$ (c)

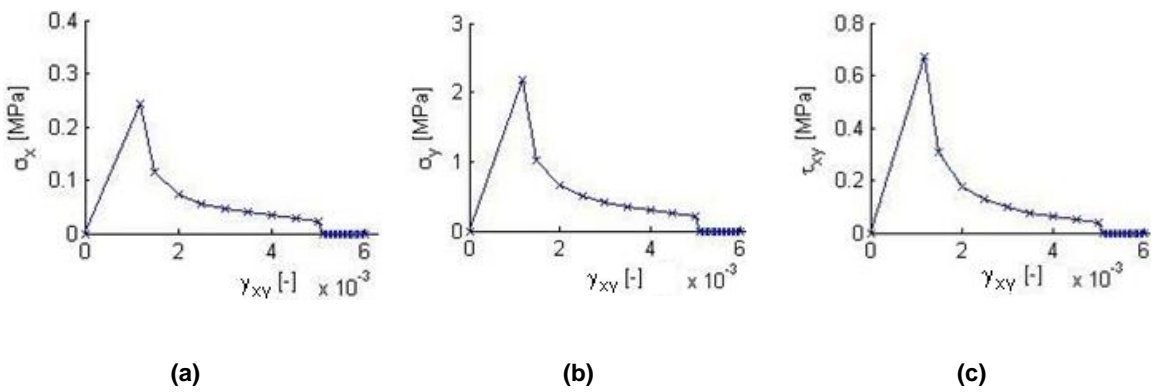


Figure 108 – LC CT2-2: Stress-strain curves $\sigma_x - \epsilon_{xy}$ (a), $\sigma_y - \epsilon_{xy}$ (b), $\tau_{xy} - \gamma_{xy}$ (c)

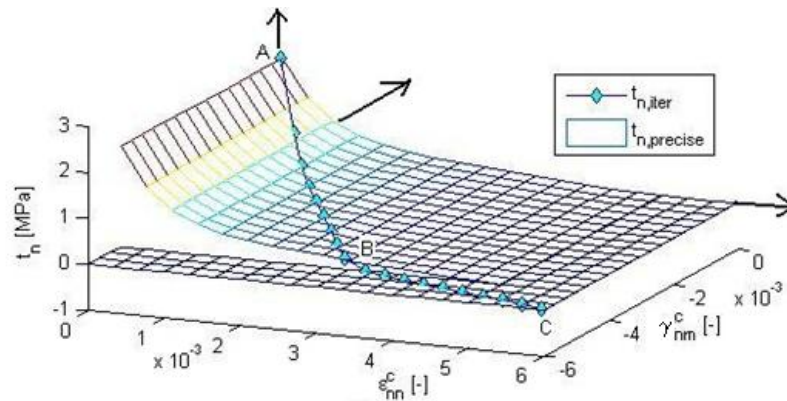


Figure 109 – LC CT2-2: Iterated normal traction $t_{n,iter}$ and normal traction function $t_n(\epsilon_{nn}^c)$ ($t_{n,precise}$)

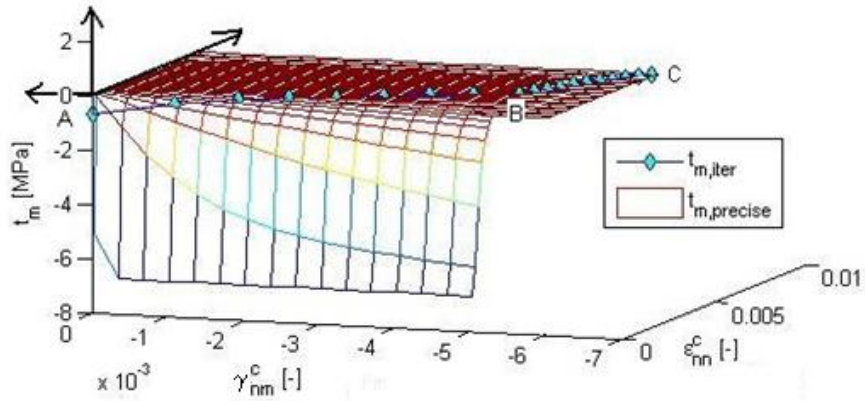


Figure 110 – LC CT2-2: Iterated shear traction $t_{m,iter}$, shear traction function $t_m(\epsilon_{nn}^c, \gamma_{nm}^c)$ ($t_{m,precise}$)

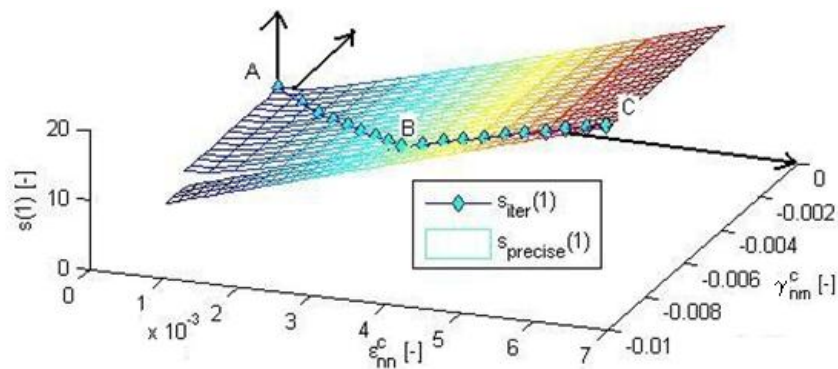


Figure 111 – LC CT2-2: Iteration function $s(1)$: iterated ($s_{iter}(1)$) and the precise function ($s_{precise}(1)$)

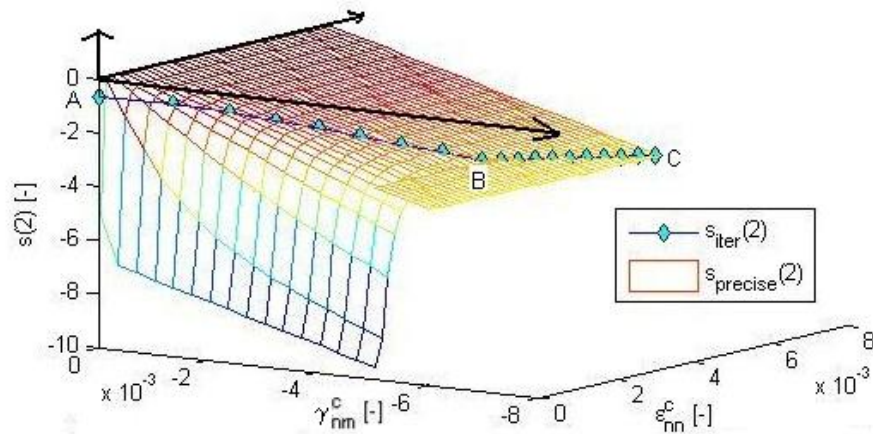


Figure 112 – LC CT2-2: Iteration function $s(2)$: iterated ($s_{iter}(2)$) and the precise function ($s_{precise}(2)$)

5.2.7 LC CT2-3: $\Delta\epsilon_y$ or $\pm\Delta\gamma_{xy}$, $\theta = 90^\circ$

LC CT2-3 prescribes strain increments $\Delta\epsilon_y^{1-2} = \Delta\epsilon_y^{13-14} = 4 \cdot 10^{-4}$, $\Delta\gamma_{xy}^{3-7} = \Delta\gamma_{xy}^{15-18} = 6 \cdot 10^{-4}$ and $\Delta\gamma_{xy}^{8-12} = -6 \cdot 10^{-4}$ (Figure 113a). Behavior of the material in LC CT2-3 is analogical to LC CT1-4. The difference consists in rotation between local and global coordinates. The results are plotted in Figure 113 - Figure 119.

Crack opens only in n direction if $\Delta\epsilon_y > 0$ and in m direction if $\Delta\epsilon_{xy} > 0$, see Figure 113b. Stress-strain curves are plotted in Figure 114 and Figure 115. It can be remarked that in Figure 115c is

shown how the shear stress τ_{xy} behaves for a certain level of crack opening δ_n . The less is the crack opened in n direction, the higher is the slope of $\tau_{xy} - \gamma_{xy}$ curve.

The course of the calculation is expressed by means of iterated components of traction vector t_n and t_m (Figure 116, Figure 117) and iterated values of iteration functions $s(1)$ and $s(2)$ (Figure 118, Figure 119). In Figure 116 - Figure 119 are denoted turning points A (crack initiation), B (end of $\Delta\varepsilon_y$, beginning of $+\Delta\gamma_{xy}$), C (beginning of $-\Delta\gamma_{xy}$), D (end of $-\Delta\gamma_{xy}$, beginning of $\Delta\varepsilon_y$), E (end of $\Delta\varepsilon_y$, beginning of $+\Delta\gamma_{xy}$) and F (end of loading path).

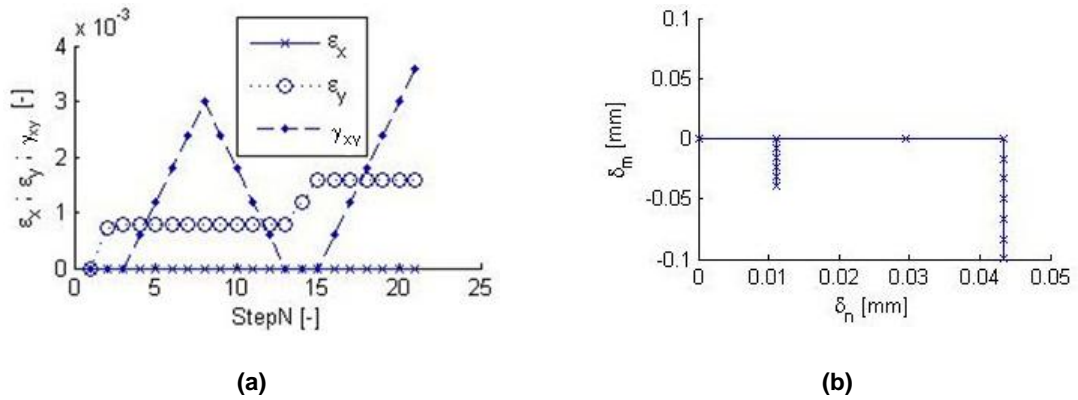


Figure 113 – LC CT2-3: Course of loading run by strain increments $\Delta\varepsilon_x$, $\Delta\varepsilon_y$, $\Delta\gamma_{xy}$ (a), development of crack opening δ_m with respect to δ_n (b)

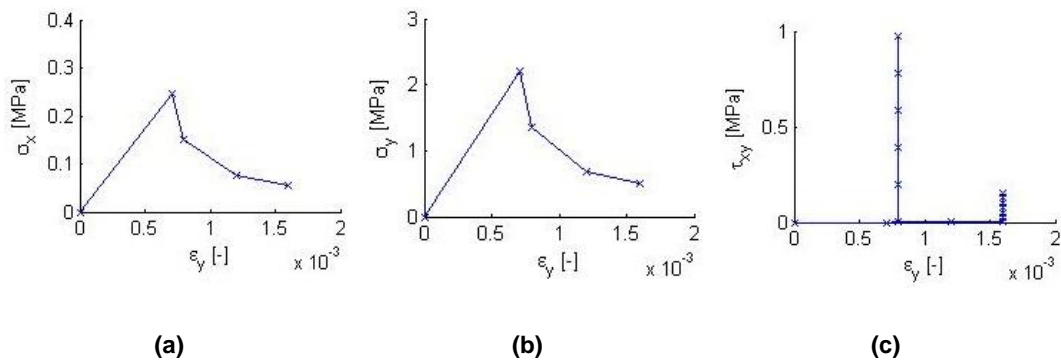


Figure 114 – LC CT2-3: Stress-strain curves $\sigma_x - \varepsilon_y$ (a), $\sigma_y - \varepsilon_y$ (b), $\tau_{xy} - \varepsilon_y$ (c)

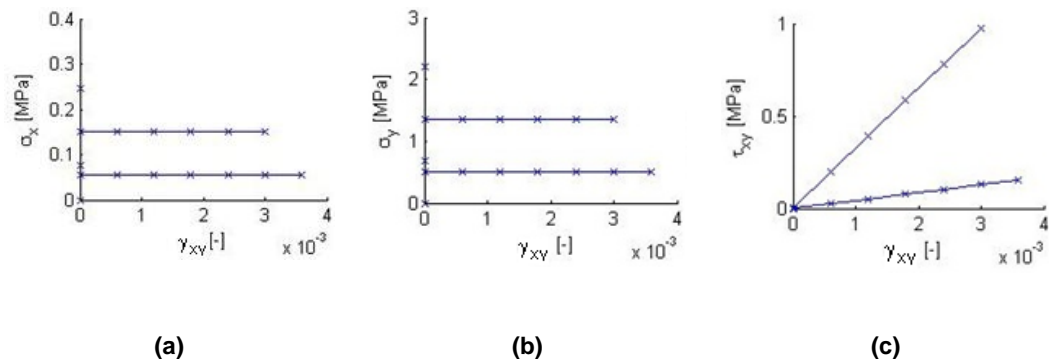


Figure 115 – LC CT2-3: Stress-strain curves $\sigma_x - \gamma_{xy}$ (a), $\sigma_y - \gamma_{xy}$ (b), $\tau_{xy} - \gamma_{xy}$ (c)

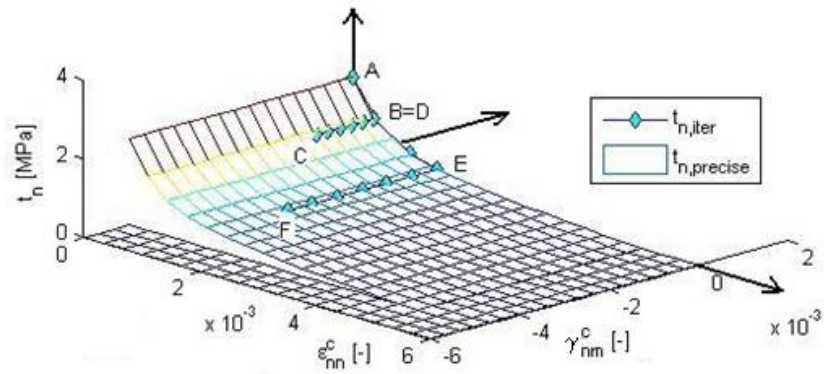


Figure 116 – LC CT2-3: Iterated normal traction $t_{n,iter}$ and normal traction function $t_n(\epsilon_{nn}^c)$ ($t_{n,precise}$)

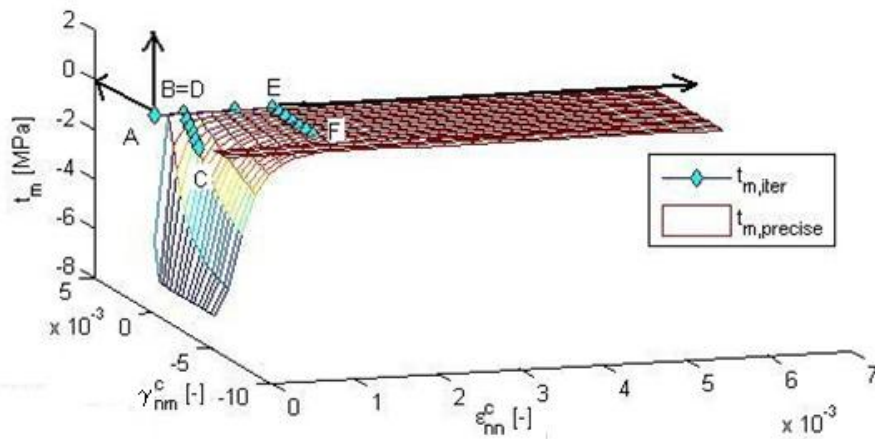


Figure 117 – LC CT2-3: Iterated shear traction $t_{m,iter}$, shear traction function $t_m(\epsilon_{nn}^c, \gamma_{nm}^c)$ ($t_{m,precise}$)

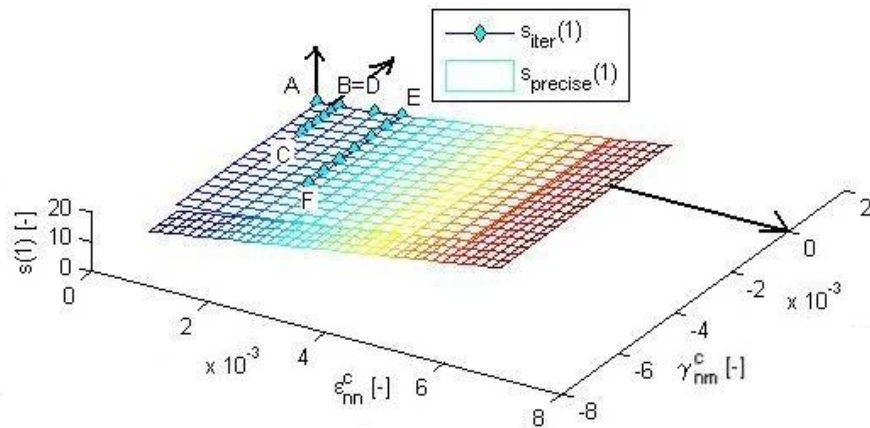


Figure 118 – LC CT2-3: Iteration function $s(1)$: iterated ($s_{iter}(1)$) and the precise function ($s_{precise}(1)$)

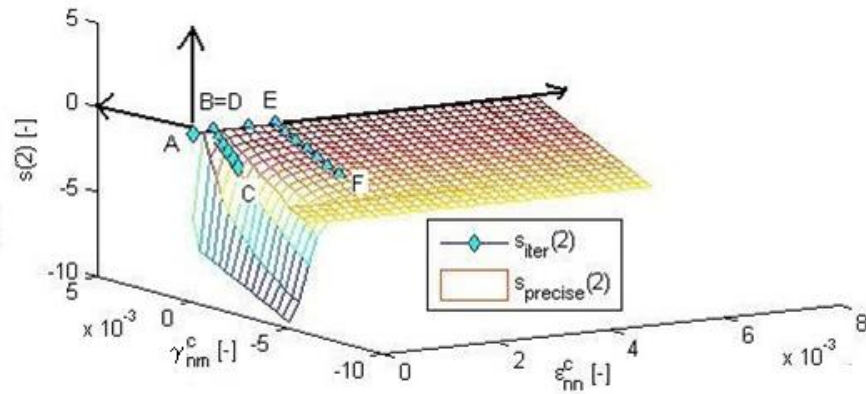


Figure 119 – LC CT2-3: Iteration function $s(2)$: iterated ($s_{iter}(2)$) and the precise function ($s_{precise}(2)$)

5.2.8 LC CT2-4: $\Delta\gamma_{xy}$, $\theta = 90^\circ$ (pure shear)

Load case CT2-4 prescribes only positive shear strain increments $\Delta\gamma_{xy}^{1-3} = 4 \cdot 10^{-3}$ for steps 1-3 and $\Delta\gamma_{xy}^{4-20} = 3 \cdot 10^{-3}$ for steps 4-20 (Figure 120a). Behavior of the material under shear is in this model considered as non-linear elastic. It is assumed that after crack initiation, the remaining bridging fibers do not behave in the manner of sliding friction but in a non-linear elastic way. This assumption seems to be suitable for CT1 while for CT2 less because in case of crack parallel to grain, there is less amount of bridging fibers as the fibers run in parallel. The results are plotted in Figure 120 - Figure 125.

Crack opens (slides) in m direction as $\Delta\gamma_{xy} > 0$, see Figure 120b. Stress-strain curves are plotted in Figure 121 where is shown that with growing shear strain $\Delta\gamma_{xy} > 0$ is non-zero only shear stress that keeps constant after reaching shear capacity f_s .

Course of the calculation is expressed by means of iterated components of traction vector t_n and t_m (Figure 122 and Figure 123, respectively) and iterated values of iteration functions $s(1)$ and $s(2)$ (Figure 124, Figure 125). In Figure 122 - Figure 125 are denoted turning points A (crack initiation), B (reach of critical crack opening δ_{crit} in m direction) and C (end of loading path). It can be remarked that the function $t_n(\varepsilon_{nn}^c)$ is in this case zero because the value of normal traction at crack initiation is zero ($t_{n,ci} = 0$).

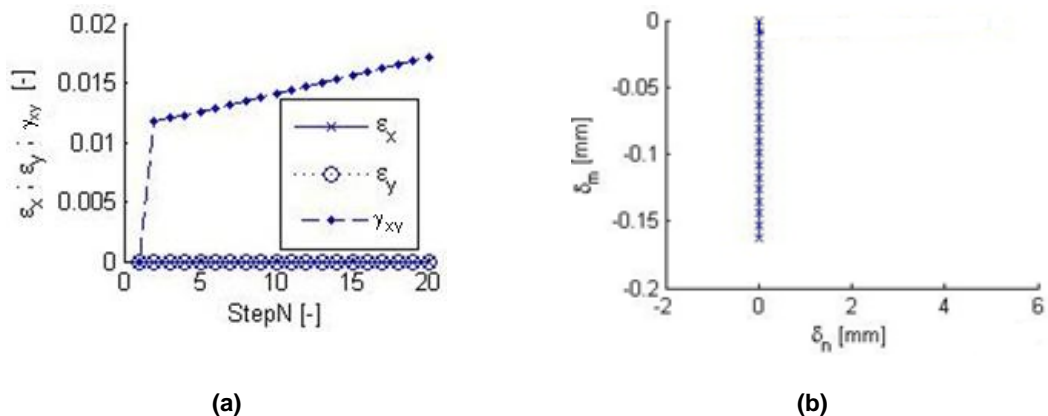


Figure 120 – LC CT2-4: Course of loading run by strain increments $\Delta\varepsilon_x$, $\Delta\varepsilon_y$, $\Delta\gamma_{xy}$ (a), development of crack opening δ_m with respect to δ_n (b)

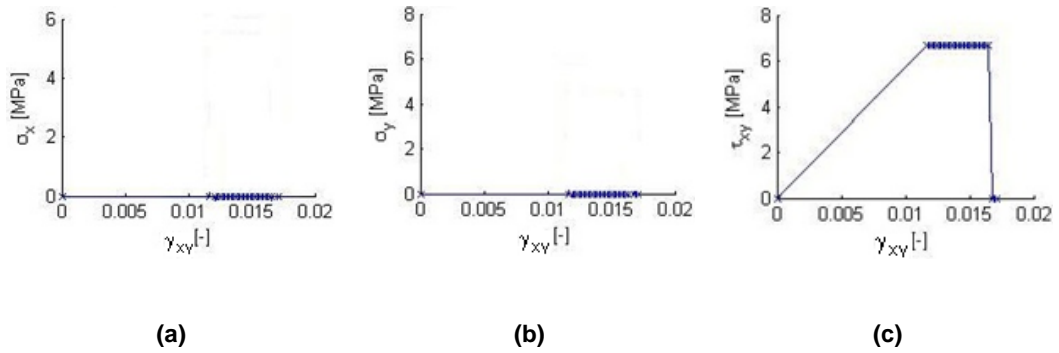


Figure 121 – LC CT2-4: Stress-strain curves $\sigma_x - \gamma_{xy}$ (a), $\sigma_y - \gamma_{xy}$ (b), $\tau_{xy} - \gamma_{xy}$ (c)

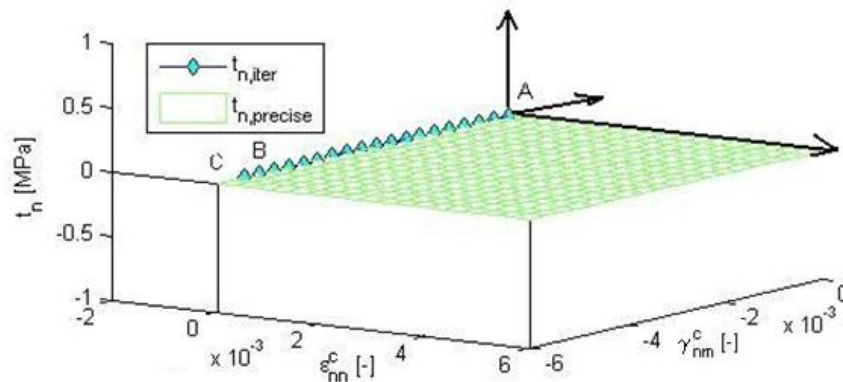


Figure 122 – LC CT2-4: Iterated normal traction $t_{n,iter}$ and normal traction function $t_n(\epsilon_{nn}^c)$ ($t_{n,precise}$)

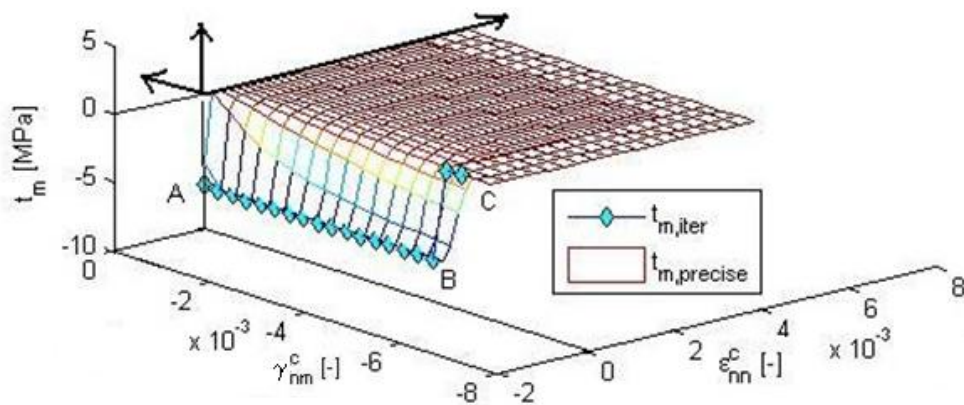


Figure 123 – LC CT2-4: Iterated shear traction $t_{m,iter}$, shear traction function $t_m(\epsilon_{nn}^c, \gamma_{nm}^c)$ ($t_{m,precise}$)

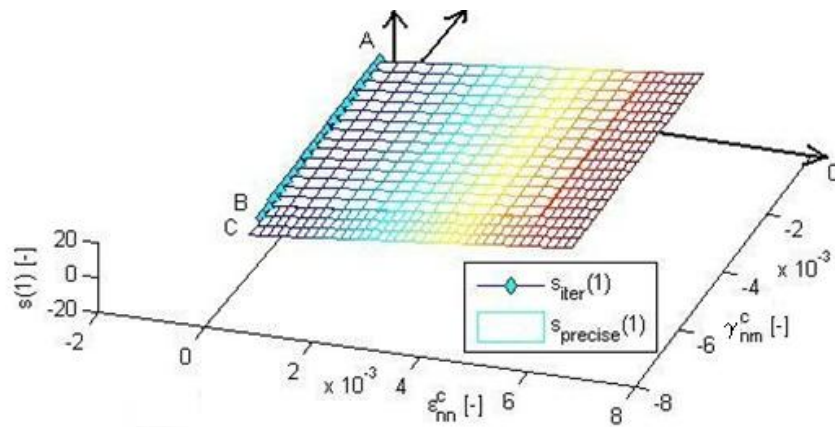


Figure 124 – LC CT2-4: Iteration function $s(1)$: iterated ($s_{iter}(1)$) and the precise function ($s_{precise}(1)$)

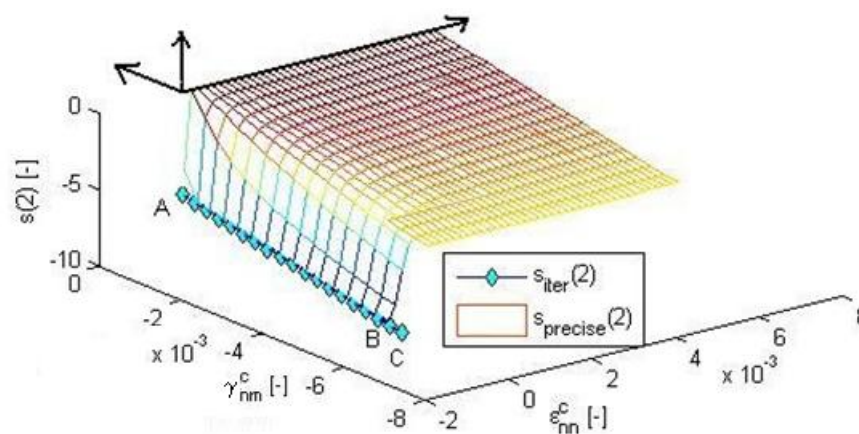


Figure 125 – LC CT2-4: Iteration function $s(2)$: iterated ($s_{iter}(2)$) and the precise function ($s_{precise}(2)$)

5.3 Model performance during unloading/reloading cycle

An example of results for unloading/reloading path (LC UNL) is presented in the following text. This Load case prescribes strain increment $\Delta\epsilon_x^1 = 5 \cdot 10^{-3}$ for the step 1, $\Delta\epsilon_x^{2-5} = \Delta\epsilon_x^{10-13} = 2 \cdot 10^{-3}$, $\Delta\epsilon_x^{17-20} = -2 \cdot 10^{-3}$ and $\Delta\gamma_{xy}^{14-20} = 4 \cdot 10^{-4}$ (Figure 126a). The results are plotted in Figure 126 - Figure 131.

Crack opens and close in n direction if $\Delta\epsilon_y > 0$ or $\Delta\epsilon_y < 0$, respectively, and in m direction if $\Delta\gamma_{xy} > 0$, see Figure 126b. Stress-strain curves are plotted in Figure 127. It can be remarked that in Figure 127a and Figure 127b is shown the unloading cycle path as a line edging to the origin of coordinates.

Course of the calculation is expressed by means of iterated components of traction vector t_n and t_m (Figure 128, Figure 129) and iterated values of iteration functions $s(1)$ and $s(2)$ (Figure 130, Figure 131). In Figure 128 is displayed the unloading function for n direction $t_{n,UNL}$. In Figure 128 - Figure 131 are denoted turning points A (crack initiation), B (beginning of unloading cycle with $-\Delta\epsilon_{nn}^c$), C (the middle of unloading cycle, beginning of $+\Delta\epsilon_{nn}^c$), D (the end of unloading cycle, beginning of $+\Delta\epsilon_{xy}$), E (beginning of $+\Delta\epsilon_x$ and $+\Delta\epsilon_{xy}$) and F (end of the loading path).

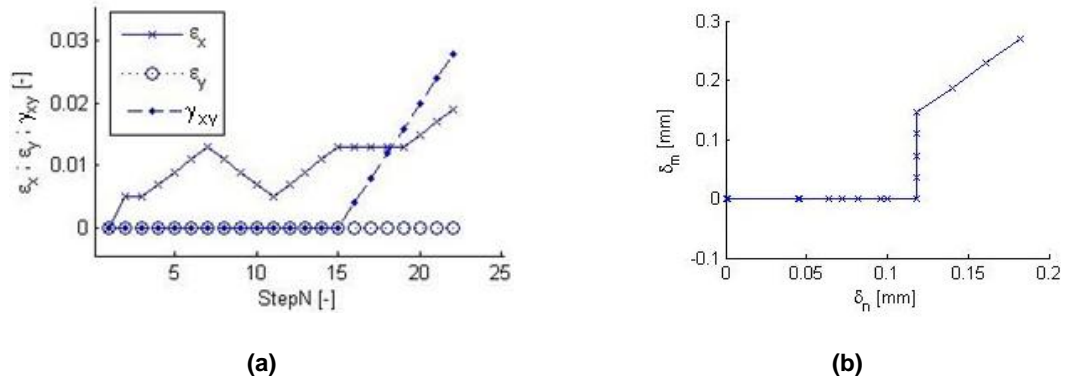


Figure 126 – LC UNL: Course of loading run by strain increments $\Delta\varepsilon_x$, $\Delta\varepsilon_y$, $\Delta\gamma_{xy}$ (a), development of crack opening δ_m with respect to δ_n (b)

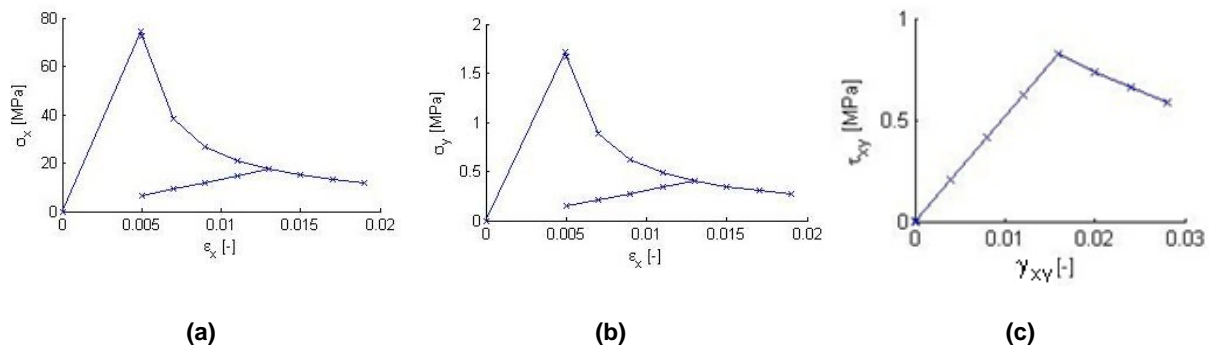


Figure 127 – LC UNL: Stress-strain curves $\sigma_x - \varepsilon_x$ (a), $\sigma_y - \varepsilon_x$ (b), $\tau_{xy} - \gamma_{xy}$ (c)

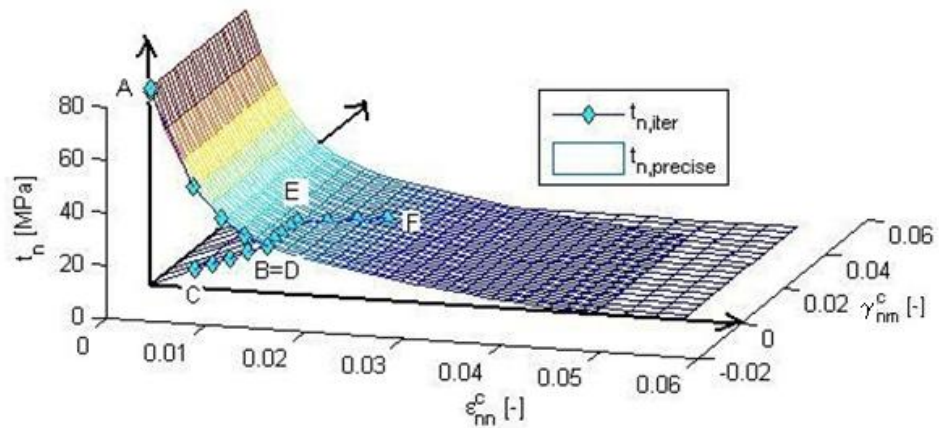


Figure 128 – LC UNL: Iterated normal traction $t_{n,iter}$ and normal traction function $t_n(\varepsilon_{nn}^c)$ ($t_{n,precise}$)

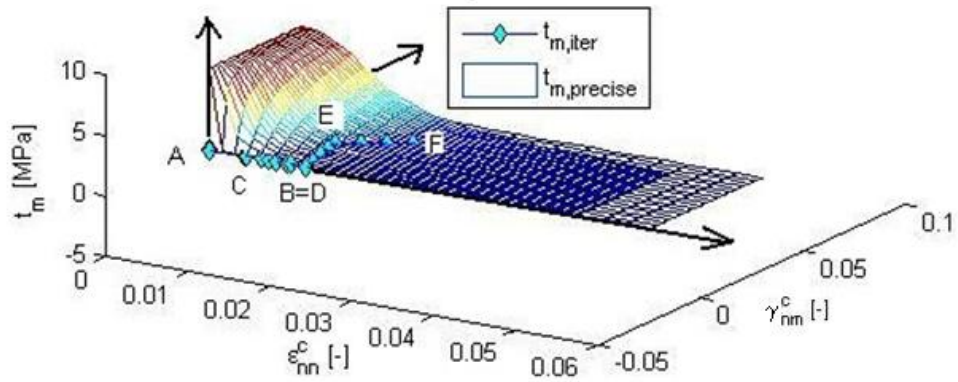


Figure 129 – LC UNL: Iterated shear traction $t_{m,iter}$, shear traction function $t_m(\epsilon_{nn}^c, \gamma_{nm}^c)$ ($t_{m,precise}$)

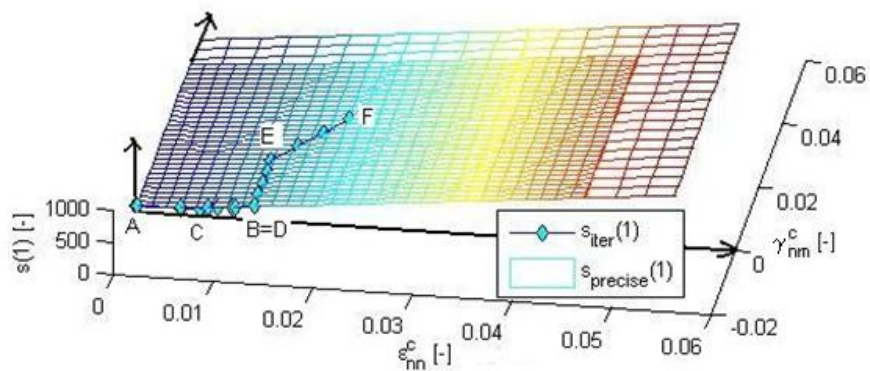


Figure 130 – LC UNL: Iteration function $s(1)$: iterated ($s_{iter}(1)$) and the precise function ($s_{precise}(1)$)

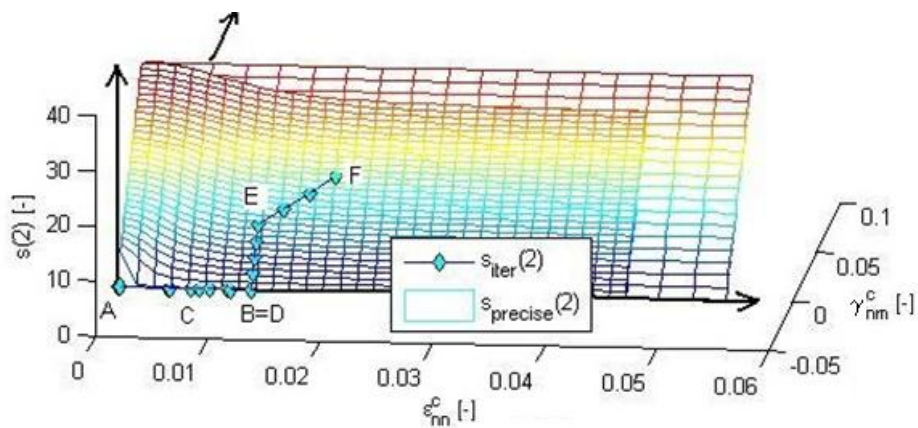


Figure 131 – LC UNL: Iteration function $s(2)$: iterated ($s_{iter}(2)$) and the precise function ($s_{precise}(2)$)

6. Conclusion

This thesis has fulfilled its objectives. First, a summary of typical wood behavior and characteristics was provided. Second, an overview of current timber models was given together with a brief discussion on their applicability to the model developed in this work. Third, a two-dimensional homogeneous constitutive model of timber fracturing under tensile and shear loads was implemented in a MATLAB[®] computer code, verified and the model performance was demonstrated for various load cases with isotropic and orthotropic material properties and also for an unloading/reloading cycle.

In the proposed constitutive model, we idealize timber as a quasi-brittle material. Thus, we consider the material as a continuum with discontinuities (cracks). The continuous part is characterized by elastic orthotropic stress-strain law while traction-separation law describes the behavior of the discontinuities (cracks). Fixed smeared crack model is used to represent the fracture. Prior to cracking, wood obeys the rules of orthotropic elasticity. The proposed model considers only one initiated crack in material at the same time and small deformations (lower than 0.05ε).

A crack is initiated if failure criterion is fulfilled. Whether a crack forms across (crack type 1) or along the grain (crack type CT2) is decided based on threshold angle between the grain direction and the principal stress direction. This angle is considered as a material parameter. Crack across the grain is perpendicular to the principal stress direction while the crack along the grain keeps parallel to the fibers irrespective of the principal stress direction. Consequently, at the crack initiation state, the crack type CT1 is exposed only to normal traction while the crack type CT2 can be exposed both to normal and tangential traction. After crack initiation, as the fixed crack model is used, the direction of the crack (CT1 or CT2) is frozen and since the principal stress axes can rotate, both normal and shear tractions may subsequently arise on the crack.

Traction-separation law defining the behavior of the initiated crack is softening in normal direction to the crack ($t_n(\varepsilon_{nn}^c)$). In tangential direction, traction-separation law $t_m(\varepsilon_{nn}^c, \gamma_{nm}^c)$ is proposed using an arctangential function that fulfills the following assumptions: (i) the maximal value of shear traction t_m never exceeds shear strength f_s ($t_m < f_s$), (ii) the function of $t_m(\varepsilon_{nn}^c, \gamma_{nm}^c)$ can take the value of $t_m \in [0, f_s)$ at the crack initiation state. Thus, traction separation law in both local directions (n, m) ensures a smooth transition from the stress state on the failure surface to the proposed cracking cohesive relationship.

Traction-separation law is limited in both local directions by critical crack opening (δ_{crit}). If the value of δ_{crit} is trespassed in n direction, both components of traction vector (t_n, t_m) continuously reach zero. If the same happens in m direction for normal crack opening (δ_n) lower than the critical value ($\delta_n < \delta_{crit}$), both components of traction vector suddenly drop to zero.

On account of the developed model performance demonstrated for various load cases, the model is consistent with expected timber behavior.

Suggestions for future work are as follows:

- The developed 2D constitutive model should be validated more thoroughly against experimental data. This might involve a need for additional specialized experiments.
- An enhancement of the model developed in this work to three-dimensional space can be carried out.
- The developed model can be extended for arbitrary loading (tension, shear, and compression).

- The input functions of cohesive law or failure surface can be improved based on available experimental data.
- After full implementation into a finite element code, this model can be used as a basis for the following advanced analysis approaches to timber:
 - A model that can account for the presence of inhomogeneities such as knots. For this purpose, the present model would be used to represent clear timber while the inhomogeneities would be modeled as discrete regions with different properties.
 - A model that can take into account an influence of moisture (wood drying, moisture induced stresses), which would be assigned as initial stress or eigen-strain. To this end, the moisture distribution would have to be analyzed separately using suitable transport model.

REFERENCES

- Anderson, T., L., 2005, *Fracture Mechanics - Fundamentals and Applications*, ISBN 978-1-4200-5821-5 (eBook - PDF).
- ASTM D143 – 94, *Standard Methods of Testing – Small Clear specimens of Timber*, ASTM – The American Society for Testing and Materials, United States.
- ASTM Standard E399, *Plain-Strain Fracture Toughness of Metallic Materials*, American Society for Testing and Materials, Philadelphia.
- Bartůňková, E., 2010, *Non-destructive Tests and Degradation Assessment of Old Chestnut Timber*, Master's Thesis, Universidade do Minho, Portugal.
- Bodig, J., Jayne, B., A., 1982, *Mechanics of wood and wood composites*. New York: Van Nostrand Reinhold.
- Bostrom, L., 1992, *Method for determination of the softening behaviour of wood and the applicability of a nonlinear fracture mechanics model*, Doctoral Thesis, Report TVBM-1012, Lund, Sweden.
- Červenka, J., Papanikolaou, V., K., 2008, *Three dimensional combined fracture–plastic material model for concrete*, *International Journal of Plasticity*, vol. 24, no. 12, pp. 2192–2220.
- ČSN EN 338:2010, *Konstrukční dřevo - Třídy pevnosti*, Česká technická norma.
- Daudeville, L., 1999, *Fracture in spruce: experiment and numerical analysis by linear and nonlinear fracture mechanics*, *Holz als Roh- und Werkstoff* 57 (1999) 425±432 Ó Springer-Verlag 1999.
- deSouza Neto, E., A., Peric, D., Owen, D., R., J., 1995, *Finite strain implementation of an elastoplastic model for crushable foam*. In: Wiberg N-E, editor, *Advances in finite element technology*, Barcelona: CIMNE.
- Dinwoodie, J., M., 1981, *Timber, Its Nature and Behaviour*, New York, ISBN 0-419-25550-8.
- EN 408:2003, *Timber structures - Structural timber and glued laminated timber – Determination of some physical and mechanical properties*, CEN – European Committee for Standardization.
- Feenstra, P., H., 1993, *Computational aspects of biaxial stress in plain and reinforced concrete*, Dissertation, Delft University of Technology, Delft, The Netherlands.
- Feio, A., O., 2005, *Inspection and diagnosis of Historical Timber Structures: NDT correlations and structural behaviour*, Ph.D. thesis - Universidade do Minho, Guimaraes, 2005, 208 pp.
- Fonselius, M., Riipola, K., 1992, *Determination of Fracture Toughness for Wood*, *J. Struct. Eng.*, 118(7), 1727–1740.
- Fortino, S., Mirianon, F., Toratti, T., 2009, *A 3D moisture-stress FEM analysis for time dependent problems in timber structures*, *Mech Time-Depend Mater* 2009, 13(4):333–56.
- Fragiacomo, M., Fortino, S., Tononi, D., Usardi, I., Toratti, T., 2011, *Moisture-induced stresses perpendicular to grain in cross-sections of timber members exposed to different climates*, *Engineering Structures* 33 (2011) 3071–3078.
- Frangi, A., Fontana, M., Hugi, E., Jobstl, R., 2009, *Experimental analysis of cross-laminated timber panels in fire*, *Fire Safety Journal* 44 (2009) 1078–1087.

- Gibson, L., J., Ashby, M., F., 1988, Cellular solids, Structure and Properties, Oxford: Pergamon.
- Glass, S., V., Zelinka, S., L., 2010, Moisture Relations and Physical Properties of Wood, Chapter 4, Wood handbook - Wood as an engineering material, General Technical Report FPL-GTR-190, Madison, WI: U.S., Department of Agriculture, Forest Service, Forest Products Laboratory, 508 p.
- Gliniorz, K-U., Mosalam, K., M., Natterer, J., 2002, Modeling of layered timber beams and ribbed shell frameworks, Composites: Part B 33 (2002) 367-381.
- Guan, Z., W., Zhu, E., C., Finite element modelling of anisotropic elasto-plastic timber composite beams with openings, Engineering Structures 31 (2009) 294-403.
- Häglund, M., 2009, Parameter influence on moisture induced eigen-stresses in timber, Eur. J. Wood Prod. (2010) 68:397–406, Springer-Verlag 2009.
- Holmberg, S., 1997, Deformation and fracture of wood in initial defibration process. Report TVSM-3019, Lund University, Sweden.
- Holmberg, S., Persson, K., Petersson, H., 1998, Nonlinear mechanical behaviour and analysis of wood and fibre materials, Division of Structural Mechanics, Lund University, Lund, Sweden.
- Hordijk, D., A., 1991, Local approach to fatigue of concrete, PhD thesis, Delft University of Technology, Delft, The Netherlands.
- Jirásek, M., 2012, Modelling of localized inelastic deformation, lecture notes, CTU in Prague.
- JCSS Probabilistic model code, 2006, Part 3: Resistance models, JCSS – Joint comitee on Structural Safety.
- JIS, Japanese Industrial Standard, 1998, Testing method for interlaminar fracture toughness of carbon fibre reinforced plastics JIS K7086-93, Japanese Standards Association, Tokyo.
- Kretschmann, D., E., 2010, Mechanical Properties of Wood, Chapter 5, Wood handbook - Wood as an engineering material, General Technical Report FPL-GTR-190, Madison, WI: U.S., Department of Agriculture, Forest Service, Forest Products Laboratory, 508 p.
- Kroflíč, A., Planinc, I., Saje, M., Turk, G., Čas, B., 2010, Non-linear analysis of two-layer timber beams considering interlayer slip and uplift, Engineering Structures 32 (2010) 1617_1630.
- Kuklík, P., 2008, Fire Resistance of Timber Structures, Handbook 1 – Timber Structures, Chapter 17, Leonardo da Vinci Pilot Project, CZ/06/B/F/PP/168007, Educational Materials for Designing and Testing of Timber Structures – TEMENTIS.
- Lamb, F., M., 1992, Splits and cracks in wood, Virginia Tech, Blacksburg, Virginia, <http://ir.library.oregonstate.edu/xmlui/handle/1957/5302> [available in September 2012].
- Larsen, H., J., Gustafsson, P., J., 1989, Design of end-notched beams, 22th CIB-W18 A meeting, Berlin Germany, Paper 22-10-1.
- Lourenço, P., B., de Borts, R., Rots, J., G., 1997, A plane stress softening plasticity model for orthotropic materials, Int. J. Numer. Meth. Engng., 40, 4033-4057.
- NBR 7190:1997, Brazilian norm, Projeto de estruturas de madeira, ABNT - Associação Brasileira de normas técnicas.
- Oemarsson, S., Dahlblom, O., Johansson, M., 2009, Finite element study of growth stress formation in wood related to distorsion of sawn timber, Wood Sci Technol (2009) 43:387-403.

- Oudjene, M., Khelifa, M., 2009, Finite element modelling of wooden structures at large deformations and brittle failure prediction, *Materials and Design*, Nancy-Universite, Laboratoire d'Etudes et de Recherche sur le Matériau Bois.
- Persson, K., 1997, Modelling of wood properties by a micromechanical approach, Report TVSM-3020, Lund University, Sweden.
- Požgaj, A., Chovanec, D., Kurjatko, S., Babiak, M., 1993, Štruktúra a vlastnosti dreva, *Príroda*, a.s. Bratislava.
- Reinhardt H., W., Cornelissen, H., A., W., Hordijk, D., A., 1986, Tensile tests and failure analysis of concrete. *Journal of Structural Engineering*, ASCE, 112:2462–2477.
- Reiterer, A., Sinn, G., Stanzl-Tschegg, S., E., 2002, Fracture characteristics of different wood species under mode I loading perpendicular to the grain. *Mater Sci Eng A332*:29–36.
- Roylance, D., 2001, Introduction to Fracture Mechanics, Department of Materials Science and Engineering, Massachusetts Institute of Technology, Cambridge, MA 02139.
- Samarasinghe, S., 1999, Fracture Toughness of Wood Based on Experimental Near-Tip Displacement Fields and Orthotropic theory, *Proceedings of the International Wood Engineering Conference*, Rotorua, New Zealand.
- Serrano, E., Gustafsson, P., J., 2006, Fracture mechanics in timber engineering – Strength analyses of components and joints. *Materials and Structures (2006)* 40:87-96.
- Sousa, H., 2012, Methodologies for Safety Assessment of Existing Timber Structures, University of Minho, Department of Civil Engineering, Portugal (work in progress).
- Turner, I., W., 1996, A two-dimensional orthotropic model for simulating wood drying processes, *Appl. Math. Modelling* 1996, Vol. 20, January.
- UNI 11035-2:2003, Legno strutturale – Regole per la classificazione a vista secondo la resistenza e i valori caratteristici per tipi di legname strutturale italiani, UNI – Ente Nazionale Italiano di Unificazione.
- Vasic, S., Smith, I., 2001, Bridging crack model for fracture of spruce, *Engineering Fracture Mechanics* 69 (2002) 745-760.
- Wiedenhoeft, A., 2010, Structure and Function of Wood, Chapter 3, *Wood handbook - Wood as an engineering material*, General Technical Report FPL-GTR-190, Madison, WI: U.S., Department of Agriculture, Forest Service, Forest Products Laboratory, 508 p.
- Yoshihara, H., Kawamura, T., 2005, Mode I fracture toughness estimation of wood by DCB test, Faculty of Science and Engineering, Shimane University, Nishikawazu-cho 1060, Matsue, Shimane 690-8504, Japan

APPENDIX 1: Tension test parallel to grain of chestnut timber

Appendix 1 is literally adopted from Bartůňková (2010). It describes tension test parallel to grain of hundred year old chestnut timber. The raw measured data were provided by Sousa (2012).

Tension test is a destructive method used to determine modulus of elasticity (MoE) in tension parallel to grain $E_{t,0}$ and tensile strength parallel to grain $f_{t,0}$. The bending test was performed according to European norm EN 408:2003 (Timber structures - Structural timber and glued laminated timber - Determination of some physical and mechanical properties) except for the time of failure that was considered with respect to the procedures.

Specimens

After completion of the bending test, two specimens were cut from each left, central and right part (L, C, R) of every bending specimen (A – T) except for the bending specimens H, L, P, T from which was cut only one specimen for each left, central and right part of the beam. There were made 108 tension specimens. The dimensions of the specimens were adapted from the Brazilian norm NBR 7190:1997 (Figure 132).

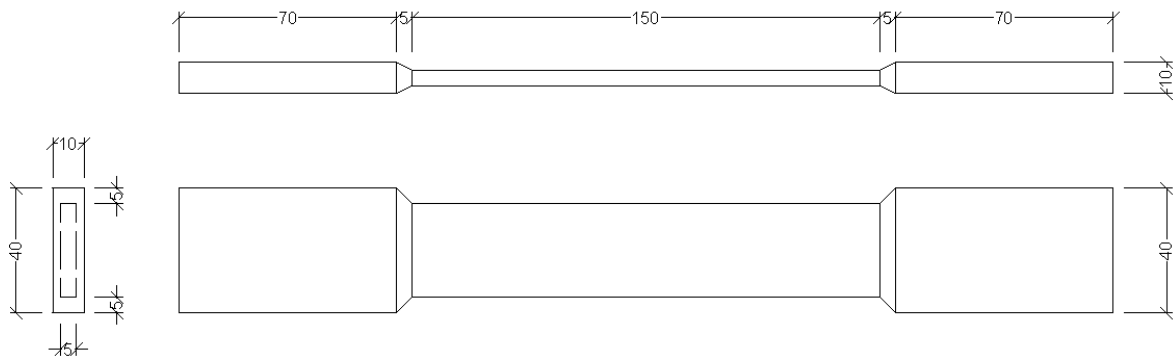


Figure 132 – Tension specimen design (dimensions in mm)

Test set up

The test piece was supported using gripping devices which permitted as far as possible the application of a tensile load without inducing bending. The test was run by displacement control of the rate of 1 to 2 mm/min with respect to a visual assessment of the specimen tension resistance regarding the existence of defects. The loading equipment used was capable of measuring the load to the required accuracy of 1% of the load applied. Deformation was measured clip-on extensometer (Figure 133) over a length of five times the width of the piece, located five times the width to the ends of the grips. The tension test performance is presented in Figure 134.

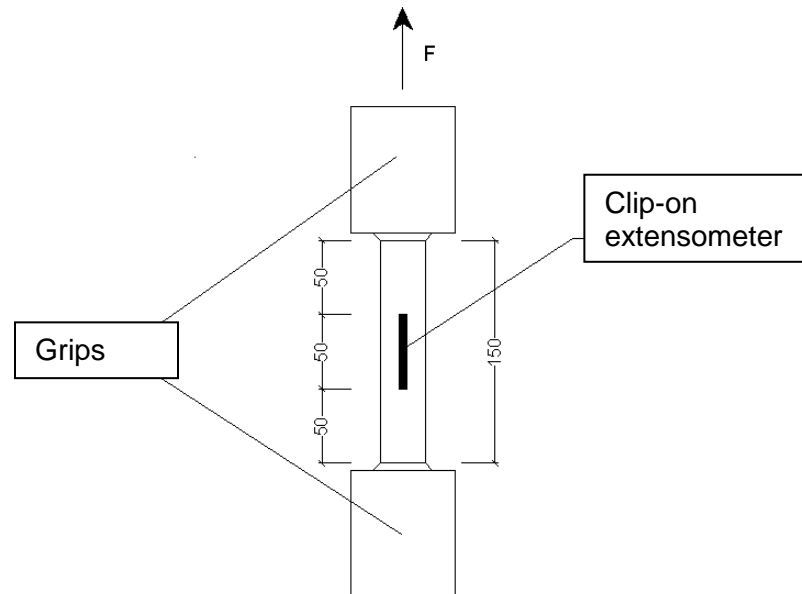


Figure 133 – Scheme of the clip-on extensometer position on the tension specimen

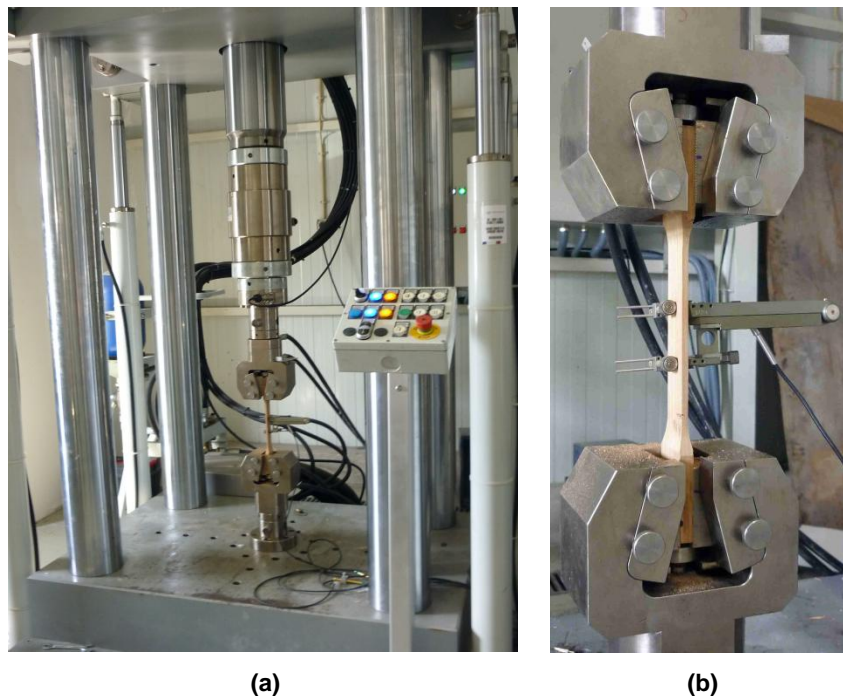


Figure 134 – Tension test: (a) overall arrangement, (b) detail of a specimen in grips

Modulus of elasticity in tension parallel to grain ($E_{t,0}$)

MoE in tension parallel to grain $E_{t,0}$ [N/mm²] is given by the equation as follows:

$$E_{t,0} = \frac{l_1(F_2 - F_1)}{A(w_2 - w_1)} \quad [86]$$

where l_1 is gauge length [mm] for the determination of MoE, A is cross-sectional area [mm²], $(F_2 - F_1)$ is an increment of load [N] on the straight line portion of the load deformation curve, $(w_2 - w_1)$ is an increment of deformation [mm] corresponding to $(F_2 - F_1)$.

MoE in tension parallel to grain $E_{t,0}$ for each specimen was calculated according to Eq. [86]. Precise cross-sectional dimensions in the middle of the specimens were measured by use of an electronic caliper. Maximum load (F_{max}) together with clip and grip displacement were obtained from the tension test procedure. Increments of load and deformation were calculated on the basis of the load vs deformation linear regression where the square of the correlation coefficient was $R^2 \geq 0.99$. The linear regression was performed within an interval of $(0.1 - 0.4) F_{max}$ of the load vs. displacement curve. An example of the linear regression is shown in **Figure 135** for the tension specimen A_{c1} .

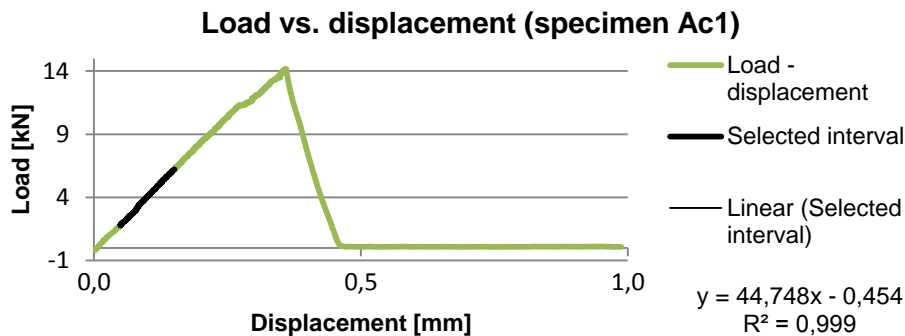


Figure 135 - Load vs. (clip gauge) displacement for the specimen A_{c1}

Tensile strength parallel to grain ($f_{t,0}$)

Tensile strength parallel to grain $f_{t,0}$ [N/mm^2] is given by the expression as follows

$$f_{t,0} = \frac{F_{max}}{A} \quad [87]$$

where F_{max} is maximum load [N], A is cross-sectional area [mm^2]. Tensile strength parallel to grain $f_{t,0}$ was calculated according to Eq. [87] for each tension specimen.

Failure modes

The mode of failure at the fracture section of each test piece was reported. The fracture modes considered were distinguished according to the failure localization or presence of the nodes as follows

- failure in the grip,
- failure due to the presence of a nod,
- failure in the middle thinner part of the tension specimen in the form of splinter, shear, tension failure mode or their combinations (**Figure 16**).

Examples of the failure modes recognized in the tension specimens in test campaign are shown in **Figure 136**.



Figure 136 – Examples of tension specimens failed in split (a), shear (b) and tension (c)

The specimens where occurred failure in the grip or failure due to the presence of a nod were not included in the calculation of the resulting $E_{t,0}$ and $f_{t,0}$. The coefficients of variation (CoV) of $E_{t,0}$ and $f_{t,0}$ for all the tension specimens (CoV_{all}) and for the specimens selected with respect to the failure mode ($\text{CoV}_{\text{selected}}$) are presented in **Table 7**. The CoV did not change or decrease with the selection of the tension specimens, especially considering the stiffness parameters in linear elastic range. Nevertheless, the CoV are equal or lower than the CoV of $E_{t,0}$ and $f_{t,0}$ ($\text{CoV} [E_{t,0}] = \text{CoV} [E_m] = 0.13$ and $\text{CoV} [f_{t,0}] = 0.30$) of Nordic softwood suggested by the JCSS Probabilistic model code (2006).

Table 7 – Coefficients of variation of $E_{t,0}$ and $f_{t,0}$ for all the specimens and for the selected specimens

	CoV_{all}	$\text{CoV}_{\text{selected}}$
$E_{t,0}$	0.13	0.13
$f_{t,0}$	0.27	0.25

Results

Results obtained from the tension test ($E_{t,0}$ and $f_{t,0}$) are shown in **Table 8**. Mean values of $E_{t,0}$ and $f_{t,0}$ for all specimens sorted according to the failure type are shown in **Table 9** where failure due to node shows significantly lower strength values than other modes and the values of $E_{t,0}$ do not much differ across the failure types.

Table 8 – Tension test results for each beam A – T: $E_{t,0}$, $f_{t,0}$ [N/mm²]

	A	B	C	D	E	F	G	H	I	J
Mean $E_{t,0}$	14 427	14 374	13 509	10 888	11 907	13 735	12 726	14 735	14 033	13 359
CoV	0.11	0.02	0.03	0.07	0.14	0.09	0.05	-	0.01	0.14
Mean $f_{t,0}$	87	68	90	62	57	79	70	65	88	82
CoV	0.15	0.25	0.03	0.27	0.48	0.21	0.10	-	0.07	0.29
	K	L	M	N	O	P	Q	R	S	T
Mean $E_{t,0}$	15 198	12 666	11 569	13 785	12 829	12 673	13 204	11 179	13 978	8 372
CoV	0.11	-	0.05	0.07	0.07	0.17	0.07	0.03	0.08	-
Mean $f_{t,0}$	78	70	59	67	55	65	87	65	85	47
CoV	0.46	-	0.27	0.11	0.51	0.19	0.12	0.14	0.03	-

Table 9 – Mean values $E_{t,0}$ and $f_{t,0}$ [N/mm²] of each failure type for all specimens A - T

Failure	Mean $E_{t,0}$	Mean $f_{t,0}$
Node	13 913	48
Grip	12 629	68
Tension	12 564	71
Shear	11 599	61
Splinter	13 736	78

The overall tension test results for the selected specimens A – T are presented in **Table 10**. Mean value of $f_{t,0}$ is much higher than the mean value of $f_{t,0}$ for class I – III defined by the Italian norm (UNI 11035- 2:2003).

Table 10 – Overall tension test results for specimens A – T: $E_{t,0}$ and $f_{t,0}$ [N/mm²]

	Min	Max	Mean _{selected}	StDev _{selected}	CoV _{selected}
$E_{t,0}$	8 372	18 003	13 048	1 731	0.13
$f_{t,0}$	29	114	73	19	0.25

In conclusion, the strength and stiffness value obtained by the tension test correspond to the class I defined by the Italian norm UNI 11035-2:2003. The CoV values comply with the recommendation of JCSS Probabilistic model code (2006).

APPENDIX 2: Code of constitutive model developed in MATLAB® software

```

clc; clear all; close all; fclose('all');

%--INPUTS I.
Sig_0=[0; 0; 0] ;
Eps_0=[0; 0; 0] ;
%LC CT1-1:
d_Eps_m=[2.4e-3 2.4e-3 2.4e-3 2.4e-3 2.4e-3 2.4e-3 2.4e-3 2.4e-3 2.4e-3 2.4e-3
2.4e-3 2.4e-3 2.4e-3 2.4e-3 2.4e-3 2.4e-3 2.4e-3 2.4e-3 2.4e-3 2.4e-3; 0 0 0 0 0
0 0 0 0 0 0 0 0 0 0 0 0 0 0 0 0; 0 0 0 0 0 0 0 0 0 0 0 0 0 0 0 0] ;
%LC CT1-2: d_Eps_m=[0.8e-3 0.8e-3 0.8e-3 0.8e-3 0.8e-3 0.8e-3 0.8e-3 0.8e-3 0.8e-3
0.8e-3 0.8e-3 0 0 0 0 0 0 0 0 0 0 0 ; 0 0 0 0 0 0 0 0 0 0 0 0 0 0 0 0 0 0 0 0
0 ; 0 0 0 0 0 0 0 0 0 0 0 6e-3 6e-3 6e-3 6e-3 6e-3 6e-3 6e-3 6e-3 6e-3 6e-3] ;
%LC CT1-3: d_Eps_m=[3e-3 0 3e-3 2e-3 2e-3 2e-3 2e-3 2e-3 2e-3 2e-3 2e-3 2e-3
2e-3 2e-3 2e-3 2e-3 2e-3 2e-3 2e-3 2e-3; 0 0 0 0 0 0 0 0 0 0 0 0 0 0 0 0
0 0 0 ; 0 3e-3 3e-3 3e-3 3e-3 3e-3 3e-3 3e-3 3e-3 3e-3 3e-3 3e-3 3e-3 3e-3
3e-3 2e-3 2e-3 2e-3 2e-3 2e-3] ;
%LC CT1-4: d_Eps_m=[5e-3 5e-3 0 0 0 0 0 0 0 0 0 0 5e-3 5e-3 0 0 0 0 0 0; 0 0
0 0 0 0 0 0 0 0 0 0 0 0 0 0 0 0 ; 0 0 2e-3 2e-3 2e-3 2e-3 2e-3 2e-3 -2e-3
-2e-3 -2e-3 2e-3 2e-3 0 0 2e-3 2e-3 2e-3 2e-3 2e-3] ;
%LC CT2-1 d_Eps_m=[0 0 0 0 0 0 0 0 0 0 0 0 0 0 0 0 ; 4e-4 4e-4 4e-4
4e-4 4e-4 4e-4 4e-4 4e-4 4e-4 4e-4 4e-4 4e-4 4e-4 4e-4 4e-4 4e-4 4e-4
4e-4 4e-4 ; 0 0 0 0 0 0 0 0 0 0 0 0 0 0 0 0] ;
%LC CT2-2: d_Eps_m=[0 0 0 0 0 0 0 0 0 0 0 0 0 0 0 0 ; 3e-4 3e-4 3e-4
3e-4 3e-4 3e-4 3e-4 3e-4 3e-4 3e-4 3e-4 3e-4 3e-4 3e-4 3e-4 3e-4 3e-4
3e-4 3e-4 ; 5e-4 5e-4 5e-4 5e-4 5e-4 5e-4 5e-4 5e-4 5e-4 5e-4 5e-4 1e-4 1e-4 1e-4
1e-4 1e-4 1e-4 1e-4] ;
%LC CT2-3: d_Eps_m=[0 0 0 0 0 0 0 0 0 0 0 0 0 0 0 0 ; 4e-4 4e-4 0 0 0
0 0 0 0 0 0 0 4e-4 4e-4 0 0 0 0 0 0 ; 0 0 6e-4 6e-4 6e-4 6e-4 6e-4 -6e-4 -6e-4
-6e-4 -6e-4 -6e-4 0 0 6e-4 6e-4 6e-4 6e-4 6e-4] ;
%LC CT2-4: d_Eps_m=[0 0 0 0 0 0 0 0 0 0 0 0 0 0 0 0 ; 0 0 0 0 0 0 0 0 0
0 0 0 0 0 0 0 0 0 0 ; 4e-3 4e-3 4e-3 3e-4 3e-4 3e-4 3e-4 3e-4 3e-4 3e-4 3e-4
3e-4 3e-4 3e-4 3e-4 3e-4 3e-4 3e-4 3e-4] ;
%LC UNL: d_Eps_m=[5e-3 2e-3 2e-3 2e-3 2e-3 -2e-3 -2e-3 -2e-3 -2e-3 2e-3 2e-3
2e-3 2e-3 0 0 0 0 2e-3 2e-3 2e-3 ; 0 0 0 0 0 0 0 0 0 0 0 0 0 0 0 0 0 0 0
0 ; 0 0 0 0 0 0 0 0 0 0 4e-3 4e-3 4e-3 4e-3 4e-3 4e-3] ;

%--INPUTS II.
Ex=14956; Ey=3088; Gxy=573; %[MPa]
ny_xy=0.023; ny_yx=Ex*ny_xy/Ey;
Ce=[1/Ex -ny_xy/Ey 0;-ny_yx/Ex 1/Ey 0;0 0 1/Gxy]; %Compliance matrix
De_G=inv(Ce); %Stiffness matrix
ft1=74.4 ; ft2=2.2; fs=6.7; %strength [MPa];ft1 = ftx; ft2 = fty; fs=tau_xy
alfa=((ft1*ft2)/(fs^2));

%--INPUTS III. (SCM)
delta_crit_11=0.45; %max crack opening CT1; spruce: 0.45 mm
delta_crit_12=0.15; %max crack opening CT2; spruce: 0.15 mm
l_ch_1=10; %char. length for CT1
l_ch_2=30; % char. length for CT2

```

```

%Failure surface f_Sig:
syms X Y Z real
f_Sig=((X-ft1)+(Y+(k*X)-ft2))/2 + sqrt( ((X-ft1-(Y+(k*X)-ft2))/2)^2 +
    alfa*(Z^2));
X=Sig_0(1); Y=Sig_0(2); Z=Sig_0(3);
f_Sig_0=subs(f_Sig);

if f_Sig_0>0
    f_Sig_0_negat=0 %Incorrect input. The initial value of the failure
        function is f_Sig_0 > 0. Acceptable values are f_Sig_0 < 0
return; end;
if abs(f_Sig_0)<1E-8
    f_Sig_0_negat=0 %Incorrect input. The initial value of the failure
        function is f_Sig_0 = 0. Acceptable values are f_Sig_0 < 0
return; end;
if f_Sig_0<0
    f_Sig_0_negat=1 %Correct input. The initial value of the failure function
        is f_Sig_0 < 0.
end;

%--- A] ELASTIC CALCULATION
f_Sig_n=f_Sig_0; Sig_el_n=Sig_0;
StepN_el = 0; StepN=StepN_el;
Eps_el_n=Eps_0;

%-Write in Excel:
soubor2 = fopen('12_17_FCM_iter_2D_M1aM2_oprava2.csv', 'wt');
soubor = fopen('12_17_FCM_2D_M1aM2_oprava2.csv', 'wt');
fprintf(soubor, '%s\n', '1)Input - elastic calculation');
fprintf(soubor, '%s;%s;%s;%s;%s;%s;%s;%s;%s\n',
    'f_Sig_0_negat','Ex', 'Ey', 'Gxy', 'ny_xy', 'ny_yx', 'ft1', 'ft2', 'fs');
fprintf(soubor, '%.6f;%.6f;%.6f;%.6f;%.6f;%.6f;%.6f;%.6f;%.6f\n',
    f_Sig_0_negat, Ex, Ey, Gxy, ny_xy, ny_yx, ft1, ft2, fs);
fprintf(soubor, '%s;%s;%s;%s;\n', 'Ce(1,1)', 'Ce(1,2)', 'Ce(2,2)', 'Ce(3,3)');
fprintf(soubor, '%.6f;%.6f;%.6f;%.6f;\n', Ce(1,1), Ce(1,2), Ce(2,2), Ce(3,3));
fprintf(soubor, '%s;%s;%s;%s;\n', 'De(1,1)', 'De(1,2)', 'De(2,2)', 'De(3,3)');
fprintf(soubor, '%.6f;%.6f;%.6f;%.6f;\n',
    De_G(1,1), De_G(1,2), De_G(2,2), De_G(3,3));
fprintf(soubor, '%s\n', '2)Elastic calculation');
fprintf(soubor, '%s;%s;%s;%s;%s;%s;%s;%s;%s;%s\n',
    'StepN_el', 'd_Eps(1)', 'd_Eps(2)', 'd_Eps(3)', 'Eps(1)', 'Eps(2)', 'Eps(3)',
    'Sig_el_n(1)', 'Sig_el_n(2)', 'Sig_el_n(3)', 'f_Sig_n');
fprintf(soubor, '%.6f;%s;%s;%s;%.6f;%.6f;%.6f;%.6f;%.6f;%.6f;%.6f\n',
    StepN_el, '-', '-', '-', Eps_0(1), Eps_0(2), Eps_0(3), Sig_el_n(1), Sig_el_n(2),
    Sig_el_n(3), f_Sig_n);

%-Write in vectors:
g_Sig_1=[];g_Sig_2=[];g_Sig_3=[];g_Eps_G_1=[];g_Eps_G_2=[];g_Eps_G_3=[];
g_StepN=[];
g_Eps_c_L_1=[];g_Eps_c_L_2=[];g_Eps_c_L_3=[];

```

```

g_Sig_L_1=[];g_Sig_L_2=[];g_Sig_L_3=[]; g_Eps_L_1=[];g_Eps_L_2=[];g_Eps_L_3=[];
g_Sig_1=[g_Sig_1 (0)];g_Sig_2=[g_Sig_2 (0)];g_Sig_3=[g_Sig_3 (0)];
g_Eps_G_1=[g_Eps_G_1 (0)];g_Eps_G_2=[g_Eps_G_2 (0)];g_Eps_G_3=[g_Eps_G_3 (0)];
g_StepN=[g_StepN (StepN)];
g_Eps_c_L_1=[g_Eps_c_L_1 (0)];
g_Eps_c_L_2=[g_Eps_c_L_2 (0)];g_Eps_c_L_3=[g_Eps_c_L_3 (0)];
g_Sig_L_1=[g_Sig_L_1 (0)];g_Sig_L_2=[g_Sig_L_2 (0)];g_Sig_L_3=[g_Sig_L_3 (0)];
g_Eps_L_1=[g_Eps_L_1 (0)];g_Eps_L_2=[g_Eps_L_2 (0)];g_Eps_L_3=[g_Eps_L_3 (0)];

while f_Sig_n<0
    StepN_el=StepN_el+1; %last el. cycle is divided by f_cic in el. and pl. part
    StepN=StepN_el;
    d_Eps=d_Eps_m(:,StepN_el);
    Sig_el_n=Sig_el_n+De_G*d_Eps;
    X=Sig_el_n(1); Y=Sig_el_n(2); Z=Sig_el_n(3);
    f_Sig_n=subs(f_Sig);
    Eps_el_n=Eps_el_n+d_Eps;
    fprintf(soubor, '%f;%f;%f;%f;%f;%f;%f;%f;%f;%f\n',
        StepN_el, d_Eps(1),d_Eps(2), d_Eps(3),Eps_el_n(1), Eps_el_n(2), Eps_el_n(3),
        Sig_el_n(1), Sig_el_n(2), Sig_el_n(3),f_Sig_n);
end;

    Sig_el_n_above=Sig_el_n
    Sig_el_n_under=Sig_el_n-De_G*d_Eps
    Eps_el_n_under=Ce*Sig_el_n_under;
    f_Sig_n_above=f_Sig_n
        X=Sig_el_n_under(1); Y=Sig_el_n_under(2); Z=Sig_el_n_under(3);
        f_Sig_n_under=subs(f_Sig)
    Sig_el_n_above_x=Sig_el_n(1);
    Sig_el_n_above_y=Sig_el_n(2);
    Sig_el_n_above_z=Sig_el_n(3);
    Sig_el_n_under_x=Sig_el_n_under(1);
    Sig_el_n_under_y=Sig_el_n_under(2);
    Sig_el_n_under_z=Sig_el_n_under(3);

if f_Sig_n>0
    syms t real positive
    Xp=Sig_el_n_above_x+(Sig_el_n_under_x-Sig_el_n_above_x)*t;
    %Xp,Yp,Zp - coordinates of point PEAK (where the yielding starts)
    Yp=Sig_el_n_above_y+(Sig_el_n_under_y-Sig_el_n_above_y)*t;
    Zp=Sig_el_n_above_z+(Sig_el_n_under_z-Sig_el_n_above_z)*t;
    f_Sig_p=((Xp-ft1)+(Yp+(k*Xp)-ft2))/2 + sqrt( ((Xp-ft1-(Yp+(k*Xp)-
        -ft2))/2)^2 + alfa*(Zp^2));
    t_2reseni=solve(f_Sig_p,'t');size_t_2reseni=size(t_2reseni);
    if size_t_2reseni(1)==2
        t_2reseni_1=eval(t_2reseni(1));t_2reseni_2=eval(t_2reseni(2));
        if (t_2reseni_1<1 && t_2reseni_1>0) || t_2reseni_1==1 || t_2reseni_1==0
            t=t_2reseni_1; %parameter t is in an interval [0,1]
        end;
        if (t_2reseni_2<1 && t_2reseni_2>0) || t_2reseni_2==1 || t_2reseni_2==0
            t=t_2reseni_2; %parameter t is in an interval [0,1]
        end;
end;

```

```

end;
if size_t_2reseni(1)==1
    t_2reseni=eval(t_2reseni(1))
    if (t_2reseni<1 && t_2reseni>0) || t_2reseni==1 || t_2reseni==0
        t=t_2reseni; %parameter t is in an interval [0,1]
    end;
end;
Sig_p=[subs(Xp) subs(Yp) subs(Zp)]';
f_Sig_p=((Sig_p(1)-ft1)+(Sig_p(2)+(k*Sig_p(1))-ft2))/2 + sqrt( (((Sig_p(1)-
    -ft1-(Sig_p(2)+(k*Sig_p(1))-ft2))/2)^2) + alfa*(Sig_p(3)^2));
    %check f_Sig_p=0
end;

Eps_p=Ce*Sig_p;
d_Eps_step1_G=d_Eps-(Eps_p-Eps_el_n_under); % 2nd part of el-pl step
fprintf(soubor, '%.6f;%.6f;%.6f;%.6f;%.6f;%.6f;%.6f;%.6f;%.6f;%.6f\n',
    StepN_el, d_Eps_step1_G(1),d_Eps_step1_G(2), d_Eps_step1_G(3),Eps_p(1),
    Eps_p(2), Eps_p(3), Sig_p(1), Sig_p(2), Sig_p(3),f_Sig_p);

    X=Sig_p(1);
    Y=Sig_p(2);
    Zp=Sig_p(3);
    theta=8; %max. crack deviation from the grain [°]
Z_f_CT=(tan(2*(theta/180*pi)))*(X-Y)/2); % (theta/180*pi) [rad]
    fi=0.5*atan(2*Sig_p(3)/(Sig_p(1)-Sig_p(2))); %crack deviation from grain
    fi_deg=fi/pi*180 ;
if Zp> Z_f_CT
    MODE=2; %SC calculation of CT2 (across the fibers)
    n=[0;1]; m=[-1;0];
    delta_crit_1=delta_crit_12;
    l_ch=l_ch_2;
    fi_deg=90;fi=fi_deg/180*pi;
end;
if Zp<= Z_f_CT
    MODE=1 %SC calculation of CT1 (along the fibers)
    n=[cos(fi); sin(fi)]
    m=[-n(2); n(1)];
    fi_deg=fi/pi*180;
    delta_crit_1=delta_crit_11;
    l_ch=l_ch_1;
end;
ec_crit_1=delta_crit_1/l_ch;

%Write in Excel:
fprintf(soubor, '%s\n', '3)Output - elastic calculation');
fprintf(soubor, '%s;%s;%s;%s;%s;%s;%s;%s;%s;%s ;%s;%s;%s;%s;%s\n',
    'MODE', 'f_Sig_p', 'Sig_p(1)', 'Sig_p(2)', 'Sig_p(3)', 'Eps_p_G(1)', 'Eps_p_G(2)',
    'Eps_p_G(3)', 'd_Eps_step1_G(1)', 'd_Eps_step1_G(2)', 'd_Eps_step1_G(3)',
    'fi_deg', 'n(1)', 'n(2)', 'm(1)', 'm(2)');
fprintf(soubor, '%.6f;%.6f;%.6f;%.6f;%.6f;%.6f;%.6f;%.6f;%.6f;%.6f ;%.6f;%.6f;
    %.6f;%.6f;%.6f;%.6f\n', MODE, f_Sig_p, Sig_p(1), Sig_p(2), Sig_p(3),
    Eps_p(1), Eps_p(2), Eps_p(3), d_Eps_step1_G(1), d_Eps_step1_G(2), d_Eps_step1_G(3),

```

```

fi_deg, n(1), n(2), m(1), m(2));

%Write in vectors for graphs at the end:
g_Sig_1=[g_Sig_1 (Sig_p(1))];g_Sig_2=[g_Sig_2 (Sig_p(2))];
g_Sig_3=[g_Sig_3 (Sig_p(3))];g_Eps_G_1=[g_Eps_G_1 (Eps_p(1))];
g_Eps_G_2=[g_Eps_G_2 (Eps_p(2))];g_Eps_G_3=[g_Eps_G_3 (Eps_p(3))];
g_StepN=[g_StepN (StepN)];

%--- B] SMEARED CRACK MODEL (after crack initiation)
%-INPUTS: Eps_p, Sig_p,d_Eps_step1_G (Voigt's notation), n, m
Sig_2ord_p=[Sig_p(1) Sig_p(3);Sig_p(3) Sig_p(2)];
Eps_p_G=Eps_p; %G-global, L-local coordinates

%-- according to angle fi (and CT) we can calculate:
R_De=[(cos(fi))^2 , (sin(fi))^2 , -sin(fi)*cos(fi);
      (sin(fi))^2 , (cos(fi))^2 , sin(fi)*cos(fi);
      2*cos(fi)*sin(fi) , 2*(-sin(fi))*cos(fi) , (cos(fi))^2-(sin(fi))^2];
De_L=R_De'*De_G*R_De;
R_Eps_Sig=[cos(fi) -sin(fi); sin(fi) cos(fi)]; %rotation matrix counterclockwise
d_Eps_2ord_step1_L=R_Eps_Sig*[d_Eps_step1_G(1) , d_Eps_step1_G(3);
                             d_Eps_step1_G(3) , d_Eps_step1_G(2)]*R_Eps_Sig';
d_Eps_step1_L=[d_Eps_2ord_step1_L(1,1); d_Eps_2ord_step1_L(2,2);
              d_Eps_2ord_step1_L(1,2)];
if MODE==1
    Sig_p_hl_L_max=max( (Sig_p(1)+Sig_p(2))/2+sqrt( ((Sig_p(1)-
    -Sig_p(2))/2)^2+Sig_p(3)^2), (Sig_p(1)+Sig_p(2))/2-sqrt( ((Sig_p(1)-
    -Sig_p(2))/2)^2+Sig_p(3)^2) );
    Sig_nn_p_scalar=Sig_p_hl_L_max;
    Sig_nm_p_scalar=0;
else
    tc_p_G=n'*Sig_2ord_p;
    tc_p_L=[tc_p_G(2);tc_p_G(1)]
    Sig_nn_p_scalar=tc_p_L(1);
    Sig_nm_p_scalar=tc_p_L(2);
end;

%-Eps_2ord_p, Sig_2ord_p: G->L
Eps_2ord_p_L=R_Eps_Sig*[Eps_p_G(1) Eps_p_G(3); Eps_p_G(3) Eps_p_G(2)]*R_Eps_Sig';
Eps_p_L=[Eps_2ord_p_L(1,1); Eps_2ord_p_L(2,2); Eps_2ord_p_L(1,2) ];
Sig_p_2ord_L=R_Eps_Sig*Sig_2ord_p*R_Eps_Sig';
Sig_p_L=[Sig_p_2ord_L(1,1); Sig_p_2ord_L(2,2); Sig_p_2ord_L(1,2) ];

%-matrix N_L
N_L=[1 0 0 ; 0 0 1];
%-Qe Acoustic matrix:
Qe_2ord = N_L*De_L*N_L';
%-Dc_2ord:
c1=3;c2=6.93; %parameters of function t_n
syms Eps_c_nn Gama_c_nm real
t_n=Sig_nn_p_scalar*( (1+((c1*l_ch*Eps_c_nn/delta_crit_1)^3)) *exp(-
-c2*l_ch*Eps_c_nn/delta_crit_1) - exp(-

```

```

-c2)*(1+(c1^3))*l_ch*Eps_c_nn/delta_crit_1);

%-calculation of ec_0->0 for defined Sig_nm_p_scalar=t_m
t_m=fs*atan(abs(Gama_c_nm)*((1-((Eps_c_nn*l_ch)/delta_crit_1)^2)/(1-(1-
-((Eps_c_nn*l_ch)/delta_crit_1)^2))))/(pi/2);
if Sig_nm_p_scalar==0;
    Sig_nm_p_scalar_q=(delta_crit_1/l_ch/100);
else Sig_nm_p_scalar_q=Sig_nm_p_scalar;
end;
if (abs(Sig_nm_p_scalar-fs)<=1e-3);
Sig_nm_p_scalar_q=fs-1e-5;
end;
q=solve(t_m-Sig_nm_p_scalar_q,Eps_c_nn,Gama_c_nm);
    if MODE==2; x=-ec_crit_1/1e9;else x=ec_crit_1/1e20;end;
    s_Eps_c_nn_obec=(eval(q.Eps_c_nn));
    Eps_c_nn=max(subs(s_Eps_c_nn_obec))
    Gama_c_nm=x;
    ec_0=[Eps_c_nn;Gama_c_nm];

%---
syms Eps_c_nn Gama_c_nm real
    if MODE==2
        t_m=-fs*atan((-Gama_c_nm)*((1-((Eps_c_nn*l_ch)/delta_crit_1)^2)/(1-(1-
-((Eps_c_nn*l_ch)/delta_crit_1)^2))))/(pi/2);
    else t_m=fs*atan( (Gama_c_nm)*((1-((Eps_c_nn*l_ch)/delta_crit_1)^2)/(1-(1-
-((Eps_c_nn*l_ch)/delta_crit_1)^2))))/(pi/2);
    end;
Dc_2ord=[diff(t_n,Eps_c_nn), diff(t_n,Gama_c_nm); diff(t_m,Eps_c_nn),
diff(t_m,Gama_c_nm)];
Dc_2ord_00=[0, 0; 0, 0];
fc_ec=[t_n;t_m];

%-derivative of fuction s=[fc(ec)+Qe*ec]
syms Eps_c_nn Gama_c_nm real
Qe_times_ec=Qe_2ord*[Eps_c_nn; Gama_c_nm];
diff_Qe_times_ec=[diff(Qe_times_ec(1),Eps_c_nn), diff(Qe_times_ec(1),Gama_c_nm);
diff(Qe_times_ec(2),Eps_c_nn), diff(Qe_times_ec(2),Gama_c_nm)];
s_slope=diff_Qe_times_ec+Dc_2ord;
Eps_c_nn=0; Gama_c_nm=0;
s_slope_eval=subs(s_slope);
    if s_slope_eval(1,1)<0;s_slope_11_positive=0
    else s_slope_11_positive=1; end;
    if s_slope_eval(1,2)<0;s_slope_12_positive=0
    else s_slope_12_positive=1; end;
    if s_slope_eval(2,2)<0;s_slope_22_positive=0
    else s_slope_22_positive=1;end;

%- for Dec_L: De_L*N_L' a N_L*De_L
De_L_times_N_L_T=De_L*N_L';
N_L_times_De_L=N_L*De_L;

%- STEP N (2D):
d_Eps_StepN_L=d_Eps_step1_L;

```



```

d_Eps_StepN_G=d_Eps_step1_G;
d_Eps_iter_L=d_Eps_step1_L;
s_previous=N_L*De_L*Eps_p_L;
d_s_iter=N_L*De_L*d_Eps_iter_L;

ec=ec_0; Eps_c_nn=ec(1); Gama_c_nm=ec(2); % ec_0= ec->0
Dec_StepN_L=De_L-De_L*N_L'*inv(Qe_2ord+subs(Dc_2ord))*N_L*De_L; %Dec(ec_0)
Dec_StepN_G=inv(R_De')*Dec_StepN_L*R_De';
delta=[0;0];
fc_ec_StepN=subs(fc_ec);
fc_ec_plus_Qe_ec=fc_ec_StepN+Qe_2ord*ec;
s_StepN=N_L*De_L*(Eps_p_L+d_Eps_StepN_L) ;
d_s_StepN=N_L*De_L*d_Eps_StepN_L ;
d_ec_StepN=[0;0];
Sig_StepN=Sig_p;
d_Sig_StepN_L= [0; 0; 0];
Sig_StepN_L=[0; 0; 0];
Eps_StepN_G=Eps_p_G;
Eps_StepN_L=Eps_p_L;
d_Eps_StepN_L=d_Eps_step1_L;
d_Eps_c_L=[0; 0; 0];
Eps_c_L=[0; 0 ;0];
iKT=inv(Qe_2ord+subs(Dc_2ord));
StepN_pl=0;
StepN=StepN_el;

fprintf(soubor, '%s\n', '4)Input - FCM calculation');
fprintf(soubor, '%s;%s;%s;%s;%s;%s;%s\n',
        'delta_crit_1', 'Sig_nn_p_scalar', 'Sig_nm_p_scalar','l_ch',
        's_slope_11_pos','s_slope_12_pos','s_slope_22_pos' );
fprintf(soubor, '%.6f;%.6f;%.6f;%f;%f;%f;%f\n',
        delta_crit_1, Sig_nn_p_scalar, Sig_nm_p_scalar, l_ch,
        s_slope_11_positive,s_slope_12_positive,s_slope_22_positive );
fprintf(soubor, '%s\n', '5)Output - FCM calculation');
fprintf(soubor, '%s;%s;%s;%s;%s; %s;%s;%s;%s;%s; %s;%s;%s;%s;%s; %s;%s;%s;%s;%s;
        %s;%s;%s;%s;%s; %s;%s;%s;%s;%s; %s;%s;%s;%s;%s; %s;%s;%s;%s;%s; %s\n',
        'StepN_pl','d_Eps_L(1)', 'd_Eps_L(2)', 'd_Eps_L(3)', 'd_Eps_G(1)',
        'd_Eps_G(2)', 'd_Eps_G(3)', 'Eps_G(1)', 'Eps_G(2)', 'Eps_G(3)', 'd_ec(1)',
        'd_ec(2)', 'ec(1)', 'ec(2)', 'delta(1)', 'delta(2)', 'fc_ec(1)',
        'fc_ec(2)', 'd_Sig(1)', 'd_Sig(2)', 'd_Sig(3)', 'Sig(1)', 'Sig(2)',
        'SigG(3)', 'Dec_G(1,1)', 'Dec_G(1,2)', 'Dec_G(2,2)',
        'Dec_G(3,3)', 'Dec_L(1,1)', 'Dec_L(1,2)', 'Dec_L(2,2)', 'Dec_L(3,3)',
        's_StepN(1)', 's_StepN(2)', 'd_Eps_c_L(1)', 'd_Eps_c_L(2)', 'd_Eps_c_L(3)',
        'iKT(1,1)', 'iKT(1,2)', 'iKT(2,2)', 'StepN' );
fprintf(soubor, '%f;%.6s;%.6s;%.6s;%.6s; %.6s;%.6s;%.6f;%.6f;%.6f;
        %.6f;%.6f;%.6f;%.6f;%.6f; %.6f;%.6f;%.6f;%s;%s; %s;%.6f;%.6f; %.6f;%s;
        %s;%s;%s;%s;%s; %s;%s;%.6f;%.6f;%.6f; %.6f;%.6f;%s;%s;%s; %f\n',
        StepN_pl, '-', '-', '-', '-', '-', '-', Eps_StepN_G(1), Eps_StepN_G(2),
        Eps_StepN_G(3), d_ec_StepN(1), d_ec_StepN(2), ec(1), ec(2), delta(1),
        delta(2), fc_ec_StepN(1), fc_ec_StepN(2), '-', '-', '-', Sig_StepN(1),
        Sig_StepN(2), Sig_StepN(3), '-', '-', '-', '-', '-', '-', '-', '-',
        s_previous(1), s_previous(2), d_Eps_c_L(1), d_Eps_c_L(2), d_Eps_c_L(3), '-');

```

```

        '-', '-', StepN );
fprintf(soubor2, '%s\n', '6)SC iterations within a StepN_pl');
fprintf(soubor2, '%s;%s;%s;%s;%s;%s;%s;%s;%s\n', 'StepN_pl', 'No_pl_iter',
        's_StepN(1)', 's_StepN(2)', 's(1)', 's(2)', 'ec(1)', 'ec(2)', 'StepN');
fprintf(soubor2, '%f;%s;%s;%s;%s;%s;%s;%s;%s\n', StepN_pl, '-', '-', '-',
        s_previous(1), s_previous(2), ec(1), ec(2), StepN);

g_fc_1=[];g_fc_2=[];g_ec_1=[];g_ec_2=[];g_s_1=[];g_s_2=[];g_delta_1=[];
g_delta_2=[];g_Dec_G_11=[];g_Dec_G_22=[];g_Dec_G_33=[];g_Dec_G_12=[];
g_fc_1=[g_fc_1 (fc_ec_StepN(1))];g_fc_2=[g_fc_2 (fc_ec_StepN(2))];
g_ec_1=[g_ec_1 (ec(1))];g_ec_2=[g_ec_2 (ec(2))]; g_s_1=[g_s_1 (s_previous(1))];
g_s_2=[g_s_2 (s_previous(2))];g_delta_1=[g_delta_1 (ec(1)*l_ch)];
g_delta_2=[g_delta_2 (ec(2)*l_ch)];
g_Eps_c_L_1=[g_Eps_c_L_1 (Eps_c_L(1))];g_Eps_c_L_2=[g_Eps_c_L_2 (Eps_c_L(2))];
g_Eps_c_L_3=[g_Eps_c_L_3 (Eps_c_L(3))];
g_Sig_L_1=[g_Sig_L_1 (Sig_p_L(1))];g_Sig_L_2=[g_Sig_L_2 (Sig_p_L(2))];
g_Sig_L_3=[g_Sig_L_3 (Sig_p_L(3))];
g_Eps_L_1=[g_Eps_L_1 (Eps_p_L(1))];g_Eps_L_2=[g_Eps_L_2 (Eps_p_L(2))];
g_Eps_L_3=[g_Eps_L_3 (Eps_p_L(3))];

UNL=0; Kapa=[0; 0]; %Kapa-internal variable, vector or positive increments
d_Eps_c_nn
fc_ec_S_1=0;

StepN_pl=1;
Cond=1;

while StepN<=20

    if ( (abs(ec(1))<ec_crit_1) && (abs(ec(2))<ec_crit_1) && (UNL==0) )
        No_pl_iter=1;
        while Cond > 1e-4
            d_ec_iter=(inv(Qe_2ord+subs(Dc_2ord)))*d_s_iter;
            ec=ec+d_ec_iter;
            Eps_c_nn=ec(1); Gama_c_nm=ec(2);
            d_ec_StepN=d_ec_StepN+d_ec_iter
            s=subs(fc_ec)+Qe_2ord*ec;
            d_s_iter=(s_StepN-s);
            Cond=( sqrt(d_s_iter(1)^2+d_s_iter(2)^2)/sqrt(s_previous(1)^2+
                    +s_previous(2)^2) ) ;

            fprintf(soubor2, '%f;%f;%s;%s;%s;%s;%s;%s;%s\n',
                    StepN_pl, No_pl_iter, s_StepN(1), s_StepN(2),
                    s(1), s(2), ec(1), ec(2), StepN);
            No_pl_iter=No_pl_iter + 1;
        end;
    end;

    if ( (abs(ec(1))<ec_crit_1) && (abs(ec(2))<ec_crit_1) && UNL==1)
        No_pl_iter=1;
        while Cond > 1e-4
            d_ec_iter=(inv(Qe_2ord+subs(Dc_2ord_unl)))*d_s_iter;

```

```

ec=ec+d_ec_iter;
Eps_c_nn=ec(1); Gama_c_nm=ec(2);
d_ec_StepN=d_ec_StepN+d_ec_iter;
s=subs(fc_ec_unl)+Qe_2ord*ec;
d_s_iter=(s_StepN-s);
Cond=( sqrt(d_s_iter(1)^2+d_s_iter(2)^2)/sqrt(s_previous(1)^2+
+s_previous(2)^2) );

fprintf(soubor2, '%f;%f;%.6f;%.6f;%.6f;%.6f;%.6f;%.6f;%.6f;\n',
        StepN_pl, No_pl_iter, s_StepN(1), s_StepN(2),
        s(1),s(2),ec(1),ec(2),StepN);
No_pl_iter=No_pl_iter + 1;
end;
end;

%-- unloading (UNL):
if ( (d_ec_StepN(1)>-1e-8 && d_ec_StepN(2)>-1e-8 && UNL==0) ||
    || ((d_ec_StepN(1))>-1e-8 && d_ec_StepN(2)>-1e-8 && ec(1)>ec_S(1) &&
    && ec(2)>ec_S(2))) );
Kapa=Kapa+d_ec_StepN ;
end;

disp(StepN);disp(UNL); disp(ec); disp(d_ec_StepN); disp(Kapa);

if ( UNL==1 && ((ec(1)-Kapa(1))<1e-8) && ((ec(2)-Kapa(2))<1e-8) &&
    (Kapa(1)-ec(1)>d_ec_StepN(1)) &&abs(Kapa(2)-ec(2)-d_ec_StepN(2))<1e-5 )
    disp('Step_UNL 2->(N-1) '); UNL==1;
end;

if ( UNL==1 && (d_ec_StepN(1)>-1e-8) && (d_ec_StepN(2)>-1e-8) &&
    (abs(Kapa(1)-ec(1))<1e-6) && (abs(Kapa(2)-ec(2))<1e-6) )
    disp('Step_UNL N'); UNL=0
end;

if ( (UNL==0) && (ec(1)-Kapa(1))<1e-8 && (abs(ec(2)-Kapa(2))<1e-8) &&
    && (abs(Kapa(1)-(ec(1)-d_ec_StepN(1)))<1e-8) &&
    && (abs(Kapa(2)-(ec(2)-d_ec_StepN(2))<1e-8)) ) %1st step of UNL
    disp('Step_UNL 1')
    ec_S=ec-d_ec_StepN
    Eps_c_nn=ec_S(1); Gama_c_nm=ec_S(2);
    fc_ec_S=(subs(fc_ec));
    fc_ec_S_1=fc_ec_S(1);ec_S_1=ec_S(1);
%--DATA for iterations:
syms Eps_c_nn Gama_c_nm real
t_n_unl=fc_ec_S(1)/ec_S(1)*Eps_c_nn
t_m=fs*atan( (Gama_c_nm)*((1-((Eps_c_nn*1_ch)/delta_crit_1)^2)/(1-(1-
-((Eps_c_nn*1_ch)/delta_crit_1)^2))))/(pi/2);
fc_ec_unl=[t_n_unl;t_m];
Dc_2ord_unl=[(fc_ec_S(1)/ec_S(1)) 0; Dc_2ord(2,1), Dc_2ord(2,2)];

Eps_c_nn=ec_S(1); Gama_c_nm=ec_S(2);
%--iter.:

```

```

while Cond > 1e-8
    d_ec_iter=(inv(Qe_2ord+subs(Dc_2ord_unl)))*d_s_iter;
    ec=ec+d_ec_iter
        Eps_c_nn=ec(1); Gama_c_nm=ec(2);
    d_ec_StepN=d_ec_StepN+d_ec_iter;
    s=subs(fc_ec_unl)+Qe_2ord*ec;
    d_s_iter=(s_StepN-s);
    Cond=( sqrt(d_s_iter(1)^2+d_s_iter(2)^2)/sqrt(s_previous(1)^2+
        +s_previous(2)^2) );
    fprintf(soubor2, '%f;%f;%.6f;%.6f;%.6f;%.6f;%.6f;%.6f;%.6f\n',
        StepN_pl, No_pl_iter, s_StepN(1),
        s_StepN(2), s(1), s(2), ec(1), ec(2), StepN);
    No_pl_iter=No_pl_iter + 1;
end;
disp(ec); disp(d_ec_StepN);
UNL=1;
end;

if ( abs(ec(1))<ec_crit_1) && (abs(ec(2))<ec_crit_1) )
    d_Eps_c_L=N_L'*d_ec_StepN;
    Eps_c_L=Eps_c_L+d_Eps_c_L;
    d_Sig_StepN_L=De_L*(d_Eps_StepN_L-d_Eps_c_L);
    Sig_StepN_L=Sig_StepN_L+d_Sig_StepN_L;
    d_Sig_2ord_StepN_L=[d_Sig_StepN_L(1) ,d_Sig_StepN_L(3); d_Sig_StepN_L(3) ,
        d_Sig_StepN_L(2)];

    d_Sig_2ord_StepN_G=inv(R_Eps_Sig)*d_Sig_2ord_StepN_L*inv(R_Eps_Sig'); %L->G
    d_Sig_StepN=[d_Sig_2ord_StepN_G(1,1);d_Sig_2ord_StepN_G(2,2);
        d_Sig_2ord_StepN_G(1,2)];
    Sig_StepN=Sig_StepN+d_Sig_StepN
    if UNL==1 ; fc_ec_StepN=subs(fc_ec_unl);
        else fc_ec_StepN=subs(fc_ec);
    end;
end;

else
    fc_ec_StepN=[0;0];
    d_Eps_c_L=N_L'*d_ec_StepN;
    Eps_c_L=Eps_c_L+d_Eps_c_L;
    d_Sig_StepN_L=[0;0;0];
    Sig_StepN_L=[0;0;0];
    d_Sig_StepN=[0;0;0];
    Sig_StepN=[0;0;0];
end;

delta=ec*l_ch;
Eps_StepN_G=Eps_StepN_G+d_Eps_StepN_G;
Eps_StepN_L=Eps_StepN_L+d_Eps_StepN_L;

fprintf(soubor, '%f;%.6f;%.6f;%.6f;%.6f;%.6f;%.6f;%.6f;%.6f;
%.6f;%.6f;%.6f;%.6f;%.6f;%.6f;%.6f;%.6f;%.6f;%.6f;%.6f;%.6f;%.6f;
%.6f;%.6f;%.6f;%.6f;%.6f;%.6f;%.6f;%.6f;%.6f;%.6f;%.6f;%.6f;%.6f;
%.6f;%.6f; %f \n', StepN_pl, d_Eps_StepN_L(1),d_Eps_StepN_L(2),

```

```

d_Eps_StepN_L(3),d_Eps_StepN_G(1),d_Eps_StepN_G(2), d_Eps_StepN_G(3),
Eps_StepN_G(1),Eps_StepN_G(2), Eps_StepN_G(3),d_ec_StepN(1),
d_ec_StepN(2),ec(1), ec(2),delta(1), delta(2),fc_ec_StepN(1) ,
fc_ec_StepN(2), d_Sig_StepN(1), d_Sig_StepN(2), d_Sig_StepN(3),
Sig_StepN(1), Sig_StepN(2), Sig_StepN(3), Dec_StepN_G(1,1),
Dec_StepN_G(1,2), Dec_StepN_G(2,2), Dec_StepN_G(3,3),
Dec_StepN_L(1,1),Dec_StepN_L(1,2),Dec_StepN_L(2,2),Dec_StepN_L(3,3),
s_StepN(1),s_StepN(2) , d_Eps_c_L(1),d_Eps_c_L(2),d_Eps_c_L(3),iKT(1,1),
iKT(1,2), iKT(2,2),StepN );

g_Sig_1=[g_Sig_1 (Sig_StepN(1))];g_Sig_2=[g_Sig_2 (Sig_StepN(2))];
g_Sig_3=[g_Sig_3 (Sig_StepN(3))];
g_Eps_G_1=[g_Eps_G_1 (Eps_StepN_G(1))];g_Eps_G_2=[g_Eps_G_2 (Eps_StepN_G(2))];
g_Eps_G_3=[g_Eps_G_3 (Eps_StepN_G(3))];
g_StepN=[g_StepN (StepN)];g_fc_1=[g_fc_1 (fc_ec_StepN(1))];
g_fc_2=[g_fc_2 (fc_ec_StepN(2))];g_ec_1=[g_ec_1 (ec(1))];
g_ec_2=[g_ec_2 (ec(2))];
g_s_1=[g_s_1 (s_StepN(1))];g_s_2=[g_s_2 (s_StepN(2))];
g_delta_1=[g_delta_1 (ec(1)*l_ch)];g_delta_2=[g_delta_2 (ec(2)*l_ch)];
g_Dec_G_11=[g_Dec_G_11(Dec_StepN_G(1,1))];
g_Dec_G_22=[g_Dec_G_22 (Dec_StepN_G(2,2))];
g_Dec_G_33=[g_Dec_G_33 (Dec_StepN_G(3,3))];
g_Dec_G_12=[g_Dec_G_12 (Dec_StepN_G(1,2))];
g_Eps_c_L_1=[g_Eps_c_L_1 (Eps_c_L(1))];
g_Eps_c_L_2=[g_Eps_c_L_2 (Eps_c_L(2))];g_Eps_c_L_3=[g_Eps_c_L_3 (Eps_c_L(3))];
g_Sig_L_1=[g_Sig_L_1 (Sig_StepN_L(1))];
g_Sig_L_2=[g_Sig_L_2 (Sig_StepN_L(2))];g_Sig_L_3=[g_Sig_L_3 (Sig_StepN_L(3))];
g_Eps_L_1=[g_Eps_L_1 (Eps_StepN_L(1))];
g_Eps_L_2=[g_Eps_L_2 (Eps_StepN_L(2))];g_Eps_L_3=[g_Eps_L_3 (Eps_StepN_L(3))];
if StepN==20
    break;
end;

%---For the next STEP:
if ( (abs(ec(1))>=ec_crit_1) || (abs(ec(2))>=ec_crit_1) )
    No_pl_iter=0;
    Dc_2ord=Dc_2ord_00; fc_ec=[0;0];
    iKT=inv(Qe_2ord+Dc_2ord_00);
    Dec_StepN_L=[0 0 0;0 0 0;0 0 0];
    Dec_StepN_G=[0 0 0;0 0 0;0 0 0];
else
    iKT=inv(Qe_2ord+subs(Dc_2ord));
    Dec_StepN_L=De_L-De_L*N_L'*inv(Qe_2ord+subs(Dc_2ord))*N_L*De_L;
    Dec_StepN_G=inv(R_De')*Dec_StepN_L*R_De';
end;

StepN_pl=StepN_pl + 1;
StepN=StepN+1;
s_previous=s_previous+d_s_StepN;
d_Eps_StepN_G=[d_Eps_m(1,StepN); d_Eps_m(2,StepN); d_Eps_m(3,StepN)];
d_Eps_2ord_L=R_Eps_Sig*[d_Eps_StepN_G(1), d_Eps_StepN_G(3); d_Eps_StepN_G(3),
    d_Eps_StepN_G(2)]*R_Eps_Sig';

```

```

d_Eps_StepN_L=[d_Eps_2ord_L(1,1); d_Eps_2ord_L(2,2); d_Eps_2ord_L(1,2) ];
d_Eps_iter_L=d_Eps_StepN_L;
d_s_StepN=N_L*De_L*d_Eps_StepN_L ;
s_StepN=s_StepN+d_s_StepN;
d_s_iter=N_L*De_L*d_Eps_iter_L;
d_ec_StepN=[0;0];
Cond=1;

    if ( (abs(ec(1))>=ec_crit_1) || (abs(ec(2))>=ec_crit_1) )
        No_pl_iter=1;
        Dc_2ord=Dc_2ord_00; fc_ec=[0;0];
        iKT=inv(Qe_2ord+Dc_2ord_00);
        d_ec_StepN=iKT*d_s_StepN;
        ec=ec+d_ec_StepN;
        Eps_c_nn=ec(1); Gama_c_nm=ec(2);
        s=subs(fc_ec)+Qe_2ord*ec;
        fprintf(soubor2, '%f;%f;%.6f;%.6f;%.6f;%.6f;%.6f;%.6f;%.6f\n',
                StepN_pl, No_pl_iter, s_StepN(1), s_StepN(2),
                s_StepN(1),s_StepN(2),ec(1),ec(2),StepN);
    end;
end;

figure %1
subplot(2,2,1); hold on
    plot(1:length(g_Eps_G_1),g_Eps_G_1,'-xb'),
    plot(1:length(g_Eps_G_2),g_Eps_G_2,':ob'),
    plot(1:length(g_Eps_G_3),g_Eps_G_3,'--.b');
    xlabel('StepN [-]'); ylabel('\epsilon_x ; \epsilon_y ; \epsilon_{x_y} [-]');
    legend('\epsilon_x', '\epsilon_y', '\epsilon_{x_y}');
subplot(2,2,2); hold on
    plot(g_Eps_G_1,g_Sig_1,'-xb');
    xlabel('\epsilon_x [-]'); ylabel('\sigma_x [MPa]');
subplot(2,2,3); hold on
    plot(g_Eps_G_1,g_Sig_2,'-xb');
    xlabel('\epsilon_x [-]'); ylabel('\sigma_y [MPa]');
subplot(2,2,4); hold on
    plot(g_Eps_G_1,g_Sig_3,'-xb');
    xlabel('\epsilon_x [-]'); ylabel('\tau_{x_y} [MPa]');

figure%2
subplot(2,2,1); hold on
    plot(g_Eps_G_2,g_Sig_1,'-xb');
    ylabel('\epsilon_y [-]'); ylabel('\sigma_x [MPa]');
subplot(2,2,2); hold on
    plot(g_Eps_G_2,g_Sig_2,'-xb');
    ylabel('\epsilon_y [-]'); ylabel('\sigma_y [MPa]');
subplot(2,2,3); hold on
    plot(g_Eps_G_2,g_Sig_3,'-xb');
    ylabel('\epsilon_y [-]'); ylabel('\tau_{x_y} [MPa]');

```

```

figure%3
subplot(2,2,1); hold on;
plot(g_Eps_G_3,g_Sig_1,'-xb');
xlabel('\epsilon_x_y [-]'); ylabel('\sigma_x [MPa]');
subplot(2,2,2); hold on;
plot(g_Eps_G_3,g_Sig_2,'-xb');
xlabel('\epsilon_x_y [-]'); ylabel('\sigma_y [MPa]');
subplot(2,2,3); hold on;
plot(g_Eps_G_3,g_Sig_3,'-xb');
xlabel('\epsilon_x_y [-]'); ylabel('\tau_x_y [MPa]');

figure%4
if MODE==1
subplot(2,2,1); hold on
X=g_ec_1; Y=g_ec_2; Z=g_fc_1;
plot3(X, Y, Z, '-db', 'MarkerSize',7,
'MarkerFaceColor', 'c', 'MarkerEdgeColor', 'k');
[X,Y]=meshgrid(0:(ec_crit_1/15):ec_crit_1);
Z=Sig_nn_p_scalar.*( (1+((c1.*l_ch.*X./delta_crit_1).^3)) .*exp(-
-c2.*l_ch.*X./delta_crit_1) - exp(-
-c2).*(1+(c1.^3)).*l_ch.*X./delta_crit_1);
mesh(X,Y,Z);
[X,Y]=meshgrid(ec_crit_1:(ec_crit_1/15):1.2*ec_crit_1,
0:(ec_crit_1/15):ec_crit_1);
Z=(X-X)+(Y-Y) ; mesh(X,Y,Z);
[X,Y]=meshgrid(0:(ec_crit_1/15):1.2*ec_crit_1,
ec_crit_1:(ec_crit_1/15):1.2*ec_crit_1 );
Z=(X-X)+(Y-Y) ; mesh(X,Y,Z);
if fc_ec_S_1>0
[X,Y]=meshgrid(0:(ec_crit_1/10):ec_crit_1/4,0:(ec_crit_1/10):ec_crit_1 );
Z=fc_ec_S_1/ec_S_1.*X; %t_n_unl
mesh(X,Y,Z);
end;
xlabel('\epsilon^c_n_n [-]'); ylabel('\epsilon^c_n_m [-]');
zlabel('t_n [MPa] ');
legend('t_n, i_t_e_r', 't_n, p_r_e_c_i_s_e');
subplot(2,2,2); hold on
X=g_ec_1; Y=g_ec_2; Z=g_fc_2;
plot3(X, Y, Z, '-db', 'MarkerSize',7, 'MarkerFaceColor', 'c',
'MarkerEdgeColor', 'k');
[X,Y]=meshgrid(0:(ec_crit_1/15):ec_crit_1);
Z=fs.*atan(Y.*(1-((X.*l_ch)./delta_crit_1).^2)./(1-(1-
-((X.*l_ch)./delta_crit_1).^2))))./(pi./2);
mesh(X,Y,Z);
[X,Y]=meshgrid(ec_crit_1:(ec_crit_1/15):1.2*ec_crit_1,
0:(ec_crit_1/15):ec_crit_1); Z=(X-X)+(Y-Y) ; mesh(X,Y,Z);
[X,Y]=meshgrid(0:(ec_crit_1/15):1.2*ec_crit_1,
ec_crit_1:(ec_crit_1/15):1.2*ec_crit_1 ); Z=(X-X)+(Y-Y) ; mesh(X,Y,Z);
xlabel('\epsilon^c_n_n [-]'); ylabel('\epsilon^c_n_m [-]');
zlabel('t_m [MPa] '); legend('t_m, i_t_e_r', 't_m, p_r_e_c_i_s_e');
subplot(2,2,3); hold on
X=g_ec_1; Y=g_ec_2; Z=g_s_1;

```

```

plot3(X,Y,Z, '-db', 'MarkerSize',7, 'MarkerFaceColor', 'c',
      'MarkerEdgeColor', 'k');
[X,Y]=meshgrid(0:(ec_crit_1/15):ec_crit_1);
t_n=Sig_nn_p_scalar.*(1+((c1.*l_ch.*X./delta_crit_1).^3)).*exp(-
      -c2.*l_ch.*X./delta_crit_1) - exp(-
      -c2).*(1+(c1.^3)).*l_ch.*X./delta_crit_1);
Qe_times_ec_1=Qe_2ord(1,1).*X+Qe_2ord(1,2).*Y;
Z=t_n+Qe_times_ec_1;
mesh(X,Y,Z);%oaxes([0 0 0]);
xlabel('\epsilon^c_n_n [-]');ylabel('\epsilon^c_n_m [-]');
zlabel('s(1) [-]'); legend('s_i_t_e_r(1)', 's_p_r_e_c_i_s_e(1)');
subplot(2,2,4); hold on
X=g_ec_1; Y=g_ec_2; Z=g_s_2;
plot3(X,Y,Z, '-db', 'MarkerSize',7, 'MarkerFaceColor', 'c',
      'MarkerEdgeColor', 'k');
[X,Y]=meshgrid(0:(ec_crit_1/15):ec_crit_1);
t_m=fs.*atan(Y.*(1-(X.*l_ch)./delta_crit_1).^2)./(1-(1-
      -(X.*l_ch)./delta_crit_1).^2)))./(pi./2);
Qe_times_ec_2=Qe_2ord(2,1).*X+Qe_2ord(2,2).*Y;
Z=t_m+Qe_times_ec_2;
mesh(X,Y,Z);%oaxes([0 0 0]);
xlabel('\epsilon^c_n_n [-]');ylabel('\epsilon^c_n_m [-]');
zlabel('s(2) [-]'); legend('s_i_t_e_r(2)', 's_p_r_e_c_i_s_e(2)');
else %Figure 4
subplot(2,2,1); hold on
X=g_ec_1; Y=g_ec_2; Z=g_fc_1;
plot3(X, Y, Z, '-db', 'MarkerSize',7, 'MarkerFaceColor', 'c',
      'MarkerEdgeColor', 'k');
[X,Y]=meshgrid(0:(ec_crit_1/15):ec_crit_1, -ec_crit_1:(ec_crit_1/15):0);
Z=Sig_nn_p_scalar.*(1+((c1.*l_ch.*X./delta_crit_1).^3)).*exp(-
      -c2.*l_ch.*X./delta_crit_1) - exp(-
      -c2).*(1+(c1.^3)).*l_ch.*X./delta_crit_1);
mesh(X,Y,Z);
[X,Y]=meshgrid(ec_crit_1:(ec_crit_1/15):1.2*ec_crit_1,
      -ec_crit_1:(ec_crit_1/15):0);Z=(X-X)+(Y-Y) ; mesh(X,Y,Z);
[X,Y]=meshgrid(0:(ec_crit_1/15):1.2*ec_crit_1,
      -ec_crit_1:(-ec_crit_1/15):-1.2*ec_crit_1 );Z=(X-X)+(Y-Y) ; mesh(X,Y,Z);
xlabel('\epsilon^c_n_n [-]');ylabel('\epsilon^c_n_m [-]');
zlabel('t_n [MPa] '); legend('t_n, i_t_e_r', 't_n, p_r_e_c_i_s_e');
subplot(2,2,2); hold on
X=g_ec_1; Y=g_ec_2; Z=g_fc_2;
plot3(X, Y, Z, '-db', 'MarkerSize',7, 'MarkerFaceColor', 'c',
      'MarkerEdgeColor', 'k');
[X,Y]=meshgrid(0.00001:(ec_crit_1/30):ec_crit_1+0.00001,
      -0.00001:(-ec_crit_1/15):-ec_crit_1-0.00001);
Z=-fs.*atan((-Y).*(1-(X.*l_ch)./delta_crit_1).^2)./(1-(1-
      -(X.*l_ch)./delta_crit_1).^2)))./(pi./2);
mesh(X,Y,Z);
[X,Y]=meshgrid(ec_crit_1+0.00001:(ec_crit_1/15):1.2*ec_crit_1+0.00001,
      -ec_crit_1-0.00001:(ec_crit_1/15):-0.00001);Z=(X-X)+(Y-Y) ;
mesh(X,Y,Z);
[X,Y]=meshgrid(0.00001:(ec_crit_1/15):1.2*ec_crit_1+0.00001,

```



```

        -ec_crit_1-0.00001:(-ec_crit_1/15):-1.2*ec_crit_1-0.00001 );
Z=(X-X)+(Y-Y) ; mesh(X,Y,Z);
xlabel('\epsilon^c_n_n [-]');ylabel('\epsilon^c_n_m [-]');
zlabel('t_m [MPa] '); legend('t_m_i_t_e_r','t_m_p_r_e_c_i_s_e');
subplot(2,2,3); hold on
X=g_ec_1; Y=g_ec_2; Z=g_s_1;
plot3(X,Y,Z, '-db', 'MarkerSize',7, 'MarkerFaceColor', 'c',
      'MarkerEdgeColor', 'k');
[X,Y]=meshgrid(0:(ec_crit_1/15):ec_crit_1, -ec_crit_1:(ec_crit_1/15):0);
t_n=Sig_nn_p_scalar.*( 1+((c1.*l_ch.*X./delta_crit_1).^3) ).*exp(-
      -c2.*l_ch.*X./delta_crit_1) - exp(-
      -c2).*(1+(c1.^3)).*l_ch.*X./delta_crit_1);
Qe_times_ec_1=Qe_2ord(1,1).*X+Qe_2ord(1,2).*Y;
Z=t_n+Qe_times_ec_1;
mesh(X,Y,Z);
[X,Y]=meshgrid(ec_crit_1+0.00001:(ec_crit_1/30):1.2*ec_crit_1+0.00001,
      -0.00001:(-ec_crit_1/15):-ec_crit_1-0.00001);
t_m= (X-X)+(Y-Y);Qe_times_ec_2=Qe_2ord(1,1).*X+Qe_2ord(1,2).*Y;
Z=t_m+Qe_times_ec_2;
mesh(X,Y,Z);
[X,Y]=meshgrid(0.00001:(ec_crit_1/30):1.2*ec_crit_1+0.00001,
      -ec_crit_1-0.00001:(-ec_crit_1/15):-1.2*ec_crit_1-0.00001);
t_m= (X-X)+(Y-Y);Qe_times_ec_2=Qe_2ord(1,1).*X+Qe_2ord(1,2).*Y;
Z=t_m+Qe_times_ec_2;
mesh(X,Y,Z);
xlabel('\epsilon^c_n_n [-]');ylabel('\epsilon^c_n_m [-]');
zlabel('s(1) [-]'); legend('s_i_t_e_r(1)', 's_p_r_e_c_i_s_e(1)');
subplot(2,2,4); hold on
X=g_ec_1; Y=g_ec_2; Z=g_s_2;
plot3(X,Y,Z, '-db', 'MarkerSize',7, 'MarkerFaceColor', 'c',
      'MarkerEdgeColor', 'k');
[X,Y]=meshgrid(0.00001:(ec_crit_1/30):ec_crit_1+0.00001,
      -0.00001:(-ec_crit_1/15):-ec_crit_1-0.00001);
t_m=-fs.*atan((-Y).*(1-((X.*l_ch)./delta_crit_1).^2)./(1-(1-
      -(X.*l_ch)./delta_crit_1).^2)))./(pi./2);
Qe_times_ec_2=Qe_2ord(2,1).*X+Qe_2ord(2,2).*Y;
Z=t_m+Qe_times_ec_2;
mesh(X,Y,Z);
[X,Y]=meshgrid(ec_crit_1+0.00001:(ec_crit_1/30):1.2*ec_crit_1+0.00001,
      -0.00001:(-ec_crit_1/15):-ec_crit_1-0.00001);
t_m= (X-X)+(Y-Y);Qe_times_ec_2=Qe_2ord(2,1).*X+Qe_2ord(2,2).*Y;
Z=t_m+Qe_times_ec_2;
mesh(X,Y,Z);
[X,Y]=meshgrid(0.00001:(ec_crit_1/30):1.2*ec_crit_1+0.00001,
      -ec_crit_1-0.00001:(-ec_crit_1/15):-1.2*ec_crit_1-0.00001);
t_m= (X-X)+(Y-Y);Qe_times_ec_2=Qe_2ord(2,1).*X+Qe_2ord(2,2).*Y;
Z=t_m+Qe_times_ec_2;
mesh(X,Y,Z);
xlabel('\epsilon^c_n_n [-]');ylabel('\epsilon^c_n_m [-]');
zlabel('s(2) [-]'); legend('s_i_t_e_r(2)', 's_p_r_e_c_i_s_e(2)');
end;

```

```
figure%5
subplot(2,2,1); hold on
plot(g_Sig_3,g_Sig_1,'-xb')
xlabel('\tau_x_y [MPa]'); ylabel('\sigma_x [MPa]');
subplot(2,2,2); hold on
plot(g_Sig_3,g_Sig_2,'-xb');
xlabel('\tau_x_y [MPa]'); ylabel('\sigma_y [MPa] ');
subplot(2,2,3); hold on
plot(g_delta_1,g_delta_2,'-xb'),
xlabel('\delta_n [mm]'); ylabel('\delta_m [mm]');
subplot(2,2,4); hold on
plot(1:length(g_Dec_G_11),g_Dec_G_11,'-b'),
plot(1:length(g_Dec_G_22),g_Dec_G_22,'--xb'),
plot(1:length(g_Dec_G_33),g_Dec_G_33,':b'),
plot(1:length(g_Dec_G_12),g_Dec_G_12,'-.b'),
xlabel('Step_p_1'); ylabel('D_e_c(i,j) [MPa]');
legend('D_e_c(1,1)', 'D_e_c(2,2)', 'D_e_c(3,3)', 'D_e_c(1,2)');
```